EPR-GUIDED DEFECT ENGINEERING OF FE-DOPED ZNO, CIGARETTE-BUTT–DERIVED ACTIVATED CARBON, AND MXENE FOR SUPERCAPACITORS

by
İPEK DENIZ YILDIRIM

Submitted to the Graduate School of Engineering and Natural Sciences
in partial fulfillment of
the requirements for the degree of Doctor of Philosophy

Sabancı University
July 2025

EPR-GUIDED DEFECT ENGINEERING OF FE-DOPED ZNO, CIGARETTE-BUTT–DERIVED ACTIVATED CARBON, AND MXENE FOR SUPERCAPACITORS

Approved by:

Prof. EMRE ERDEM……..

(Dissertation Supervisor)

Assoc. Prof. FERAY BAKAN MISIRLIOĞLU…….

Prof. NURDAN DEMİRCİ SANKIR……..

Asst. Prof. SÜLEYMAN GÖKHAN ÇOLAK……

Asst. Prof. UTKU BULUT ŞİMŞEK…….....

Date of Approval: June 23, 2025

ABSTRACT

EPR-GUIDED DEFECT ENGINEERING OF FE-DOPED ZNO, CIGARETTE-BUTT–DERIVED ACTIVATED CARBON, AND MXENE FOR SUPERCAPACITORS

İPEK DENİZ YILDIRIM

Materials Science and Nano Engineering, Ph.D. Dissertation, July 2025

Dissertation Supervisor: Prof. Emre Erdem

Keywords: iron-doped zinc oxide, MXene, waste materials, electron paramagnetic resonance, supercapacitors.

In this work, we aim to synthesize new materials that achieve high energy density and power density, thereby enhancing the electrochemical performance of supercapacitors. Herein, the focus is given on synthesizing three different materials that will offer EDLC, pseudocapacitive, and hybrid charge storage mechanisms to produce hybrid supercapacitors. Thus, three distinct materials, which are Fe-doped ZnO nanoparticles, $Ti_3C_2T_x$ MXenes, and activated carbons derived from cigarette butts, were synthesized, and paramagnetic defect centers were investigated using EPR spectroscopy. The effect of paramagnetic defect centers on electrochemical performance was analyzed. Firstly, Fe-doped ZnO was synthesized via solid-state reaction to investigate the effect of calcination temperature and dopant concentration. Secondly, $Ti_3C_2T_x$ MXene were synthesized by selectively etching Ti_3AlC_2 in either concentrated HF, HF/HCl and HF/H_2SO_4 mixtures, followed by delamination using LiCl. Finally, waste cigarette-butt were transformed into hierarchically porous carbons through inert-atmosphere carbonization and subsequent KOH activation. Comprehensive characterization, including XRD, Raman spectroscopy, SEM, TGA analysis, BET analysis, PL spectroscopy, and EPR spectroscopy. Symmetric and asymmetric supercapacitors were assembled using two-electrode setup. Electrochemical analyses showed that among all samples, The supercapacitor assembly designed with ball-milled sample oppose to

activated carbon derived by cigarette-butts exhibits the highest performance, reaching 416 F/g, 74 Wh/kg, and 1123 W/kg, surpassing every other design tested under the same conditions. This improvement is attributable to the ball-milling process, as evidenced by the superior results of the ball-milled sample compared to the undoped samples. In symmetric supercapacitors, ZnO:Fe3 delivered the best results (323 F/g, 58 Wh/kg, 1,049 W/kg). Our findings highlight a sustainable pathway for converting waste into high-performance energy storage materials.

ÖZET

ELEKTRON PARAMANYETIK REZONANS REHBERLIĞINDE FE-KATKILI ZNO, SIGARA FILTRESI KAYNAKLI AKTİF KARBON VE MXENELER IÇIN KUSUR MÜHENDISLIĞI VE SÜPERKAPASITÖR UYGULAMALARI

İPEK DENİZ YILDIRIM

Malzeme Bilimi ve Nano Mühendislik, Doktora Tezi, Haziran 2025

Tez Danışmanı: Prof. Dr. Emre Erdem

Anahtar Kelimeler: demir katkılanmış çinko oksit, MXene, atık malzemeler, elektron paramanyetik rezonans spektrometresi, süperkapasitör.

Bu çalışmada, yüksek enerji ve güç yoğunluğu sağlayarak süperkapasitörlerin elektrokimyasal performansını artıracak yeni malzemelerin sentezlenmesi amaçlanmaktadır. Burada odak noktası, hibrit süperkapasitör üretimi için EDLC, sözde kapasitif ve hibrit yük depolama mekanizmalarını sunabilecek üç farklı malzemenin sentezine verilmiştir. Bu kapsamda, demir katkılı ZnO nanopartikülleri, $Ti_3C_2T_x$ MXene'ler ve sigara izmaritlerinden türetilmiş aktif karbonlar olmak üzere üç farklı malzeme sentezlenmiş ve paramanyetik kusur merkezleri EPR spektroskopisi ile incelenmiştir. Paramanyetik kusur merkezlerinin elektrokimyasal performans üzerindeki etkisi analiz edilmiştir. İlk olarak, demir katkılı ZnO, kalsinasyon sıcaklığının ve katkı maddesi konsantrasyonunun etkisini araştırmak amacıyla katı-hal reaksiyonu yöntemi ile sentezlenmiştir. İkinci olarak, $Ti_3C_2T_x$ MXene'ler, Ti_3AlC_2'nin yoğun HF, HF/HCl ve HF/H_2SO_4 karışımlarında seçici olarak aşındırılması ve ardından LiCl ile delaminasyonu ile sentezlenmiştir. Son olarak, atık sigara izmaritleri, inert atmosfer altında karbonizasyon ve ardından KOH aktivasyonu yoluyla hiyerarşik gözenekli karbonlara dönüştürülmüştür. Malzemeler, XRD, Raman spektroskopisi, SEM, TGA analizi, BET analizi, PL spektroskopisi ve EPR spektroskopisi ile kapsamlı bir şekilde karakterize edilmiştir. İki elektrotlu kurulum kullanılarak simetrik ve asimetrik süperkapasitörler oluşturulmuştur. Elektrokimyasal analizler, tüm numuneler arasında,

sigara izmaritlerinden türetilmiş aktif karbona kıyasla bilyeli öğütmeye tabi tutulmuş numune ile tasarlanan süperkapasitörün en yüksek performansı gösterdiğini ortaya koymuştur. Bu tasarım, aynı koşullar altında test edilen diğer tüm tasarımları geride bırakarak 416 F/g spesifik kapasitansa, 74 Wh/kg enerji yoğunluğuna ve 1123 W/kg güç yoğunluğuna ulaşmıştır. Bu iyileşme, bilyeli öğütme işleminin sonucudur ve öğütülmemiş numunelere kıyasla daha üstün sonuçlar vermektedir. Simetrik süperkapasitörlerde ise en iyi sonucu ZnO: Fe3 göstermiştir (323 F/g, 58 Wh/kg, 1049 W/kg). Bulgularımız, atık malzemelerin yüksek performanslı enerji depolama malzemelerine dönüştürülmesinde sürdürülebilir bir yol sunduğunu vurgulamaktadır.

ACKNOWLEDGEMENTS

I extend my deepest gratitude to my advisor, Prof. Dr. Emre Erdem, for his support, genuine kindness, and unwavering belief in my potential. His encouraging guidance and gentle insistence that I venture beyond my comfort zone were instrumental in shaping both the substance and scope of this thesis, and his invaluable assistance in connecting me with new collaborative projects alongside other scientists has broadened my research horizons. His thoughtful feedback, patient mentorship, and readiness to celebrate each milestone have not only driven this work to completion but have also fostered my growth as a researcher and scholar. I am also indebted to my thesis progress committee—Associate Prof. Feray Bakan Mısırlıoğlu and Prof. Dr. Nurdan Demirci Sankır—for generously offering their time, insight, and guidance during my review meetings. Their suggestions were invaluable.

I am deeply grateful to my advisor, Prof. Yury Gogotsi, for his exceptional guidance, unwavering support, and inspiring mentorship throughout this work. His profound expertise in nanomaterials and dedication to scientific rigor have shaped the direction and quality of my research, while his patient discussions of experimental challenges and encouragement to pursue innovative approaches have continually broadened my horizons. It has been a privilege to learn from Prof. Gogotsi's passion for excellence, and his mentorship has been invaluable not only to this project but to my growth as a scientist.

I would like to express my gratitude to Dr. Arpad Mihai Rostas for his guidance and expertise in EPR spectroscopy. Also, I would like to thank him for his collaboration on high-field EPR spectroscopy measurements. A special thank-you goes to my laboratory teammates: Dr. Ahmet Güngör, Mohammed Hasan Aleinawi, Dr. Merve Buldu-Aktürk, and Dr. Ameen Uddin Ammar. Working alongside such capable and helpful colleagues has been a privilege.

I would like to thank also our valuable lab specialists Bilge Esenkal and Cansu Yılmaz Baker for their help in the laboratories and expert technical support—ensuring that

instruments were meticulously maintained, experiments ran smoothly, and troubleshooting was always just a call away.

Finally, I am profoundly grateful to my family, my mother, father, aunt, and sister, for their steady support throughout this journey, and to my always-cheerful dog for brightening each day. I owe particular thanks to my grandmother for the countless lessons she has taught me.

I would like to express my gratitude to Aleyna Demirci for believing in me and being by my side as a true friend. My sincere thanks go to İleyna Üvak, even though we met later, for being there for me and offering her help since the moment we became acquainted. I am deeply thankful to Melih Can Taşdelen for standing by me all these years, never leaving me in both good and difficult times, and always extending his support. I am also grateful to Nazlı Sürmeli for constantly reminding me of her belief in me, especially during the thesis writing process, and for all her support. Finally, I would like to thank all my friends who were able to be present on my thesis day, as well as those who, even if they could not attend, showed their support to me throughout the writing process.

ACKNOWLEDGEMENTS FOR TÜBİTAK

I would like to express my sincere gratitude to the Scientific and Technological Research Council of Türkiye (TÜBİTAK) for supporting my research through the 2214/A – International Doctoral Research Fellowship Program (2022, 2nd Call)**.** Their generous funding enabled the completion of my project, "MXene Synthesis, Characterization, and the Asymmetric Supercapacitor Application of Iron-Ion-Infused Zinc Oxide with MXene," and made it possible for me to spend one year at Drexel University, USA.

I am especially thankful to Prof. Yury Gogotsi for hosting me in his group, for his invaluable guidance, and for the stimulating research environment he provided throughout my stay. Also, I am grateful to every lab member of the Nanomaterials Research group and their help during the project. This fellowship has been instrumental in broadening my scientific perspective and advancing the work presented in this thesis.

I would also like to express my heartfelt gratitude to Jamie Banks, Assistant Director, whose guidance and support throughout the admission process and my entire stay made every step smoother and more welcoming. My sincere thanks go to Molly Peek, our Lab Manager, for her always-available assistance and expert coordination that kept our experiments on track. I am likewise grateful to Deniz Çakır, Dr. Yuan Zhang, Bita Soltan Mohammadlou, and Yash Athreya for their generous help, insightful discussions, and camaraderie, all of which greatly enriched my research experience and daily life in the lab.

TABLE OF CONTENTS

LIST OF TABLES

LIST OF FIGURES

1. INTRODUCTION

Driven by the diminishing availability of fossil fuels and rising pollution, research now focuses on wind, solar, and hydroelectric power, with the main challenge being to match global energy quality and reliability, typically stored using batteries or supercapacitors (An, Tian, Feng, & Qian, 2022; Simon & Gogotsi, 2008). In comparison to other energy-storage technologies, supercapacitors offer distinct advantages, including outstanding cycling durability, rapid charge–discharge capability, and a high level of operational safety (Simon, Gogotsi, & Dunn, 2014; Y. Wu & Cao, 2018). Electrochemical capacitors vary in their charge storage mechanisms according to the choice of electrode materials. Firstly, in Electric double-layer capacitors (EDLCs), charge is accumulated electrostatically on the surface, and the charge storage mechanism is governed by the adsorption and desorption of electrolyte ions. Carbon materials with high surface areas show EDLC behavior. Pseudo capacitors, also known as redox supercapacitors, rely on rapid, reversible chemical reactions at or near the electrode surface to store energy. Typically, transition metal oxides or electrically conducting polymers exhibit pseudo capacitance. Finally, the newest class, hybrid capacitors, utilizes both EDLC and pseudocapacitive storage to enhance the high power capability of capacitors with the high energy density of batteries (Najib & Erdem, 2019; Simon & Gogotsi, 2008). The capacitance of a supercapacitor can be improved by tuning both the material composition and the capacitor architecture. For example, reducing particle dimensions to the sub-nanometer range brings the system close to quantum confinement limits, yielding exceptional electrochemical behavior. Likewise, doping the electrode matrix with transition metal ions (TMIs) such as iron (Fe), manganese (Mn), chromium (Cr), or cobalt (Co) increases its electrical conductivity, which in turn enhances the device's overall capacitance (Najib & Erdem, 2019). The electrode pore diameter and electrolyte ion radius exhibit a direct correlation, and the maximization of specific capacitance is achieved when the pore size distribution closely

matches the solvated ion dimensions, thereby optimizing ion accessibility and double-layer formation kinetics. Furthermore, the intrinsic and extrinsic defect structures critically influence charge storage by modulating electronic conductivity, pseudocapacitive activity, and ion diffusion pathways (Najib & Erdem, 2019). Hence, investigating the defects is a good strategy to guide the rational design of next-generation high-capacitance materials and optimized material–electrolyte interfaces (Genc et al., 2017).

Electron Paramagnetic Resonance (EPR) spectroscopy is a highly effective technique for analyzing the paramagnetic defect centers at the atomic level (Kaftelen et al., 2012). EPR is also highly sensitive for the detection of TM ions, such as Fe^{3+}, $Mn^{2+/4+}$, and $Co^{2+/3+,}$ due to existing unpaired electrons at their outer shells, even at low concentrations (Kaftelen et al., 2012). TM ions do have spin quantum numbers higher than ½ and thus show pronounced zero-field splitting (ZFS), enabling the detection of the electronic structure of the systems. By combining EPR with Raman spectroscopy and Photoluminescence (PL) spectroscopy, researchers can gain a more comprehensive understanding of defect structures, especially in materials like ZnO (Kaftelen et al., 2012). Several research studies have been conducted in the literature that have focused on the defect structures of ZnO, comparing different synthesis routes such as freezer-milling (Kaftelen et al., 2012), and coprecipitation (Erdem, 2014). Doping ZnO with TM ions improves the properties of ZnO. For instance, the effect of Fe doping on the structural, optical, and electronic properties of ZnO has been experimentally investigated for many years. However, due to insufficient analytical characterization of the materials and the lack of data from advanced EPR techniques, which prevents the determination of spin Hamiltonian parameters for Fe^{3+} incorporated into ZnO, the local position of Fe^{3+} in the ZnO lattice and the sign of the zero-field splitting parameters remain unclear and are still a matter of debate (Azamat & Fanciulli, 2007; Heitz, Hoffmann, & Broser, 1992; Igelmund & Hausmann, 1975; P. Zhang, Phan, & Yu, 2012). In most previous EPR studies, Fe^{3+} in ZnO has been investigated either using EPR at only one single EPR frequency or by examining samples with very high Fe concentrations above the solubility limit. In this project, we aim to combine a more comprehensive experimental data set, focusing on the effect of temperature and dopant concentration, using high-frequency and multi-frequency EPR.

With the discovery of single-layer graphene in 2004, it is well known that two-dimensional (2D) free-standing crystals exhibit different properties compared to their three-dimensional (3D) counterparts (Alhabeb et al., 2017; Naguib et al., 2023). The isolation of graphene paved the way for the discovery of new 2-D materials (Alhabeb et al., 2017). Transition metal carbides, nitrides, and carbonitrides that have a formula of $M_{n+1}AX_n$, where n= 1, 2, 3 (M_2AX, M_3AX_2, M_4AX_3), M is an early transition metal (Ti, Zr, Hf, V, Nb, Ta, Cr, Mo, Sc, etc.), A is an element in A-group (mostly groups 13 and 14), and X is a carbon (C), fluorine (F), and nitrogen (N), called as MAX phases and constitutes laminated structures having anisotropic properties (Alhabeb et al., 2017; Anasori, Lukatskaya, & Gogotsi, 2023; Naguib et al., 2012). MAX phases are structurally layered hexagonal with a space group of $P6_3/MMC$ and have two formula units per unit cell, where A-group elements fall within the interlayer of near closed packed M layers and X-atoms fill the octahedral sites (Anasori et al., 2023; Naguib et al., 2012) .It is noted that in the year 2011, over 60 MAX phases were known to exist, and in the year 2017, 70 were known, of which Ti_3AlC_2 is one of the most studied MAX phases (Anasori, Lukatskaya, & Gogotsi, 2017; Naguib et al., 2011). In the MAX phases the A-group elements are relatively weakly bounded and hence the most reactive species in the structure compared to M-X bonds (Naguib et al., 2023; Naguib et al., 2012). Thus $M_{n+1}X_n$ layers are chemically more stable (Naguib et al., 2012). MAX phases partially decompose to $M_{n+1}X_n$ at high temperatures. However, at high temperatures during the decomposition recrystallization is induced and non-layered $M_{n+1}X_n$ 3-D cubic carbides and/or nitrides are formed. Mechanical deformation of MAX phases initiated by basal dislocations can lead to partial delamination, aiding in the formation of lamellas with thicknesses ranging from tens to hundreds of nanometers. Moreover, MAX phases exhibit a combination of metallic, ionic, and covalent bonding, resulting in high bond strength. Therefore, most of the MAX phases were synthesized at temperatures greater than 1600 °C. Until 2011, as far as it is known, there were no studies based on selective room and/or moderate temperature liquid or gas phase extraction of A-group layers in the MAX phases or their exfoliation with strong primary bonds that could lead to a few-nanometer-thick crystalline layers like graphene (Naguib et al., 2023). With the discovery of “MXenes” in 2011, Naguib et al. and his colleagues at Drexel University, USA, there is a lot of ongoing research based on the synthesis of new 2-D materials that have outstanding properties (Naguib et al., 2012). Compared to other 2-D materials MXenes mostly have hydrophilic surfaces as well as high metallic

conductivities (>10,000 S/cm) and hence hold potential in energy storage applications, water desalination technologies, catalysis, wireless communication and electromagnetic interference shielding (Alhabeb et al., 2017; Anasori et al., 2023; Anayee et al., 2020). The first reported MXene, which is 2-D nanosheets comprised of a few titanium carbide ($Ti_3C_2T_x$) layers as well as conical scrolls, is synthesized by wet chemical etching in which the selective etching of the aluminum (Al) layers in the titanium aluminum carbide (Ti_3AlC_2) MAX phase is achieved at room temperature employing the hydrofluoric acid (HF). It was concluded that the following chemical reactions (Eq. (1.1), (1.2), and (1.3) occur when Ti_3AlC_2 is immersed in HF:

$$Ti_3Al_2C_2 + 3\ HF = AlF_3 + 3/2\ H_2 + Ti_3C_2 \quad (1.1)$$

$$Ti_3C_2 + 2\ H_2O = Ti_3C_2(OH)_2 + H_2 \quad (1.2)$$

$$Ti_3C_2 + 2HF = Ti_3C_2F_2 + H_2 \quad (1.3)$$

Structurally, Ti_3AlC_2 is composed of individual Ti_3C_2 layers that were separated by Al-group atoms (Naguib et al., 2011). Upon the introduction of HF, in other words, when reaction (1) takes place, the metallic bonding between the Al atoms and $Ti_3C_2T_x$ is lost, hence removal of the Al atoms and exfoliation of the $Ti_3C_2T_x$ are achieved (Naguib et al., 2012). Since the experiment is held in an aqueous environment rich in fluorine ions, (-F), oxygen (=O), and hydroxyl (-OH) groups were expected to be the possible "T_x" terminations (Alhabeb et al., 2017; Naguib et al., 2011). In the first proposed attempt, 10 gr of $Ti_3Al_2C_2$ powder is immersed in ~100 mL of 50 % concentrated HF solution at room temperature for 2 hours (Naguib et al., 2023; Naguib et al., 2012). After 2 hours, the resultant suspension is washed with de-ionized (DI) water and centrifuged to separate the powders (Naguib et al., 2011). As a result, Al layers were selectively etched and replaced with =O, -OH, and -F surface groups as described in reactions (2) and (3), which leads to the hydrophilic surface (Naguib et al., 2012). Additionally, it was noted that, in addition to nanosheets, nanotubes, scrolls, and multilayers of $Ti_3C_2T_x$ were also observed (Naguib et al., 2012). However, in 2013, it was discovered that by intercalating large organic molecules, 2-D sheets can be delaminated, and the 2-D nature of MXenes became truly exploitable (Alhabeb et al., 2017). The etching parameters for Al-containing MAX phases differ from each other depending on the

transition metal to another, the structure of the material, atomic bonding, as well as the particle size of the MAX phases. As the atomic number of M is increased, the required etching time becomes longer for complete etching. Additionally, since the bonding between M and Al layers is metallic, as the atomic number of M increases, a larger number of M valence electrons are required, and therefore, stronger etching will be necessary. Moreover, since the etching process is kinetically controlled, and hence as the number of "n" increases in the formula, the acquired etching time will be higher. To date, it has been reported that etching of $Ti_3Al_2C_2$ can be achieved using a concentration of> 30 wt.% HF in 5 hours at room temperature (Alhabeb et al., 2017). Anayee *et al.* (Anayee et al., 2020), investigated the effect of etchant acids on the properties of $Ti_3C_2T_X$ and used pure HF, HF/HCl, and HF/H_2SO_4, in which the weight % of HF is kept as 5 % for comparison. The resultant $Ti_3C_2T_X$ has different surface terminations (=O, -OH, -F, -Cl) due to the use of different acid mixtures. It is also seen that the highest conductivity and thermal stability are achieved with HF/H_2SO_4 acid combination (Anayee et al., 2020). MXenes exhibit a combination of high electronic conductivity (20,000 S/cm), a hydrophilic surface, biocompatibility, optical absorption bands in the infrared region, and reversible surface redox reactions, enabling their use in a wide array of fields such as electrical energy storage, electrocatalysis, optoelectronics, communications, water and gas purification, and the pharmaceutical industry. In summary, this unique blend of electrical, chemical, and optical properties makes MXenes highly versatile in a wide range of applications, including energy storage [20], electromagnetic shielding (EMI) [21], electrocatalysis [21], optoelectronics [22], and biomedical applications (Ward et al., 2020; Xu & Gogotsi, 2020).

Activated carbons are critical electrode materials for supercapacitors due to their exceptionally high specific surface area and tunable pore architecture, which together enable the rapid formation of extensive electric double layers, thereby delivering high capacitance. Their interconnected network of micropores, mesopores, and macropores facilitates both ion adsorption and facile electrolyte transport, ensuring excellent rate capability and low internal resistance. Activated carbons are also chemically and mechanically stable over thousands of charge–discharge cycles, cost-effective to produce (especially from biomass or waste precursors), and compatible with a wide range of electrolytes. Together, these advantages make activated carbon electrodes suitable for high-power, long-lifetime electrochemical energy storage devices. Thus,

within this thesis, we aim to synthesize activated carbons from waste materials. An inorganic waste material, cigarette-butts, was selected as a precursor. Each year, approximately 4.5 trillion discarded cigarette filters, which is about 1.69 billion pounds of waste, enter lakes, oceans, and soil, making cigarette butts the most common single item of plastic litter recorded during coastal and urban clean-ups (Slaughter et al., 2011). A cigarette filter is a dense bundle of cellulose acetate fibers (as shown in Figure 1 (a)), a durable plastic that slowly breaks into microplastics and nano plastics while leaching the nicotine, polycyclic aromatic hydrocarbons, and heavy metals it trapped during smoking. The World Health Organization (WHO) and the United Nations Environment Program (UNEP) both classify these filters as problematic single-use plastics and urge their phase-out. Laboratory assays show that leachate from a single smoked filter in one liter of water can kill half of the fish exposed. Ecotoxicology studies have documented the migration of metals, such as arsenic, lead, and cadmium, from discarded butts into sediments and coastal plants, creating pathways for bioaccumulation up the food chain. This global load of persistent plastic fragments, combined with mobile chemical toxins, therefore represents an emerging multi-stress threat to freshwater, marine, and soil environments (Zafeiridou, Hopkinson, & Voulvoulis, 2018). Studies indicate that cigarette filters composed of cellulose acetate seldom break down in natural settings because their tightly packed structure and the acetyl groups within the polymer hinder biodegradation (Haynes, Wilson, & Strickler, 1991; Luke, 1991). When filters are subjected to factors like sunlight and moisture, they can disintegrate into micro-sized plastic fragments that trap and eventually release some of the roughly 7,000 chemicals present in cigarettes. Many of these substances are toxic to ecosystems (as illustrated in Figure 1 (b)), and more than fifty are confirmed to cause cancer in humans (Marinello, Lolli, Gamberini, & Rimini, 2020; Organization, 2017). There are ongoing researches which are based on recycling of cigarette-butts for a variety of applications such as supercapacitors (Meng et al., 2019), hydrogen storage (Blankenship & Mokaya, 2017), waste-water remediation (Panneerselvam, Suresh, Alatawi, Angayarkanni, & Murugan, 2022), decolorization process (Li et al., 2023), and agriculture (Liu et al., 2024).

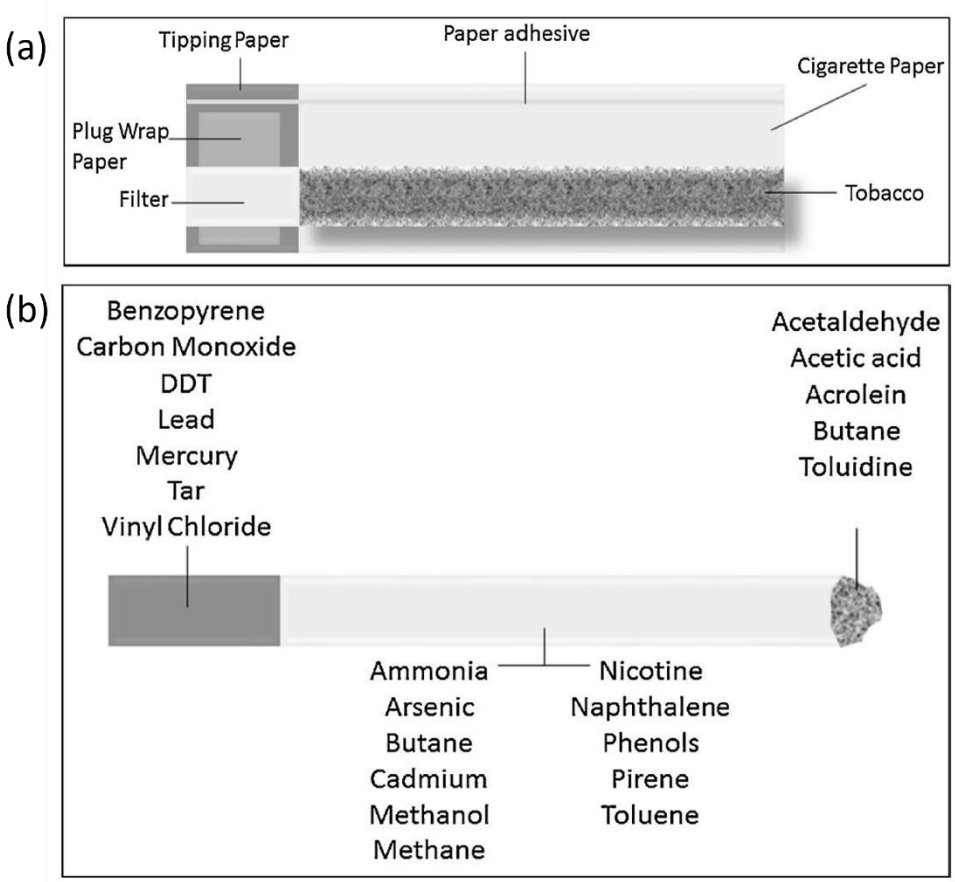

Figure 1 The cigarette butt: (a) the diagram, (b) the composition (Marinello et al., 2020).

Within this thesis, we aim to synthesize new materials that enhance electrochemical performance meaning achieving higher energy density and power densities. To achieve this, three different materials are selected according to the general charge-storage mechanism, which are metal oxides (Fe-doped ZnO) for pseudocapacitance, MXenes for both pseudocapacitance and EDLC behaviour, and carbon materials for EDLC behaviour (Activated carbon from waste cigarette-butts), to produce a hybrid performance in supercapacitors. Our main goal here is to use EPR spectroscopy to study paramagnetic defect centers in the materials and understand their effect on electrochemical performance. Firstly, Fe-doped ZnO will be synthesized using the solid-state reaction technique, which is a facile and solvent-free technique, and to investigate how Fe-doping affects the paramagnetic defects by varying the calcination temperature and dopant concentration. Secondly, $Ti_3C_2T_x$ MXenes using different etchant mixtures will be synthesized, and paramagnetic defect centers will be analyzed using EPR. This will also be important to tune the wet chemical etching protocols of Ti_3AlC_2. Finally, waste cigarette butts were carbonized and activated to produce porous carbons with

high surface areas. By applying EPR spectroscopy in conjunction with electrochemical testing to each system, we will investigate unpaired electrons and relate them to capacitance, thereby establishing a unified defect-engineering strategy for next-generation supercapacitor electrodes. By selecting Fe-doped ZnO, cigarette-butt-derived activated carbon, and MXenes, we span three fundamentally different electrode families: a TM ion-doped metal oxide, a highly conductive 2D carbide, and a sustainable porous carbon. This diversity not only demonstrates a general roadmap for designing high-performance asymmetric supercapacitor electrodes.

In the chapters that follow, Chapter 2 describes the synthesis and preparation of our three electrode materials: Fe-doped ZnO nanoparticles, $Ti_3C_2T_x$ MXene films produced via wet-chemical etching, and activated carbons derived from cigarette butts. Chapter 3 introduces characterization methods: X-ray diffraction, Raman spectroscopy, SEM, BET surface area measurements, TGA, Photoluminescence spectroscopy, and EPR spectroscopy, used to assess phase composition, structural defects, morphology, porosity, and unpaired-electron populations in each material. Chapter 4 presents and discusses our core findings, which were obtained through the characterization methods described in Chapter 4. Chapter 5 will focus on the electrochemical performance, detailing the results of cyclic voltammetry, galvanostatic charge–discharge, and impedance spectroscopy for both symmetric and asymmetric supercapacitor devices. Finally, in Chapter 6, conclusions and future directions will be outlined.

2. SYNTHESIS

Within the aim of this thesis, three different materials, which are Fe-doped ZnO, $Ti_3C_2T_x$, and activated carbon, were synthesized. Throughout Chapter 2, the detailed synthesis of each material was discussed separately.

2.1 Synthesis of Fe-doped ZnO NPs

For the solid-state reaction synthesis of Fe-doped ZnO nanoparticles, ZnO nanopowder and Iron (III) acetylacetonate ($Fe(C_5H_7O_2)$ were selected as precursors and purchased from Sigma-Aldrich, and used as received. Here, we have employed solid-state reaction (SSR) synthesis, as it can accommodate the formation of complex, multielement phases at elevated temperatures without the use of solvents, while remaining simple to execute and easily scalable (A. Kumar et al., 2022). Within this study, the primary concern is how the synthesis parameters affect the defect structure as observed by EPR spectroscopy. Thus, a facile and solvent-free method is selected. Firstly, ZnO and $Fe(C_5H_7O_2)$ were mixed gently in mol% ratios of 0.05, 0.1, 0.5, 1, and 3, and then ground in an agate mortar for 5 minutes. The maximum dopant concentration is selected as 3 moles % due to the high spin-spin interaction observed in the EPR results. Due to high spin-spin interaction causing broadening, the resolution of defect centers becomes challenging. Following this, all samples were placed into ceramic crucibles and calcined at various temperatures in the muffle furnace under ambient conditions. In the muffle furnace, the heating rate was set at 5 °C/min. After calcination for 2 hours, the prepared samples were cooled down at a cooling rate of 10 °C/min to room temperature.

Each sample is prepared using this protocol repeatedly and the illustration of the synthesis route is given in Figure 2.

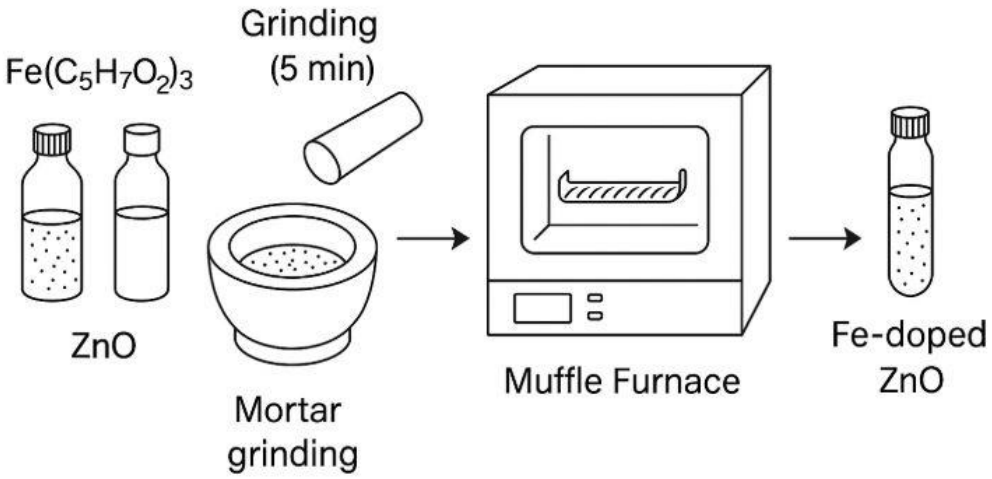

Figure 2 The illustration of the solid-state reaction method to synthesize Fe-doped ZnO.

Within the synthesis, first, the effect of calcination temperature was investigated, as shown in Table 1.

Table 1 The synthesized ZnO: Fe1 at different temperatures.

Sample ID	**($Fe(C_5H_7O_2)_3$ Mol Percentage (%)**	**Calcination Temperature (°C)**	**Time (h)**
ZnO:Fe1-250°C	1 mol	250	2
ZnO:Fe1-300°C	1 mol	300	2
ZnO:Fe1-320°C	1 mol	320	2
ZnO:Fe1-360°C	1 mol	360	2
ZnO:Fe1-400°C	1 mol	400	2
ZnO:Fe1-500°C	1 mol	500	2
ZnO:Fe1-750°C	1 mol	750	2
ZnO:Fe1-900°C	1 mol	900	2

Secondly, the effect of dopant concentration was investigated as in Table 2.

Table 2 The synthesized ZnO:Fe at different dopant concentrations.

Sample ID	$(Fe(C_5H_7O_2)_3$ Mol Percentage (%)	Calcination Temperature (°C)	Time (h)
ZnO:Fe005-1000°C	0.05 mol	1000	5
ZnO:Fe01-1000°C	0.1 mol	1000	5
ZnO:Fe05-1000°C	0.5 mol	1000	5
ZnO:Fe1-1000°C	1 mol	1000	5
ZnO:Fe3-1000°C	3 mol	1000	5

2.2 Synthesis Of Mxenes As Electrodes

2.2.1 HCl Washing

To synthesize $Ti_3C_2T_X$, Ti_3AlC_2 (MAX phase) was bought from Carbon-Ukraine, Ltd., with a particle size <40 μm for the synthesis. For the etching purposes, 48 wt. % HF in H_2O (CAS: 339261), and 37 wt.% HCl in H_2O (CAS: 339253) was bought from Sigma-Aldrich. Firstly, the HCl wash 100 grams of Ti_3AlC_2 is weighed using weight boats. In a 2 L Erlenmeyer flask, a large stir bar is inserted, which is sufficient to cover half of the flask's bottom. Followed by this, 250 mL of DI-water is added to the flask, and then 750 mL of HCl is added under a fume hood. The Erlenmeyer flask was put inside an ice bath on a magnetic stir plate and set to 150 rpm. After 5 minutes, we started to add Ti_3AlC_2 at 1 g/min slowly. Bubbles will be observed due to the exothermic reaction resulting from the dissolution of intermetallic impurities in the HCl. Therefore, the cap of the flask should be left open to allow for gas release, as shown in Figure 3 (a). If a rapid formation of bubbles is observed, the system should be allowed to cool the reaction before adding more Ti_3AlC_2 powder. It should be noted that HCl is a corrosive acid; therefore, during usage, double-nitrile gloves should be worn with proper safety glasses and a laboratory coat. After adding all the Ti_3AlC_2 powder, the

flask should be capped, and the solution should be allowed to stand for 12 hours before neutralizing it with DI water until the pH reaches 6. Then a vacuum-filtration setup is prepared using a Millipore filter to dry the Ti_3AlC_2 powder and powder is left to dry for 2 days.

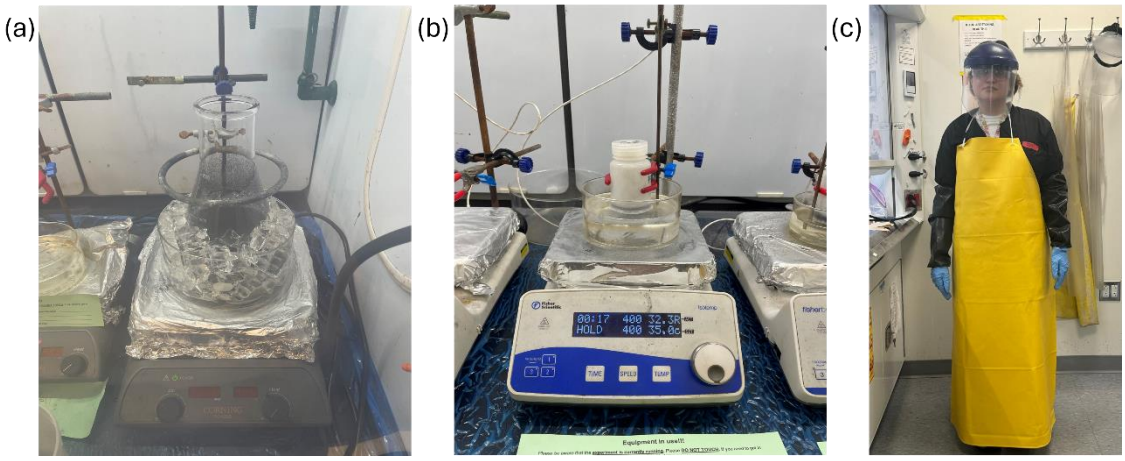

Figure 3 Representation of the synthesis stages; (a) HCl wash step showing the ice bath inside the beaker to cool down the exothermic reaction that occurred during the reaction of the impurities in the MAX phase with HCl, (b) The Etching setup showing the HDPE bottle in the mineral oil bath, (c) The proper HF gear used during etching and washing step which were held at Nanomaterials Lab at Drexel University, USA under supervision of Prof. Yury Gogotsi.

2.2.2 Etching and Delamination of Ti_3AlC_2 MAX Phase

After the HCl wash, 2 g of Ti_3AlC_2 powder is measured using Alumina weight boats and left aside. Followingly, a 250 mL HDPE bottle is taken with a clean stirring bar, which is sufficient to cover half of the bottle's base, and inserted inside. Using a graduated measuring cylinder, the proper amount of DI water was measured and added to the HDPE bottle. Then proper amount of etchant mixtures containing HF, H_2SO_4, HCl, DI water given in Table 3, was added to the HDPE bottle and all pipettes graduated cylinders and beakers used during the preparation were neutralized using DI water and checked to make sure that the pH was 6. Additionally, the waste is placed in the designated waste containers and properly labeled. Then, HF gear was worn as in Figure 3 (c), and the proper amount of HF was added into the HDPE bottle, and the cap was closed to insert the bottle inside of a mineral oil bath on top of the magnetic stirrer.

Here, it should be repeated that HF is a highly strong, and corrosive acid and during its handling proper protective equipment should be worn as in Figure 3 (c). Further safety concerns the handling protocols of HF can be found in articles (Downes, Shuck, McBride, Busa, & Gogotsi, 2024; Shekhirev, Shuck, Sarycheva, & Gogotsi, 2021). Also, in each setup, a thermometer connection is inserted to check the temperature fluctuations. The thermocouple is fixed with clamps to make sure that during the stirring, there will not be any contact between the thermocouple and the beaker. After the HDPE bottle is inserted into the mineral oil bath, the position of the bottle is checked also to prevent any contact of the bottle with the base of the oil beaker to eliminate any corrosion or excessive heating throughout stirring. After carefully putting the bottle inside the mineral oil bath, the stirring is set to 100 rpm at 35 ºC. After waiting for 5 minutes, the cap is untightened and the weighted Ti_3AlC_2 is started to be added as 1 g/min to the bottle by checking the formation of the bubbles to eliminate any risk that may be caused during the exothermic reaction. After adding all the Ti_3AlC_2 powder, as in Figure 3 (b) the cap was tightened loosely, and the stirrer was set to 400 rpm and held for 15 hours for reactions to take place.

Table 3 The required amount of etchant mixtures.

Sample ID	**HF**	**HCl**	**H_2SO_4**	**H_2O**	**Time (h)**
HF	10 mL	-	-	-	24
HF-HCl	4 mL	6 mL	-	-	24
5 HF-H_2SO_4	1 mL	-	1.5 mL	7.5 mL	15
10 HF-H_2SO_4	2 mL	-	1.5 mL	6.5 mL	15
20 HF-H_2SO_4	4 mL	-	1.5 mL	4.5 mL	15

After the etching reaction, the stirrer is closed. 50 mL of DI water is added to 150 mL centrifuge bottles. Followingly, the etching solution is transferred using a pipette from HDPE bottles to centrifuge tubes. The centrifuge tubes were labeled and balanced with another centrifuge tube and centrifuged to 3500 rpm for 5 minutes then the supernatant was discarded to the proper waste container and the washing step was repeated until pH reached 6. It should be noted that at each washing cycle the pH is measured, and HF gear should be worn until the pH reaches 4. When the pH reached 6, half of the samples

were set aside for further characterization, and with the other halves delamination step was continued. 1 gr of LiCl is added to 20 mL of DI water and shaken with hand for 2 mins. Then the mixture is transferred onto the sample using a pipette and shaken using a paint shaker for 8 minutes. The supernatant is discarded again to the waste container and the sample is transferred to 500 mL centrifuge tubes and balanced with DI water. The centrifuge tube was shaken again using a paint shaker for 5 minutes and then centrifuged at 3500 rpm for 15 minutes. After each centrifuge step, the same paint shaking, and centrifugation are repeated and the l the color of the supernatant is checked with a pipette until reaches a dark color. Then, the sample was centrifuged at 3500 rpm for one hour and the supernatant was collected. After 1 hour, the supernatant was taken to another centrifuge tube, and the collection of the supernatant was started. After collecting the supernatant, it was balanced with DI water and continued to be shaken with a paint shaker for 5 minutes, then centrifuged at 3500 rpm for 15 minutes, collecting the supernatant until it reached a transparent color. When the supernatant becomes transparent, it means that the delamination is over and the remaining samples are the multilayer, where the collected solution contains both single and multilayers. Then the solid solution is centrifuged to 10,000 rpm for 20 minutes. The supernatant is discarded into a waste container, and the remaining samples are labeled and stored in the fridge for future use. It should be noted that the samples were carefully parafilmed to prevent any oxidation.

2.2.3 The Preparation of the Free-standing Film

The solid solutions of each sample were diluted in DI water to analyze the concentration of each solution using a UV-VIS spectrometer. After calculating the concentration of the solid solutions, the amount required for each solution to fabricate 6 μm thick free-standing films was calculated. The films were fabricated using vacuum-assisted filtration and left to dry for 2 days as in Figure 4.

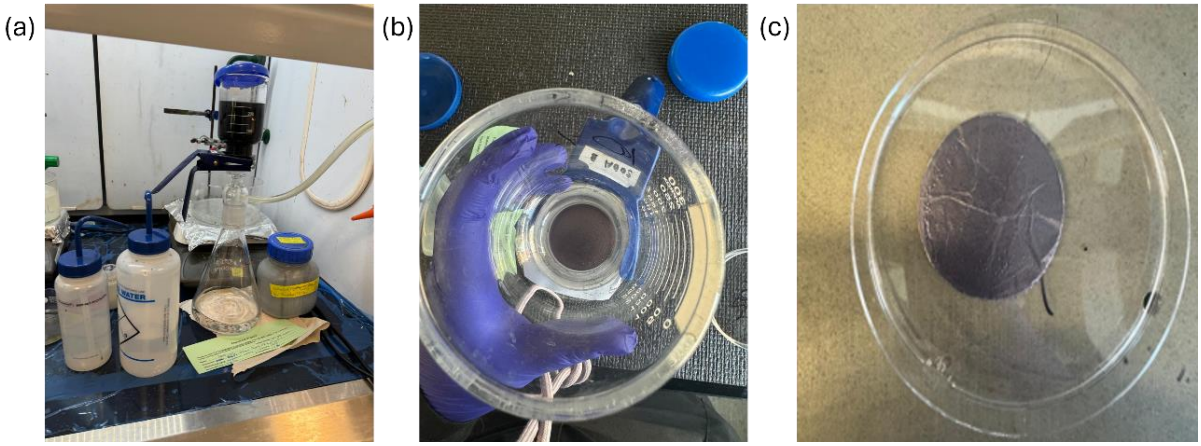

Figure 4 Representation of the synthesis stages: (a) The vacuum-assisted filtration setup to fabricate free-standing MXene films, (b) and (c) Top view of the fabricated free-standing film.

2.3 Synthesis of Activated Carbons from Cigarette-butt

To synthesize ACs, used cigarette butts have been collected from Sabanci University Campus. The discarded cigarette butts were regularly collected from designated collection containers located on the Sabancı University campus. The collected cigarette butts were cleaned by adding 100 mL of deionized water to every 10 grams of butts and stirring the mixture in a glass beaker using a magnetic stirrer for 15 minutes. The cleaned butts were then dried in a vacuum oven at 100 °C for six hours. After drying, acetone was added to dissolve the cigarette filters, which consist of approximately 95 % cellulose acetate. The resulting solution was poured into a petri dish and left to dry under ambient conditions for one day, allowing the acetone to evaporate. The dried material was then ground into powder using a grinder. This process is also illustrated in Figure 5.

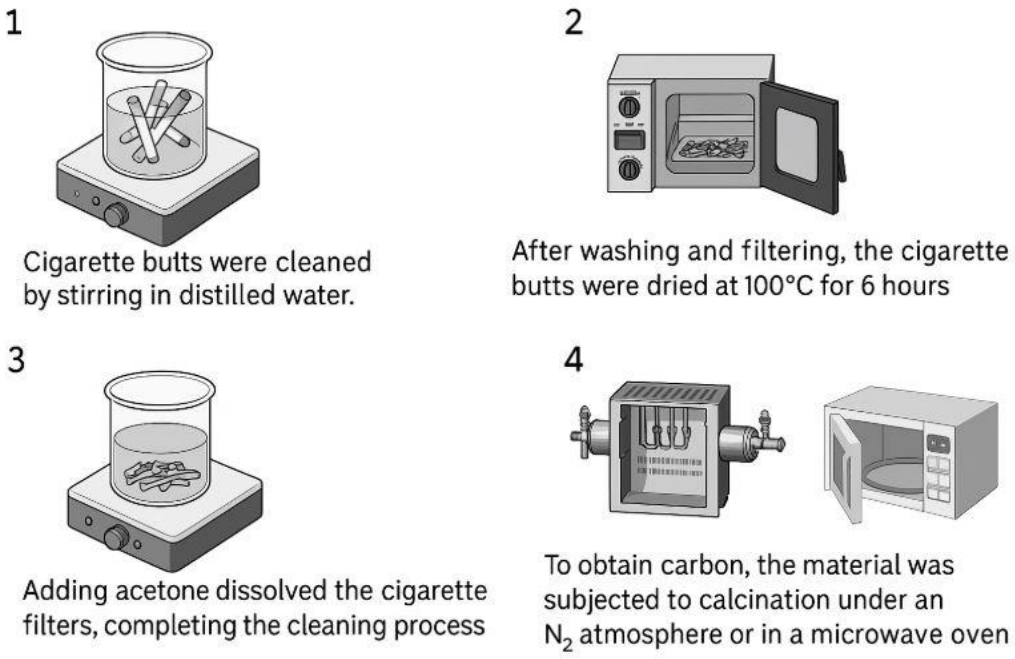

Figure 5 Schematic illustration of the step-by-step procedure to produce activated carbon from waste cigarette butts.

The pre-treatment steps applied to the waste cigarette butts prior to carbonization are illustrated in Figure 6 (a) and (b). The dried cigarette butts then soaked in acetone and cellulose acetate were dissolved as Figure 6 (c).

The carbonization process was carried out in a horizontal tube furnace, as illustrated in Figure 6 (d), under an inert atmosphere (with nitrogen gas at a flow rate of 200 mL/min). The collected and pre-treated cigarette butts were carbonized in the horizontal tube furnace at different temperatures (300, 400, 450, and 500 °C) and for 2 hours, as shown in Table 4. These temperatures were selected based on the TGA results presented in Section 4.4.1, Figure 21.

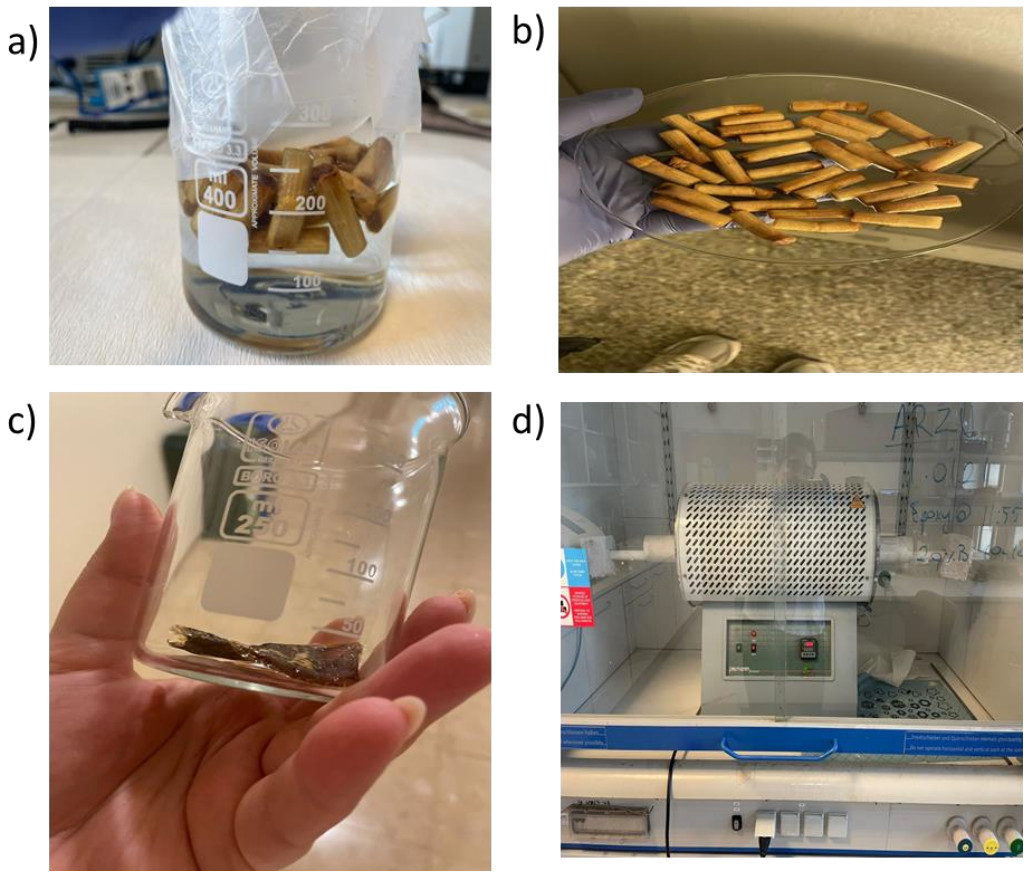

Figure 6 Representation of the processes prior to carbonization: (a) The treatment of cigarette butts in DI water, (b) Dried cigarette-butts in vacuum oven at 100 °C, (c) Dissolved cigarette-butt in acetone, (d) Tube furnace for the carbonization process under inert atmosphere.

Table 4 List of parameters used for the carbonization process.

Sample ID	**Carbonization Temperature (°C)**	**Time (h)**	**N_2 Flow (mL/min)**
CB-300	300	2	200
CB-400	400	2	200
CB-450	450	2	200
CB-500	500	2	200

Following the carbonization process, the EPR and BET analyses were conducted. The cigarette-butt carbonized at 450 °C is selected for further experiments due to its high surface area and pore volume. The use of activation agents in the production of activated carbon plays a critical role in optimizing the material's pore structure, surface area, and adsorption capacity. These agents can be employed in chemical or physical

activation processes, and the surface properties of activated carbon vary significantly depending on the type of activator used (Maciá-Agulló, Moore, Cazorla-Amorós, & Linares-Solano, 2004). Activation agents promote the formation of micro, meso, and macropores within the carbon material. These pores are the fundamental features that enhance the adsorption capacity of activated carbon. Activation agents increase the surface area of the carbon material, providing greater adsorption capacity. A high surface area allows activated carbon to absorb contaminants in both liquid and gas phases more effectively. Activation agents improve surface chemistry by promoting the formation of oxygen, hydrogen, or other functional groups on the carbon surface. This enhances the performance of activated carbon in specific applications, such as the removal of heavy metals or the adsorption of organic pollutants. Chemical activation is typically performed at lower temperatures than physical activation, resulting in energy savings. Moreover, chemical activating agents can simultaneously carry out carbonization and activation, which accelerates the production process (Heidarinejad et al., 2020). The activation process was carried out using three different types of chemical agents: alkali-based (KOH), acidic-based (H_3PO_4), and salt-based ($ZnCl_2$). KOH is highly effective at enhancing the microporous structure of carbon materials, delivering a high surface area and a uniform pore distribution (Lillo-Ródenas, Cazorla-Amorós, & Linares-Solano, 2003). Activation with KOH typically yields high-performance activated carbon ideal for energy-storage applications (J. Wang & Kaskel, 2012). KOH is widely used as an activating agent for carbon materials; at elevated temperatures, it reacts with carbon to generate pores through a simplified reaction, as illustrated in Eq. 2.1 (Lillo-Ródenas et al., 2003).

$$6KOH + 2C \rightarrow 2K + 3H_2 + 2K_2CO_3 \quad (2.1)$$

The gases evolved during this reaction (H_2 and CO) promote the formation and expansion of pores in the carbon structure. KOH activation generally produces high surface area, microporous activated carbons and is especially effective at creating narrow micropores (< 1 nm). These micropores are ideal for ion adsorption in supercapacitor applications. However, KOH activation can make pore-size distribution more challenging to control, and if over-activated, may cause the carbon framework to collapse (Lillo-Ródenas et al., 2003).

$ZnCl_2$ functions as a dehydrating agent, promoting both aromatization and pore development in the carbon framework during carbonization (Y. Huang, Liu, & Zhao, 2016). By interacting with the carbon precursor, $ZnCl_2$ prevents structural degradation and encourages pore creation throughout the process. Activated carbons produced with $ZnCl_2$ typically exhibit a broader pore-size distribution and favor the formation of mesopores (2–50 nm) (Caturla, Molina-Sabio, & Rodriguez-Reinoso, 1991). These mesopores enable faster diffusion of electrolyte ions into the electrode material, thereby enhancing the power performance of supercapacitors. Compared with KOH, $ZnCl_2$ can be employed at lower activation temperatures, resulting in energy savings (Caturla et al., 1991; Y. Huang et al., 2016). The principal drawback is that $ZnCl_2$ is highly corrosive and has adverse environmental impacts. A simplified activation reaction is shown in Eq. (2.2) (J. Yang & Qiu, 2011).

$$ZnCI_2 + C_xH_yO_z \rightarrow Zn + HCI + H_2O + C_{x-1} \quad (2.2)$$

H_3PO_4 interacts with the carbon precursor before carbonization, promoting cross-linking and dehydration (Duan, Srinivasakannan, Wang, Wang, & Liu, 2017). This makes the carbon structure more ordered, enabling controlled pore formation. Activated carbons produced with H_3PO_4 typically have a broad pore-size distribution and support the development of both micro- and mesopores (H. Yang et al., 2022). H_3PO_4 can increase carbon yield and, by fostering the formation of oxygen-containing functional groups on the surface, enhance the wettability and electrochemical performance of the electrode material (Jibril, Houache, Al-Maamari, & Al-Rashidi, 2008; Liang, Li, Zhang, Wang, & Hu, 2024). A simplified activation reaction is presented in Eq. (2.3).

$$H_3PO_4 + C_xH_yO_z \rightarrow H_2O + C_{x-1} + PO_x \quad (2.3)$$

For each activating agent, three different mass ratios of carbon precursor to activating agent, 1:1, 1:2, and 1:3, were tested, and the details are given in Table 5 below. All activation processes were conducted using a carbonized cigarette-butt at 450 ºC due to the high BET surface area and pore values as discussed in section 4.5 Table 8.

Table 5 The parameters used for the chemical activation process.

Activating Agent	**Activator Ratio (m_{CP}: m_{agent})**	**Time (h)**	**N_2 Flow (mL/min)**	**Activating Temperature (°C)**
1:1	KOH	2	200	450
1:1	H_3PO_4	2	200	450
1:1	$ZnCl_2$	2	200	450
1:2	KOH	2	200	450
1:2	H_3PO_4	2	200	450
1:2	$ZnCl_2$	2	200	450
1:3	KOH	2	200	450
1:3	H_3PO_4	2	200	450
1:3	$ZnCl_2$	2	200	450

3. CHARACTERIZATION METHODS

3.1 X-ray Diffraction (XRD)

X-ray diffraction (XRD) is a non-destructive analytical technique commonly used to examine the crystal structure of solid materials, including metals, ceramics, and polymers. The method operates based on constructive interference, as described by Bragg's law as Eq. (3.1)

$$n\lambda=2d\sin\theta \quad (3.1)$$

where n is an integer, λ is the wavelength of the X-ray, d is the interlayer spacing, and θ is the incident angle. It enables identification of crystalline phases and lattice parameters when the material composition is unknown, and it also allows for the calculation of crystallinity, internal strain, and the relative abundance of different phases within a sample. The diffraction patterns were recorded under ambient conditions using a Bruker D2 Phaser X-ray diffractometer, operating with Cu-Kα radiation (λ = 1.540 Å) at 30 kV and 10 mA. Scans were performed over a 2θ range of 5° to 90°, with a step size of 0.02° s^{-1}. Phase identification was carried out using DIFFRAC.EVA software (version 4.2, Bruker)

3.2 Raman Spectroscopy

Raman spectroscopy is a vibrational analysis technique that relies on light–matter interactions and the change in a molecule's polarizability during its vibrational motion. In this method, a high-intensity laser beam is focused on a sample, exciting the target molecules. This interaction induces dipole moments associated with specific vibrational modes, leading to the inelastic scattering of light known as Raman scattering. The resulting spectral data provides distinct chemical and structural information unique to each molecule, effectively serving as a molecular fingerprint. Raman spectroscopy is widely used for both qualitative and quantitative characterization of organic, inorganic, and biological compounds. In this dissertation, Raman spectroscopy was employed to study the defect structure of the materials, specifically by examining the presence and characteristics of the D- and G-bands for carbon materials. For carbon materials, the D- and G-bands originate from the sp^2 regions of possible free carbons in the samples and are detected around 1350 cm^{-1} and 1570 cm^{-1} in the Raman spectrum, respectively. The G-band peak is associated with the stretching of the C-C bond in all sp^2 carbon systems, including both rings and chains. In contrast, the D peak depends on the sp^2 fraction and order and appears only if the sp^2 is in disordered rings (Y. Wang, Alsmeyer, & McCreery, 1990). Measurements of Fe-doped ZnO and AC were performed using a Renishaw inVia Raman spectrometer equipped with a 532 nm green laser, under ambient conditions. The Raman Spectroscopy analysis was carried out at the University of Pennsylvania, USA, using a Reinshaw spectrometer with a 785 nm laser at room temperature.

3.3 Scanning Electron Microscopy (SEM)

Scanning Electron Microscopy (SEM) is a widely used technique for examining the morphology and microstructure of materials. It operates by directing a focused beam of electrons across the surface of a sample. As these electrons interact with the material,

they generate various signals that provide detailed information about the sample's surface topography and composition.

In this study, the particle size, microstructural characteristics, and surface morphology of the synthesized materials were examined using a field emission scanning electron microscope (FE-SEM, Zeiss Leo Supra 35 VP). The system was equipped with a field emission gun (FEG) and operated at an accelerating voltage ranging from 3 to 15 kV to capture high-resolution images. Before imaging, the samples were coated with a thin layer of Au-Pd using a Cressington 108 sputter coater at 40 mA for 120 seconds.

3.4 Differential thermal analysis (DTA) and thermogravimetric analysis (TGA)

Thermal analysis plays a vital role in solid-state physics and chemistry, providing insight into a material's thermal stability, phase transitions during heating, and weight changes as temperature varies. In this study, differential thermal analysis (DTA) was employed to investigate the thermal behavior of the cigarette-butts, with a particular focus on the decomposition of organic components and temperature-dependent phase transitions. This analysis played a crucial role in determining suitable temperatures for carbonizing the cigarette butts. Concurrently, thermogravimetric analysis (TG) was performed to monitor mass loss during heating, using a Shimadzu DTG-60H system capable of simultaneous TG/DTA measurements.

3.5 Brunauer-Emmett-Teller (BET)

A porous material's effectiveness is usually gauged by its internal surface area per unit mass or volume, a property most often determined through gas-adsorption tests. The notion of quantifying surface area in this way dates back to Langmuir's landmark studies on monolayer adsorption (Langmuir, 1916, 1918). In the Langmuir framework, gas molecules attach in a one-to-one (stoichiometric) fashion to specific lattice sites, providing a quantitative measure of a flat surface's area. Brunauer, Emmett, and Teller

later expanded this thermodynamic approach to describe multilayer adsorption (Brunauer, Emmett, & Teller, 1938; Emmett & Brunauer, 1937). Hence, BET analysis is conducted to analyze the surface areas and pore volumes of the carbonized and further activated materials. Within this thesis, the measurements were held using the BET technique on a Micromeritics Tristar II analyzer after an overnight degassing at 120 °C.

3.6 Photoluminescence Spectroscopy (PL)

Photoluminescence (PL) spectroscopy is a powerful technique for investigating the energy levels of various materials, particularly semiconductors. In a typical PL excitation experiment, a laser with a fixed wavelength excites electrons in the material, promoting them from their ground state to an excited state. As these electrons return to their ground state, they release excess energy in the form of photons. This emitted light is detected and converted into an electrical signal, producing a spectrum that shows PL intensity as a function of excitation wavelength. The resulting data provides valuable insights into both intrinsic and extrinsic electronic transitions. Extrinsic transitions are often associated with defect states—such as trap states—because transitions near the band edge typically involve lower energy emissions and appear at longer wavelengths.

In this study, an FS5 Edinburgh Instruments PL spectrometer was used to investigate the optoelectronic behavior of point defects in the synthesized particles. The system included a 150 W continuous-wave, ozone-free xenon arc lamp as the light source, a Czerny-Turner monochromator with plane gratings, and a dedicated sample holder designed for direct measurement of solid-state samples. The PL measurement of ZnO and Fe-doped ZnO was conducted with an excitation wavelength of 320 nm, and emission spectra were recorded for 360 to 700 nm. Whereas, the PL measurement of $Ti_3C_2T_x$ films was recorded at an excitation wavelength of 300 nm, and emission was recorded from 360 to 700 nm. All PL measurements are conducted at room temperature.

3.7 Electron Paramagnetic Resonance (EPR) Spectroscopy

Electron Paramagnetic Resonance (EPR), also known as Electron Spin Resonance (ESR), is a non-destructive analytical technique that detects the absorption of microwave-frequency electromagnetic radiation by paramagnetic materials. It is widely applied across disciplines such as physics, chemistry, biology, and medicine to study free radicals, redox processes, reaction kinetics, conducting electrons, and—most relevant here—point defects. Atoms, ions, or molecules containing unpaired electrons in their outermost orbitals exhibit unique electronic behaviors. EPR exploits the magnetic moments arising from these unpaired electron spins.

In the absence of an external magnetic field, the spin states of unpaired electrons are degenerate, meaning they have the same energy. When a magnetic field is applied, this degeneracy is lifted due to the Zeeman effect. These states differ in energy, and resonance occurs when the energy difference between them matches the energy of the incoming microwave photon. This relationship is defined by Eq. (3.2) as the resonance condition:

$$\Delta E = h\nu = g\,\beta\,B_0 \quad (3.2)$$

where h is Planck's constant (6.626×10^{-34} J·s), ν is the microwave frequency, g is the dimensionless spectroscopic splitting factor (g-factor), β is the Bohr magneton (9.274×10^{-24} J·T^{-1}), and B_0 is the external magnetic field (in Tesla).

In this thesis, paramagnetic point defects were analyzed using both X-band (9.64 GHz) and Q-band (33.98 GHz) EPR spectroscopy. For X-band measurements, samples were placed in a 25 cm-long spin-free quartz tube (Qsil, Germany), and spectra were recorded at room temperature using a Bruker EMX Nano spectrometer. Q-band measurements were conducted using a Bruker Elexsys 500 spectrometer fitted with an ER 5106 QT probe designed for continuous-wave EPR. Dr. Arpad Mihai Rostas performed the Q-band studies at the National Institute for Research and Development of Isotopic and Molecular Technologies in Romania, while the room-temperature X-band

measurements and the analysis of all EPR data presented in this thesis were carried out by the author. The ultra-high-field EPR measurements were performed at the National High Magnetic Field Laboratory, Tallahassee, USA. The EPR measurements were performed at 112, 216, 324, and 406 GHz.

3.8 Electrochemical Analysis

Electrochemical measurements were performed using a Biologic VMP 300 multi-channel potentiostat with our all-in-one supercapacitor. Using an all-in-one supercapacitor device, we employed a two-electrode setup to investigate the electrochemical performance of assembling a supercapacitor. In the two-electrode system (as illustrated in Figs. 7(a) and (b)), we have varied the electrode materials among the synthesized samples and built both symmetric and asymmetric supercapacitors. We have used Whatman porous glass fiber paper (Whatman, grade GF/F) separator in all supercapacitors. We have used two different electrolytes, which are 6 M KOH and 1 M H_2SO_4, in the supercapacitors. The electrodes were prepared by depositing the slurry of AC, PTFE and Electrode Material in a wt. % of 10:10:80, respectively, and dried using a vacuum oven at 70 ºC as in Figure 7 (c) and (d). The performance of the supercapacitors and the electrochemical performance of the electrode material was tested using CV, GCPL, and PEIS. CV curves were determined by controlling the oxygen evolution reaction (OER) and hydrogen evolution reaction (HER). The safe voltage window is observed to be 0 to +0.6 V and is applied during the tests. PEIS measurements were performed using a 10 mV sinusoidal signal with a frequency range of 100 MHz to 100 kHz. GCPL was conducted within a voltage window of 0 to +0.6 V at specific current densities of 1 A/g.

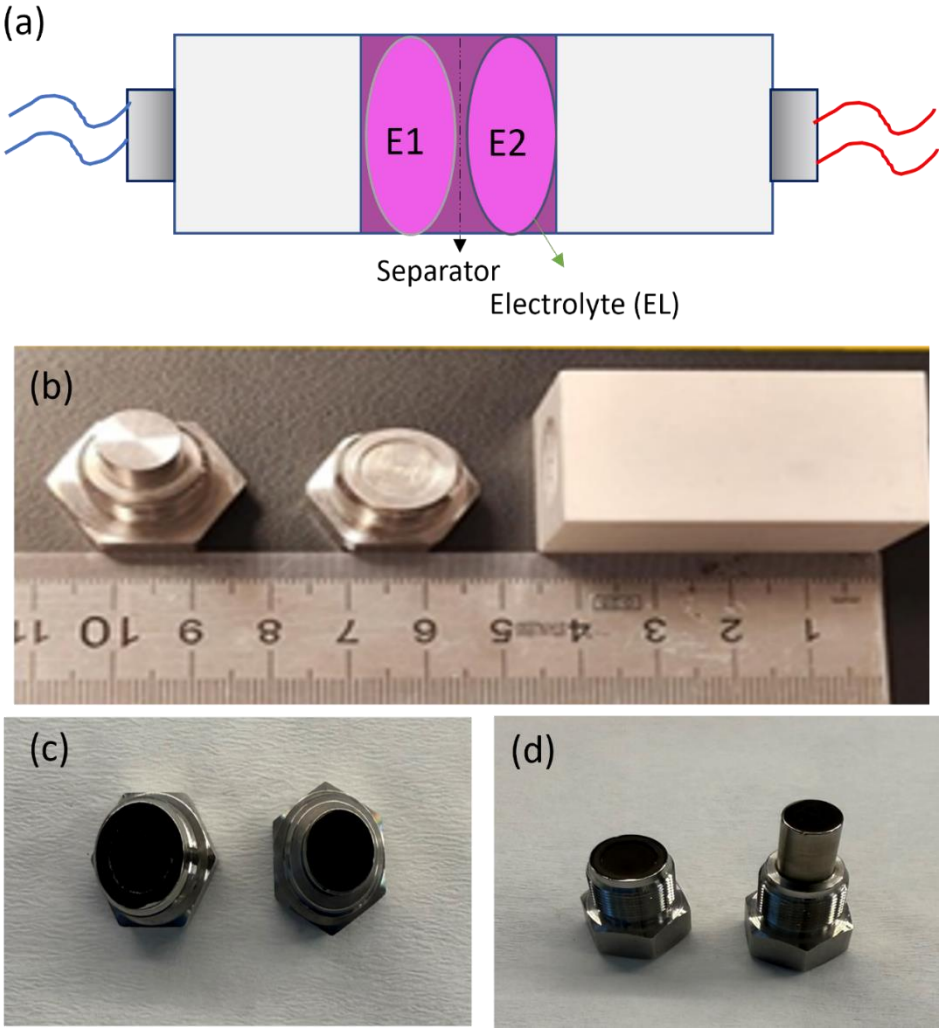

Figure 7 The all-in-one supercapacitor; (a) design showing electrode 1 (E1), electrode 2 (E2), electrolyte (EL), and separator, (b) all-ion-one supercapacitor device, (c) and (d) top and front view of electrodes with stainless steel current collectors.

4. RESULTS AND DISCUSSION

4.1 XRD Analysis

4.1.1 Fe-doped ZnO NP

To isolate the influence of calcination temperature, all other synthesis variables were held constant. At the same time, Fe-doped ZnO powders (ZnO: Fe1) were treated at 250, 300, 320, 360, 400, 500, 750, 850, and 900 °C (as in Figure 8). X-ray diffraction confirmed single-phase materials, with no reflections attributable to impurities or secondary phases. Every pattern could be indexed to the hexagonal wurtzite ZnO structure, exhibiting the characteristic (100), (002), (101), (102), (110), and (103) reflections, as listed in PDF 70-2205. To probe the influence of dopant concentration, the Fe precursor molarity was adjusted from 0.05 to 3 mol% %, while all other synthesis parameters were held constant. Here, the calcination was performed at 1000 °C for 5 hours. X-ray diffraction analysis of Fe-doped ZnO synthesized with precursor concentrations between 0.05 and 3 mol% % is shown in Figure 9. Up to 0.5 mol% % Fe, every reflection matches the wurtzite ZnO reference (PDF 79-2205), and no extra peaks appear, indicating that Fe^{3+} is fully accommodated in the ZnO lattice. A slight shift of the ZnO peaks toward higher 2θ values accompanies this doping, consistent with the lattice contraction expected when the smaller Fe^{3+} ion (≈ 0.645 Å) substitutes for Zn^{2+} (≈ 0.75 Å) both in Fig.8 and Figure 9 (Bai et al., 2014). At and beyond 1 mol % Fe, additional reflections emerge at ≈ 30.1°, 35.5°, and 43° 2θ that index to the (220), (311), and (400) planes of spinel $ZnFe_2O_4$ (PDF 79-1150); their intensity increases further at 3 mol %, confirming precipitation of a secondary spinel phase once the solid-solution limit is exceeded. This second phase has only been observed in the 1 and 3

mol% Fe-doped ZnO and is very low and incomplete in intensity. Thus, this could be related to the solubility limit or result from impurities.

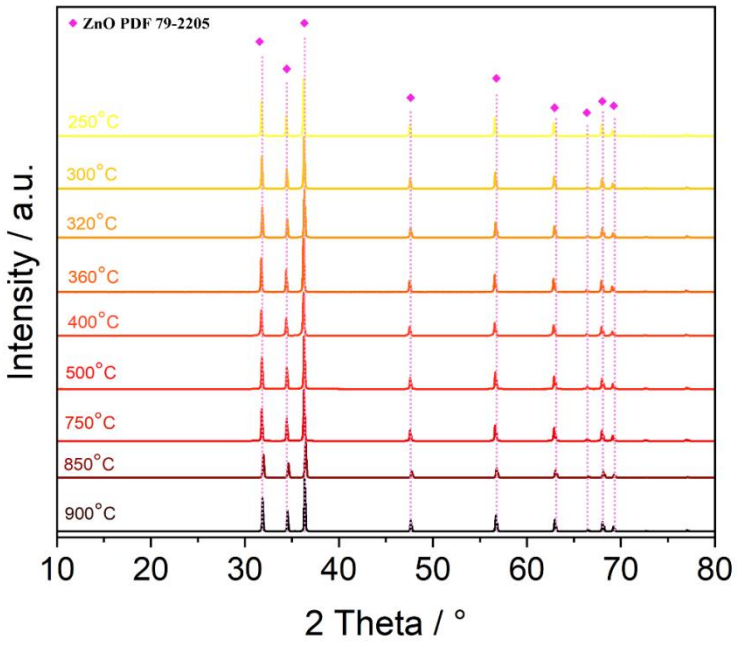

Figure 8 XRD pattern of ZnO: Fe1 calcinated at various temperatures.

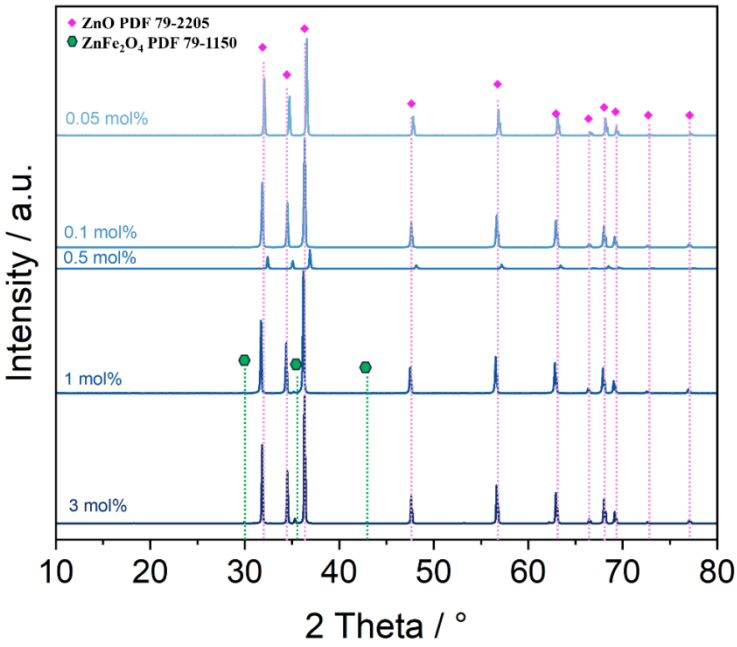

Figure 9 XRD pattern of synthesized Fe-doped ZnO at different dopant concentrations.

4.1.2 XRD of $Ti_3C_2T_x$ MXene

The XRD analysis of the samples was conducted at Drexel University using a Rigaku Mini Flex XRD (voltage and current of the X-ray generator were 40 kV and 15 mA) with Cu Kα radiation and a step scan of 0.04 °. XRD measurements were carried out for the MAX phase precursor and all the synthesized powder and film samples for detailed comparison, as in Figure 10.

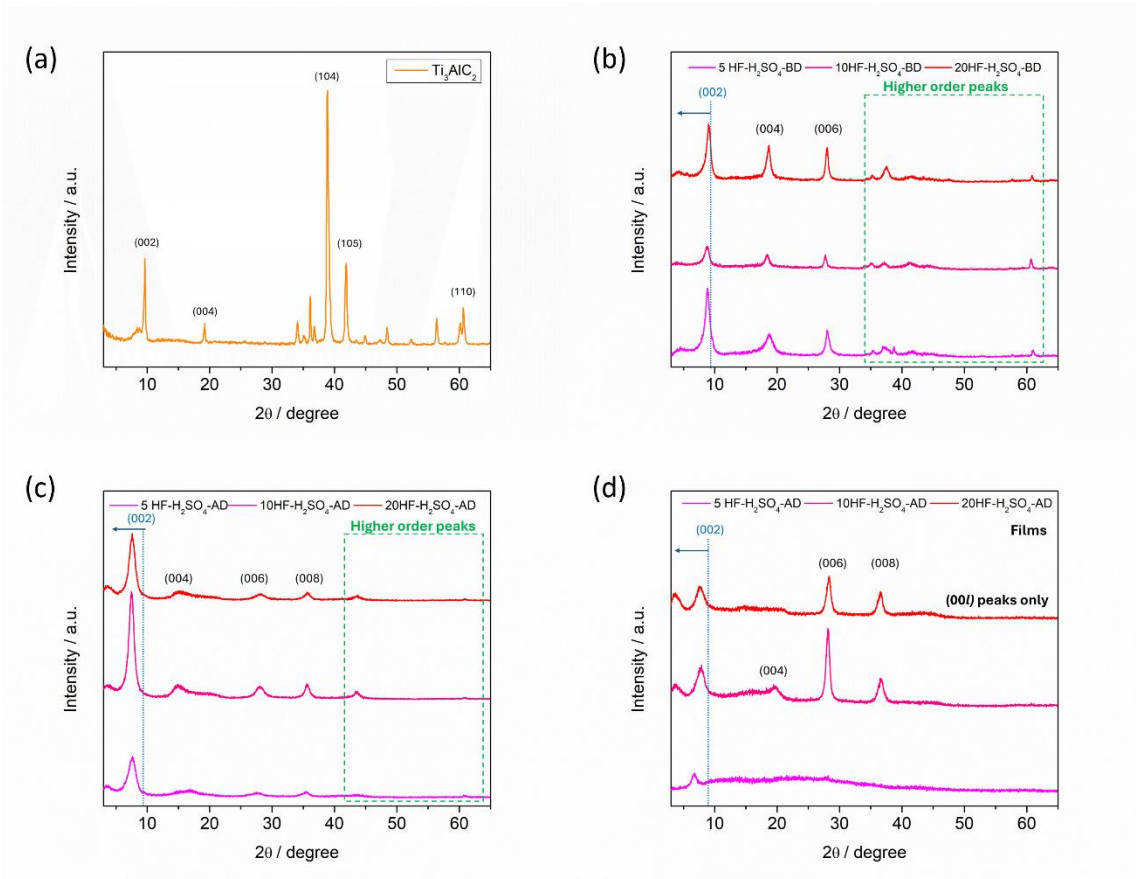

Figure 10 XRD Spectra; (a) Ti_3AlC_2 MAX phase, (b) XRD patterns of $Ti_3C_2T_x$ MXene powders etched at different HF volume ratios, (c) The XRD spectra of $Ti_3C_2T_x$ MXene powders fabricated after delamination with LiCl, (d)XRD spectra of $Ti_3C_2T_x$ MXene films fabricated after delamination with LiCl.

The position of the (002) peak gives information about the stacking order as well as the interlayer spacing of the $Ti_3C_2T_x$ layers (Anayee et al., 2020). The (002) peak of the Ti_3AlC_2 MAX phase was at 9.5°, which corresponds to a d-spacing of 9.3 Å. According to Figure 10 (b), the position of (002) peaks of 5 HF-H2SO4, 10 HF-H2SO4, and 20 HF-H2SO4 powder samples were 8.95º, 8.78º, and 9.04º, which correspond to an interlayer spacing of 9.9 Å, 10.1 Å, and 9.8 Å, respectively. The shift of the (002) peak

of the synthesized MXene powder to lower angles compared to the Ti_3AlC_2 MAX phase confirms the etching. It is observed that in the multilayer powder samples, the XRD pattern (Figure 10(b)) exhibits residues from the MAX phase, as indicated by the (104) plane. After delamination using LiCl as in Figure 10 (c), the positions of the (002) peaks were measured as 6.63º, 7.82º, and 7.65º and the corresponding d-spacing was calculated as 13.3 Å, 11.3 Å, and 11.6 Å using the 5 HF-H_2SO_4, 10 HF-H_2SO_4, and 20 HF-H_2SO_4 free-standing films, respectively. The higher-order peaks. According to Figs. 10 (b) and (c), no clear trend is observed with an increase in HF etchant concentration, although it is calculated without delamination. 10 HF-H_2SO_4 has the highest d-spacing, whereas after delamination with LiCl, the sample 5 HF-H_2SO_4 has a higher d-spacing. This also suggests that using an HF-H_2SO_4 etchant combination instead of an HF/HCl mixture facilitates the delamination of LiCl. The XRD pattern of the fabricated delaminated films exhibits only a signal for the (00l) planes, indicating successful delamination. The HF-H_2SO_4-AD sample has only shown a (002), which can be an indication of higher order of water molecules that could be structurally connected to the surface (Anayee et al., 2020; Naguib et al., 2012; Shekhirev et al., 2021).

4.1.3 XRD of Activated Carbon

XRD reveals the structural evolution of cigarette-butt–derived carbons as they progress from raw filter to carbonized and finally KOH-activated forms (S. Zhang et al., 2020). In Figure 11, the pristine butts (CB) show sharp reflections at 20–25°, characteristic of the crystalline cellulose-acetate domains in the filter matrix (Mahto et al., 2022). Carbonization erases these peaks, replacing them with a broad (002) and a very weak (100) shoulder near 43°, signatures of poorly graphitized carbon (CBC) (Y.-F. Wu et al., 2022).

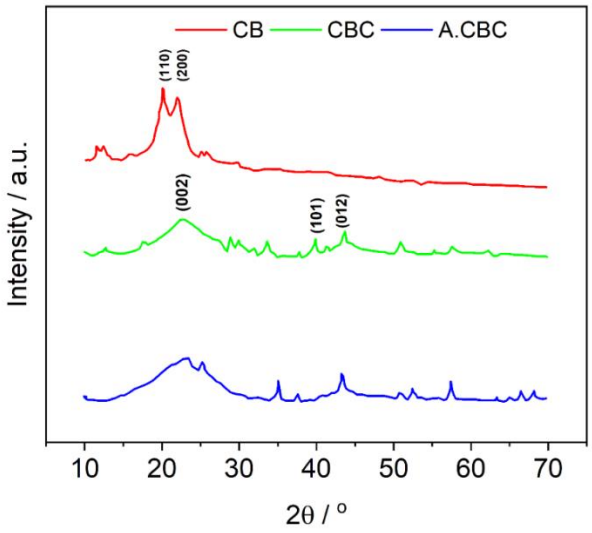

Figure 11 XRD patterns of waste cigarette butt (CB), waste–cigarette-butt–derived carbon (CBC), and KOH-activated carbon derived from waste cigarette butts (A.CBC).

4.2 Raman Analysis

4.2.1 Raman Analysis of Fe-doped ZnO

Firstly, the Raman Analysis of ZnO: Fe1-320 °C and ZnO: Fe1-750 °C was conducted. The ZnO: Fe1-320 °C has significant broadening, softening, and blue-shift effects. In principle, the P63mc symmetry of wurtzite-type ZnO gives five fingerprint Raman-active phonon modes for its bulk form. $2E_2(M)$ at 340 cm^{-1}, $A_1(TO)$ at 380 cm^{-1}, $E_1(TO)$ at 410 cm^{-1}, $E_2(high)$ at 436 cm^{-1} and a broad band $A_1(LO)$ between 500 and 630 cm^{-1}. All five bands are present in both samples, indicating the good formation of Raman-active modes. The changes in both spectra and deviations from the ideal Raman features are due to incorporation of Fe^{3+} ion in ZnO lattice and causing symmetry reduction, further symmetry reduction due to lower particle size Typical TO vibrational modes at

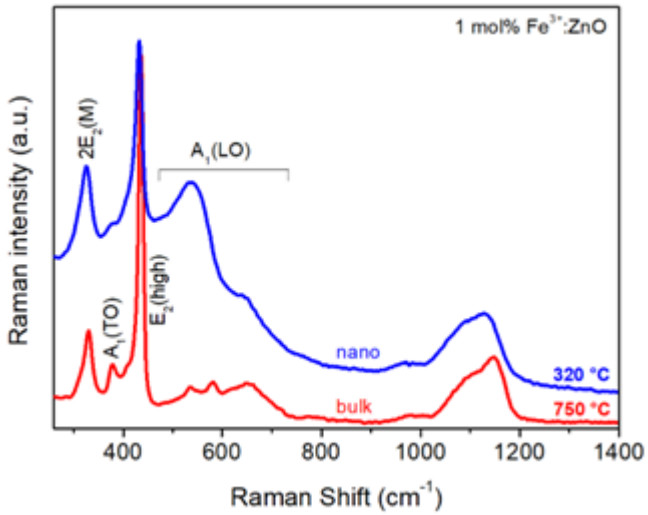

Figure 12 Comparison of Raman spectra for the ZnO: Fe1-320 °C and ZnO: Fe1-750 °C samples.

380 cm^{-1} and 410 cm^{-1} was detected and assigned to A_1(TO) and E_1(TO), respectively. The Raman mode at 340 cm^{-1} is generally attributed to second-order Raman processes and assigned to $2E_2$(M) mode. The broadband between 500 cm^{-1} and 630 cm^{-1} is referred to as anomalous because it is not often detectable in bulk ZnO samples. This broad Raman line A_1(LO) is typically observed in nano-sized ZnO, which is also present here. As it is very clear from Figure 12 that, by reducing the calcination temperature, hence the particle size, the broad line at 500–630 cm^{-1} becomes more prominent. Exactly when we double (x2) these modes result in 1000 and 1260 cm-1, we again observe in Figure 12. These doubled broad Raman lines, which are assigned to $2A_1$(LO). This can be attributed to a decrease in symmetry in the Wurtzite structure, which is strongly related to the existence of various point defect centers (surface and bulk defects) concerning particle size as in line with EPR ana PL results.

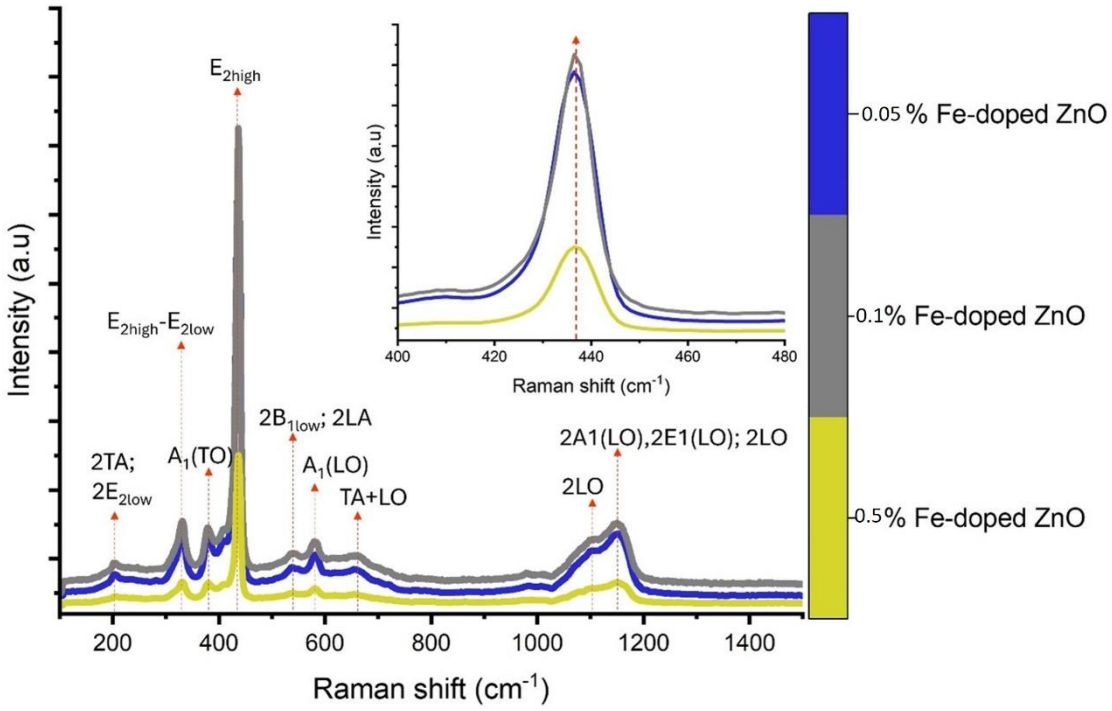

Figure 13 First-order and second-order Raman spectra were recorded at room temperature using a Renishaw inVia Raman spectrometer with an excitation wavelength of 532 nm. The Raman spectra of the Fe-doped ZnO samples reveal vibrational features across the 100–1500 cm^{-1} range. Changes observed within this spectral window reflect modifications in both the fundamental and overtone modes, providing insights into the structural and defect-related effects induced by Fe incorporation.

Raman spectroscopy serves as a sensitive, non-destructive technique to investigate the effects of Fe incorporation on the ZnO lattice. The hexagonal wurtzite structure of ZnO (space group P63mc), composed of four atoms per unit cell, supports 12 vibrational modes at the Brillouin zone center, including three acoustic branches (Aleinawi et al., 2025). In standard backscattering Raman measurements, ZnO is distinctly recognized by the strong presence of E_2 modes, which serve as key spectral fingerprints of its wurtzite phase (Aleinawi et al., 2025; Colak et al., 2024; S. Kumar et al., 2014). In case of Fe-doped ZnO, the characteristic Raman modes of the wurtzite phase (particularly the E_2 high mode around 437 cm^{-1}) are expected to remain present but often exhibit notable changes such as peak broadening, intensity variation, and slight shifts in frequency (Pandiyarajan, Udayabhaskar, & Karthikeyan, 2012; Sahai, Kumar, Agarwal, Olive-Méndez, & Goswami, 2014). These spectral modifications are typically attributed to lattice disorder, local strain, and increased defect concentrations induced by Fe^{3+} substitution at Zn^{2+} sites. Additionally, the A_1(LO) and E_1(LO) modes, which are more

sensitive to defects and carrier concentration, often become more pronounced in Fe-doped samples. In some cases, additional defect-related modes or multiphonon scattering features may also emerge, indicating enhanced phonon-defect coupling. Overall, Raman analysis provides clear evidence of structural perturbations and defect evolution associated with Fe doping in the ZnO matrix. As depicted in Figure 13, a sharp and intense peak near 437 cm^{-1} is assigned to the E_2(high) mode—an unmistakable signature of crystalline wurtzite ZnO (Altaf et al., 2023). Although the E_2(low) mode is not observed in this measurement, a band around 330 cm^{-1} commonly appears and is attributed to a second-order Raman process, specifically the E_2(high) – E_2(low) difference model (Altaf et al., 2023; Sahai et al., 2014). The polar nature of the wurtzite lattice leads to the splitting of the A_1 and E_1 optical phonon modes into transverse optical (TO) and longitudinal optical (LO) components. In this study, the A_1(TO) mode manifests as a weak band near 380 cm^{-1}, while the A_1(LO) mode emerges around 581 cm^{-1}, becoming more prominent when the crystallographic c-axis is aligned parallel to the sample surface. At higher frequencies, additional bands appear due to second-order Raman scattering processes, involving overtones and phonon combinations (Altaf et al., 2023; Colak et al., 2024; S. Kumar et al., 2014; Pandiyarajan et al., 2012; Sahai et al., 2014). One such mode, observed at approximately 660 cm^{-1}, corresponds to a TO + LO combination—originating from the simultaneous excitation of one TO and one LO phonon (Aleinawi et al., 2025). Furthermore, a weak shoulder near 1146 cm^{-1} is likely associated with 2LO scattering involving flat phonon branches along the A–L–M directions of the Brillouin zone (Aleinawi et al., 2025; Colak et al., 2024; S. Kumar et al., 2014; Pandiyarajan et al., 2012). This feature may also result from the superposition of 2A_1(LO) and 2E_1(LO) modes at the Γ point. The appearance, position, and intensity of these second-order modes provide valuable insight into the material's crystallinity, phonon–phonon interactions, lattice disorder, and the influence of dopants.

4.2.2 Raman Analysis of $Ti_3C_2T_x$ MXene

The Raman Spectroscopy analysis was carried out at the University of Pennsylvania, USA, using the same model described in the methods section. For each sample, data are collected at an acquisition time of 60 seconds using a 785 nm laser for three different spots. The Raman spectra of the samples before and after delamination are recorded

using powders and are given in Figure 14 (a) and (b). The Raman spectra of the $Ti_3C_2T_x$ MXene samples etched at different HF volume ratios were similar to typical $Ti_3C_2T_x$ MXene synthesized with HF-HCl etchants. With the excitation of 785 lasers, it was expected to see the first resonant peak which is coupled with the plasmonic peak and the results were in parallel. Besides the resonant peak (at 123 cm^{-1}), there are two other clear, sharp peaks around 200 cm^{-1} and 720 cm^{-1} attributed to the A_{1g}(Ti, O, C) and A_{1g}(C), respectively. As the HF volume increased in the etchant mixture the A_{1g}(C) peak shifted slightly to lower wavenumbers 722 cm^{-1}, 721 $cm^{-1,}$ and 720 cm^{-1}. There isn't any clear indication of the different surface terminations that would be caused by the H_2SO_4 used in the etchant mixture compared to the literature. After delamination, the wavenumbers corresponding to A_{1g}(C) increased which is due to the larger interlayer spacing (Sarycheva & Gogotsi, 2023).

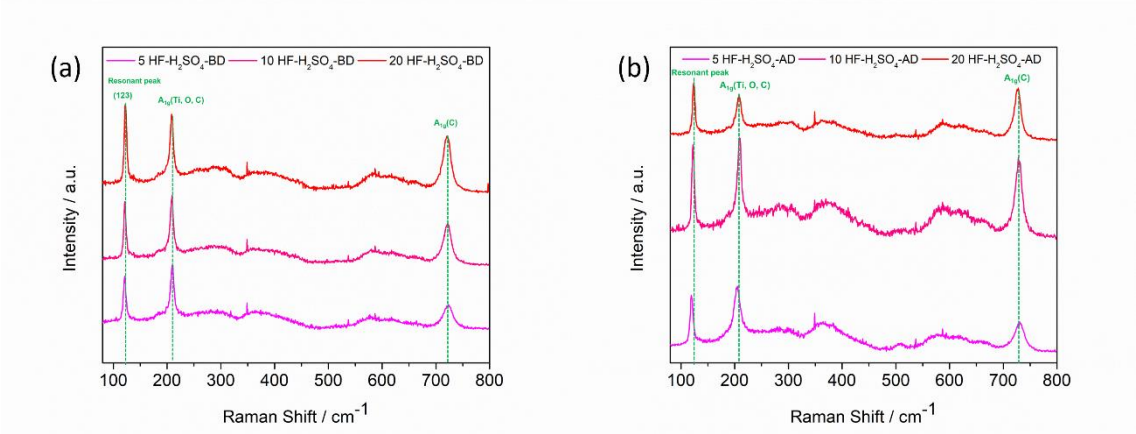

Figure 14 Raman spectra of the samples recorded at excitation with a 785 nm laser; (a) $Ti_3C_2T_x$ MXene powders etched at different HF volume ratios (b) $Ti_3C_2T_x$ MXene powders after delamination.

4.2.3 Raman Analysis of Activated Carbon

Raman spectroscopy is a method used to examine the structural properties of carbon materials, particularly to determine the ratio of amorphous to crystalline carbon phases. The Raman spectra shown in Figure 15 and the data presented in Table 6 compare the structural characteristics of the waste-cigarette-butt-derived carbon material (CBC) and the waste-cigarette-butt-derived KOH-activated carbon (A.CBC) samples. This analysis details how the carbonization and activation processes influence the graphite-like ordering, amorphous structure, and surface defects of the material. (Merlen, Buijnsters, & Pardanaud, 2017). In the Raman spectra, two primary bands characteristic of carbon materials appear: the D band (around 1380 cm^{-1}) and the G band (around 1610 cm^{-1}).

The D band represents structural disorder and defects in the carbon matrix, whereas the G band corresponds to the vibrational modes of graphite-like, well-ordered sp^2-hybridized carbon atoms. The intensity ratio of these two bands (I_D/I_G) is a critical parameter for assessing the degree of disorder and the proportion of graphite-like structures within the carbon material. The intensity ratio of D to G bands (I_D/I_G) greater than 1, this means that graphitization is low and there is higher degree of disorder (Takai et al., 2003).

Table 6 D and G band values and the I_D/I_G ratio of the waste-cigarette-butt-derived carbon material (CBC) and the waste-cigarette-butt-derived KOH-activated carbon (A.CBC)

	Raman Shift (cm^{-1})		
Malzeme	**D Band**	**G Band**	**I_D/I_G**
CBC	1379	1613	2.96
A.CBC	1391	1611	2.34

The CBC sample displays distinct D and G bands in its Raman spectrum. According to Table 4, its I_D/I_G ratio is 2.96. This high value shows that carbonization produced some ordered sp^2-hybridized carbon domains as organic compounds decomposed, yet the structure still contains considerable disorder (Shimodaira & Masui, 2002; Vali et al., 2024). Carbonization removed the organic constituents of the cigarette butts and increased graphitic ordering, but the elevated I_D/I_G ratio confirms that the amorphous phase was not fully eliminated and that substantial disorder remains which indicates only limited graphitization.

In contrast, the A.CBC sample exhibits a lower I_D/I_G ratio of 2.34. This decrease demonstrates that KOH activation reduces structural disorder and enhances graphitic ordering. During activation, KOH reacts with the carbon matrix, promoting the formation of micro and mesopores while simultaneously converting part of the amorphous phase into ordered sp^2 carbon (Vali et al., 2024). The drop in the I_D/I_G ratio for A.CBC therefore shows that activation not only expands the surface area but also creates a more ordered carbon framework.

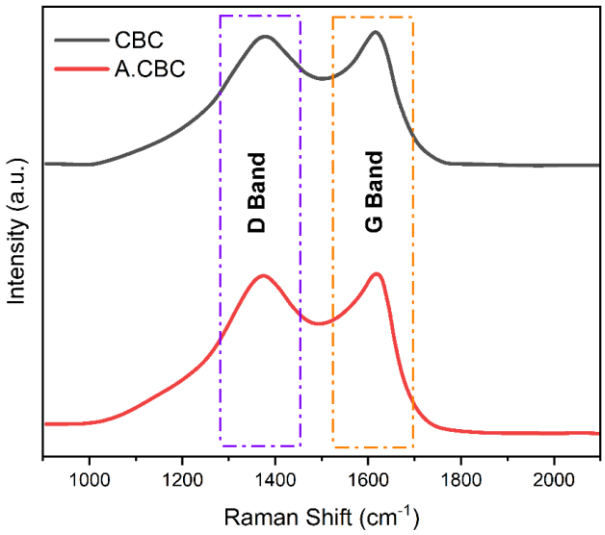

Figure 15 Raman spectra of carbon derived from waste cigarette butts (CBC) and KOH-activated carbon derived from waste cigarette butts (A.CBC).

4.3 SEM Analysis

4.3.1 SEM images of Fe-doped ZnO

We employed SEM to analyze the morphological structure of Fe-doped ZnO. To analyze the structure, we have selected two samples: ZnO: Fe1-320 °C and ZnO: Fe1-750 °C. We have chosen these two samples based on the nucleation and growth mechanism and EPR results, where we selected 320 °C (nano) as the temperature for smaller particles and 750 °C (bulk) as the temperature for larger particles. The SEM image of ZnO: Fe1-320 °C is shown in Figure 16. The size difference between the two Fe-doped samples is seen in the SEM images (Figure 16 and 17). The number of nanoscale particles in ZnO: Fe1-320 °C is significantly greater than ZnO: Fe1-750 °C. That is, the mean particle size of ZnO: Fe1-750 °C is in the micron scale (Figure 17), whereas the other, ZnO: Fe1-320 °C, is on the nanoscale (Figure 16). No definite particle shape is observed, which is due to the selection of the synthesis method.

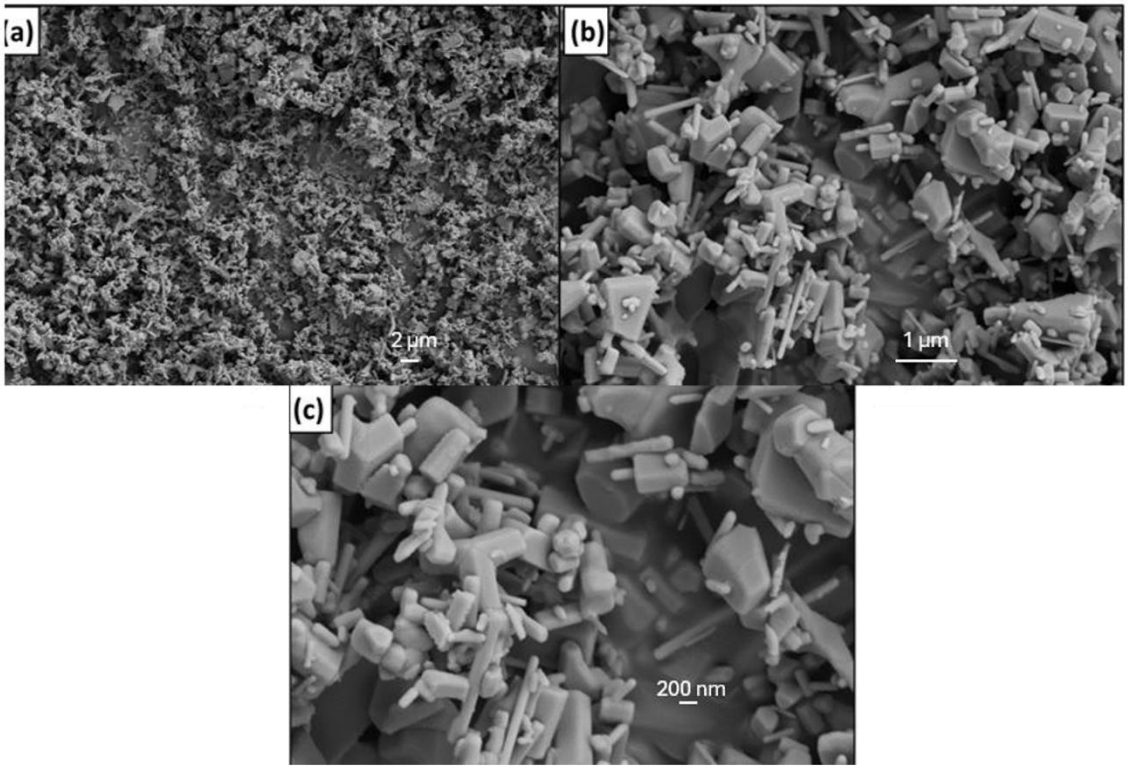

Figure 16 SEM images of ZnO: Fe1-320 °C: (a) 5kX, scale: 2 µm, (b) 30 kX, scale: 1 µm, (c) 50 kX, scale: 200 nm.

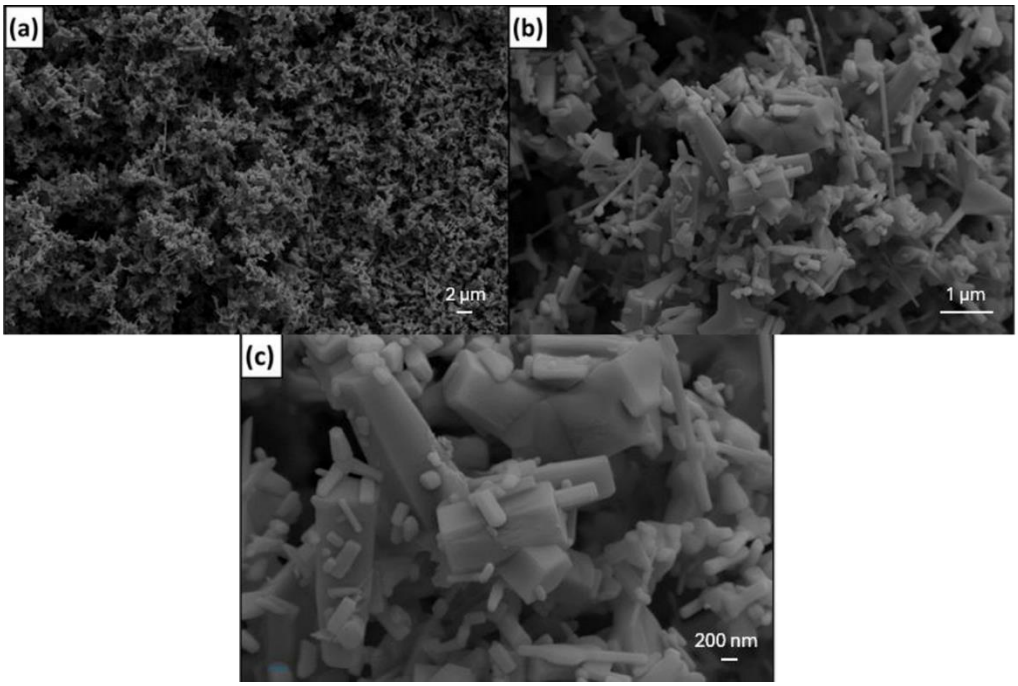

Figure 17 SEM images of ZnO: Fe1-750 °C: (a) 5kX, scale: 2 µm, (b) 25kX, scale: 1 µm, (c) 50 kX, scale: 200 nm

4.3.2 SEM of $Ti_3C_2T_x$ MXenes

The surface morphologies of the $Ti_3C_2T_x$ MXene samples were measured using Zeiss Supra 50 VP field emission SEM at 5kX magnification and given in Figure 18 and 19. SEM provides direct structural visualization that can confirm MXene formation, although etched specimens do not all exhibit identical morphologies. Because the earliest MXenes were produced by etching in highly concentrated HF, the resulting accordion-like architecture has become emblematic of successful synthesis, yet this characteristic motif does not capture the full diversity of multilayer MXene structures (Shekhirev et al., 2021). In Figure 18 (a) and (b), An accordion-like structure is observed using pure HF as an etchant as expected (Naguib et al., 2023; Naguib et al., 2012; Shekhirev et al., 2021). With the synthesis performed using an HF/HCl mixture, no precise openings have been observed before the delamination step, as shown in Figure 18 (c) below which is inline with the literature (Shekhirev et al., 2021).

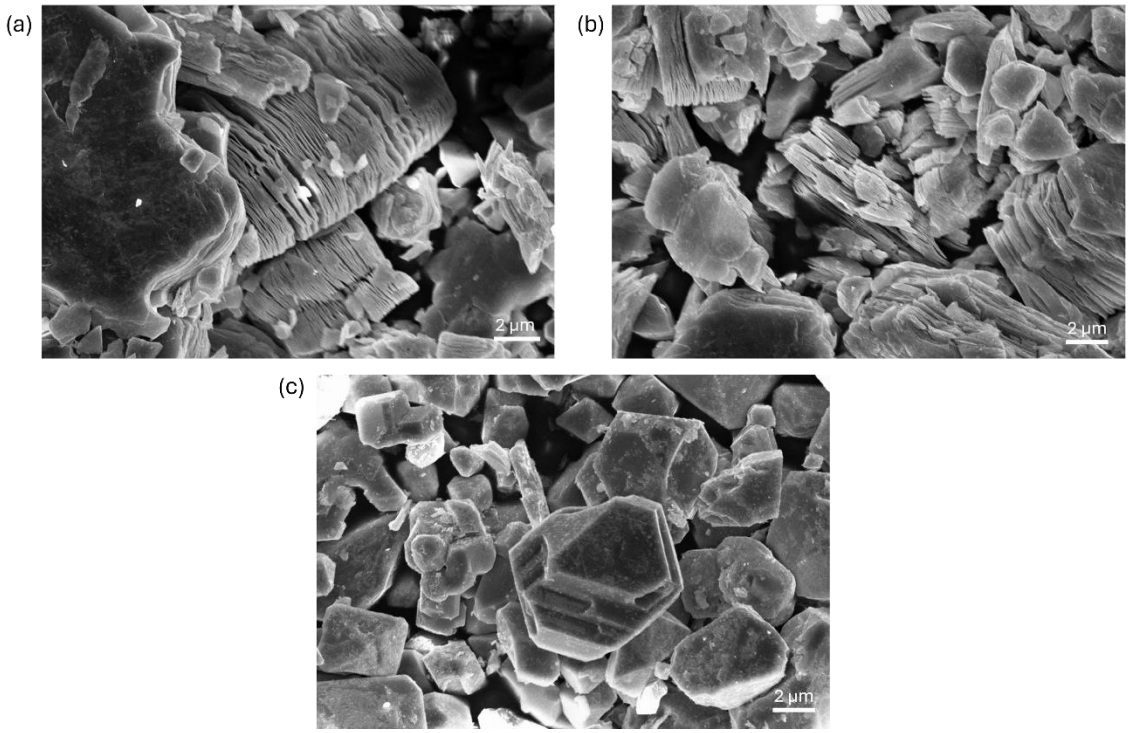

Figure 18 SEM images of the samples recorded at 5kX magnification etched using: (a) and (b) pure HF, (c) HF/HCl.

There are compact openings on the MXene layers which is in line with the work proposed by Anayee *et. al.* (Anayee et al., 2020), a clear accordion-like structure was not seen which is also expected due to the use of a lower concentration of % HF < 30

for Figure 19. SEM also used to detect oxide nanoparticles decorating the exterior of MXene layers, a signature of aggressive etching and surface oxidation. The detection of these oxides is not easy with X-ray diffraction analysis because of their nanoscale dimensions, low abundance, or amorphous structure (Shekhirev et al., 2021). However, the oxide formation is detectable with Raman spectroscopy through the observation of peak shifts. In this study, the SEM results and Raman analysis confirm that there is no oxide formation on MXenes.

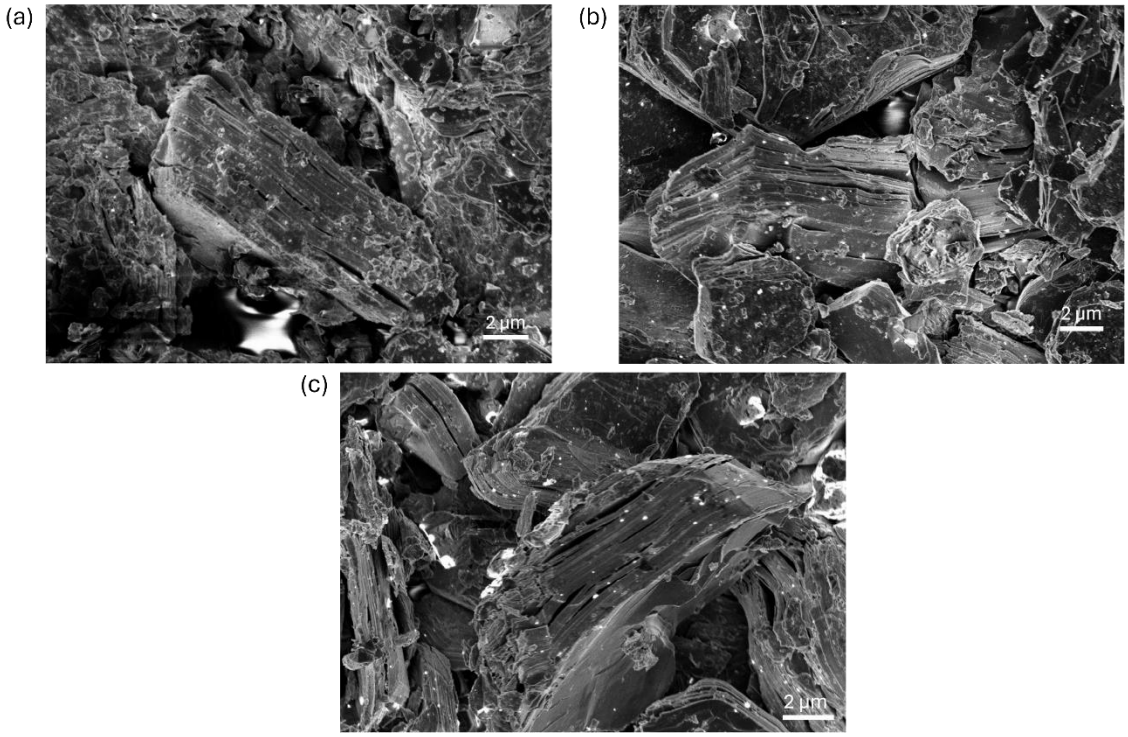

Figure 19 SEM images of the samples recorded at 5kX magnification: (a) 5 HF-H_2SO_4, (b) 10 HF-H_2SO_4, (c) 20 HF-H_2SO_4.

4.3.3 SEM Images of Activated Carbon

The SEM images presented in Fig.20 display the surface morphologies of the CB, CBC, and A.CBC samples. Examination of CB shows a dense, compact, and smooth surface in the SEM micrographs. The CB surface exhibits a fibrous morphology that reflects the natural structure of cellulose-acetate fibers. This morphology reveals a very compact surface that does not allow the formation of a porous network (Mahto et al., 2022). Consequently, raw cigarette butts have a low adsorption capacity, and no pronounced pore structure is present on their surface before carbonization/activation treatments. The

SEM images of the CBC sample reveal a more porous surface structure than that of CB. During carbonization, the organic compounds on the CB surface underwent thermal decomposition, producing a partial pore network. Consequently, CBC exhibits a less dense and more irregular morphology. Even so, the pores observed on CBC are limited in size and distribution, showing that carbonization initiated but did not fully develop pore formation. Although CBC's surface area is somewhat higher than CB's, this increase is modest and insufficient to markedly enhance the material's adsorption capacity. The A.CBC sample displays a surface morphology entirely different from that of CB and CBC in the SEM images. Owing to the activation treatments, the surface of A.CBC has transformed into a highly porous structure. During activation, KOH reacts chemically with the carbon matrix, promoting the formation of micro- and mesopores on the surface. The SEM micrographs reveal an irregular yet extensive pore network. This porous architecture is corroborated by BET analysis: the high surface area and increased pore volume of A.CBC correspond directly to the morphological changes seen in the SEM images. Notably, KOH activation appears to break down the dense carbon framework, producing a more open and accessible surface. This porous structure markedly enhances the material's adsorption capacity and surface reactivity. The effects of carbonization and activation reveal a strong correlation between the SEM images and BET results. During carbonization, the organic compounds on the CB surface undergo thermal decomposition, producing a partial pore structure. However, these pores remain limited, and the surface area does not increase appreciably. In the activation stage, KOH's chemical action creates many more pores within the carbon matrix, leading to a substantial rise in surface area. BET analysis shows that the surface area of A.CBC increases several-fold compared with CBC, a trend that aligns well with the porous morphology observed in the SEM micrographs.

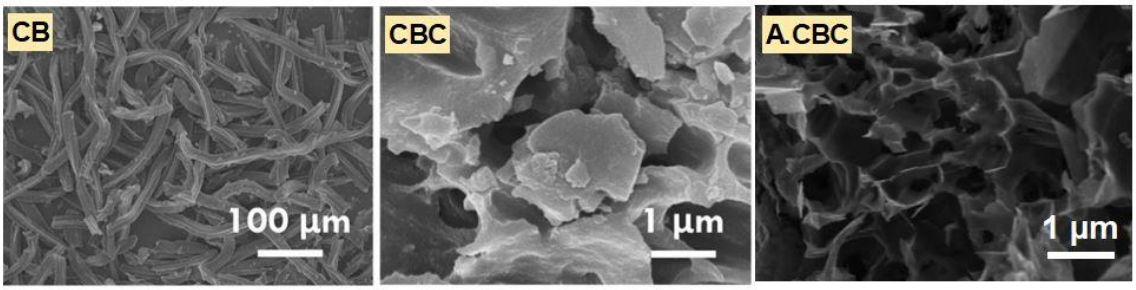

Figure 20 Scanning electron micrographs (SEM) of raw waste cigarette butts (CB), carbon derived from waste cigarette butts (CBC), and KOH-activated carbon derived from waste cigarette butts (A.CBC).

4.4 TGA Analysis

4.4.1 TGA analysis of Activated Carbon

The thermogram displayed in Figure 21 differentiates the behavior of the cigarette-butt (CB) from activated carbon (A.CBC), thereby quantifying the impact of chemical activation on their respective decomposition pathways and residual char yields (Saldarriaga et al., 2015). The CB thermogram exhibits three distinct mass-loss intervals: (i) 100–150 °C, where adsorbed water and low-boiling volatiles are released, reflecting the material's high moisture/volatile content; (ii) 200–400 °C, corresponding to the pyrolytic degradation of cellulose acetate and cleavage of carbonyl functionalities; and (iii) >400 °C, where the incipient carbon framework itself begins to decompose (Ranjkesh & Nasouri, 2023; Salman Masoudi Soltani & Sara Kazemi Yazdi, 2012; Yousef, Eimontas, Striūgas, Praspaliauskas, & Abdelnaby, 2024). The significant cumulative mass loss indicates that the pristine filter's thermal robustness is limited. In contrast, the A.CBC curve shows (i) a more minor 100–150 °C loss, implying that activation has already removed most residual moisture/volatiles; (ii) a significantly suppressed 200–400 °C loss, because KOH treatment has eliminated the majority of thermolabile organics and produced a chemically cleaner carbon matrix; and (iii) only minor degradation above 400 °C, signifying a far more stable skeleton (Al-Enizi, 2022). Consistently, the midpoint decomposition temperature (T_{50}) rises from 361 to 380 °C upon activation. KOH reacts with carbon during activation, etching extensive micro and mesoporosity that boosts BET surface area while simultaneously converting the framework into a more ordered and thermally resilient structure that enhances the material's suitability for energy-storage electrodes, water purification, and gas adsorption. Moreover, it should be noted that the acquired yield is comparably higher than that in literature (Blankenship & Mokaya, 2017; László, Bóta, & Nagy, 2000; Salman Masoudi Soltani & Sara Kazemi Yazdi, 2012).

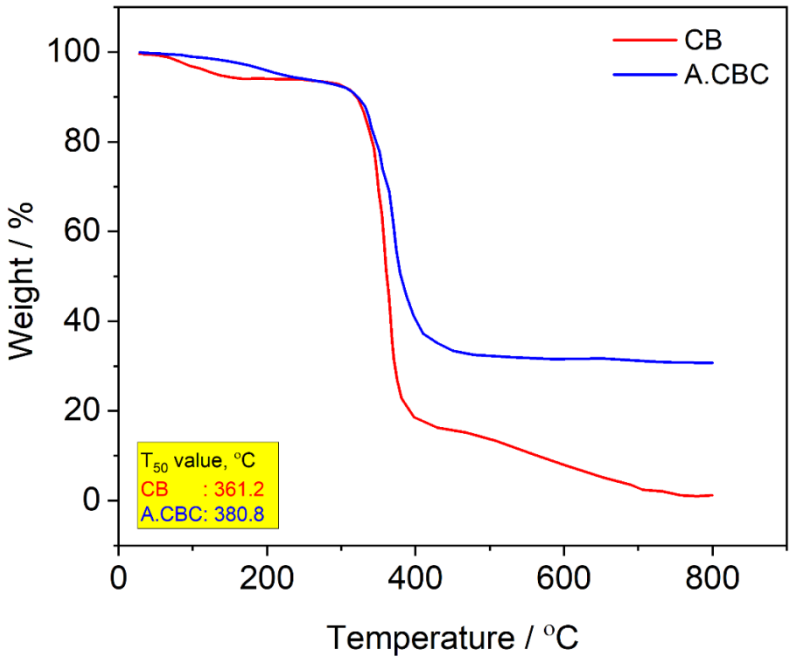

Figure 21 Thermogram of the acetone-treated and pure cigarette butt.

4.5 BET Analysis of Activated Carbons

As described earlier, the carbonization and activation processes were carried out in a horizontal tube furnace under an inert nitrogen atmosphere. As part of the optimization study, the specific surface area (m^2/g) and pore volume (cm^3/g) of each synthesized product were subsequently measured by BET analysis. Table 7 shows the S_{BET} and pore volume of the carbonized samples at 400, 450, and 500 ºC. The highest surface area and pore volume were measured from the sample CB-450. Hence, CB-450 is selected as the CB in this thesis and used as a precursor for further activation processes.

Table 7 BET results showing the surface area (S_{BET}) and pore volume measured from carbonized samples by varying temperatures.

Sample ID	S_{BET} (m^2/g)	Pore Volume (cm^3/g)
CB-400	356	0.1976
CB-450	457	0.3096
CB-500	375	0.2654

The CB-450 has been chemically activated in tube furnace 450 °C for 2 hours using 200 mL/min using KOH, H_3PO_4, and $ZnCl_2$, at three different mass ratios where m_{CB-450}: $m_{activating\ agent}$ will be 1:1, 1:2, and 1:3. After activation process, BET is used to analyze the S_{BET} and pore volume and the results were given in Table 8 below. Table 8 details how the type and ratio of activators affect the BET surface area and pore volume of the activated carbon. Chemical activation is a critical step for enhancing the pore structure and increasing the surface area of carbon materials. According to the table, KOH provides the highest surface area and pore volume compared with the other activators. Specifically, a 1:2 KOH ratio yields the best results, with a BET surface area of 1,198.5 m^2/g and a pore volume of 0.6584 cm^3/g. This ratio shows that KOH effectively develops micropores within the carbon framework and stabilizes the carbon skeleton. When the KOH ratio is increased to 1:3, the surface area drops from 1,198.5 m^2/g to 689.2 m^2/g. In contrast, the pore volume increases, indicating that higher activator ratios can cause pore collapse or coalescence. $ZnCl_2$ stands out as an effective activator for improving both micro- and mesoporous structures, but it does not deliver as high a surface area as KOH. At a 1:3 $ZnCl_2$ ratio, the best results are obtained, with a BET surface area of 954.1 m^2/g and a pore volume of 0.5332 cm^3/g. This ratio suggests that $ZnCl_2$ creates a balanced pore structure within the carbon framework. H_3PO_4, while promoting the formation of oxygen-containing functional groups on the carbon surface, provides a lower surface area and pore volume compared with the other activators. At a 1:3 ratio, H_3PO_4 achieves its best performance, with a BET surface area of 976.4 m^2/g and a pore volume of 0.4928 cm^3/g.

Table 8 BET results showing the surface area (S_{BET}) and pore volume of activated carbons.

Activating Agent	Activator Ratio (m_{CP}: m_{agent})	S_{BET} (m^2/g)	Pore Volume (cm^3/g)
1:1	KOH	822.7	0.4841
1:1	H_3PO_4	745.3	0.4215
1:1	$ZnCl_2$	689.2	0.3987
1:2	KOH	1198.5	0.6584
1:2	H_3PO_4	927.3	0.5127
1:2	$ZnCl_2$	878.6	0.4579
1:3	KOH	689.2	0.5223
1:3	H_3PO_4	954.1	0.5332
1:3	$ZnCl_2$	976.4	0.4928

The highest S_{BET} and pore volume were measured at 1198.5 m^2/g and 0.6584 cm^3/g, respectively. The measured S_{BET} is higher compared to other activated carbons in which KOH is used (Cheng et al., 2019; Hu et al., 2022; Shahrokhi-Shahraki, Benally, El-Din, & Park, 2021). Hence, all other measurements were conducted using KOH in a 1:2 ratio.

4.6 Photoluminescence (PL)Analysis

4.6.1 PL Analysis of Fe-doped ZnO

To supplement our EPR studies and deepen our understanding of the electronic structure, we performed PL measurements. While UV–visible PL spectra have been widely reported, the precise origins and mechanisms of the luminescent centers remain unclear, and some proposed assignments lack convincing experimental validation (Janotti & Van de Walle, 2009; Özgür et al., 2005). All PL analyses of the ZnO precursor and Fe-doped samples were measured with an excitation wavelength of 320

nm at room temperature. PL is highly sensitive to the defect structures, especially for luminescent samples. Thanks to the photoluminescence property of ZnO, we can detect emission spectra of defects in the visible light range. In principle, PL has two significant emission signals: i) electron-hole recombination, which corresponds to the band gap energy, and ii) defect-related broadband visible light emission. Since these two emissions can be distinguished, we may have valuable information not only about the defects but also about the band gap mechanism of each sample. Firstly, to use as a reference, the PL spectra of the ZnO precursor are measured and given in Figure 22. One sharp signal is seen at 370 nm, which is the near-band-edge (NBE) emission, or in other words, e^--h+ recombination of the ZnO. This emission gives directly the band gap of the ZnO, where we obtained the value of 3.37 eV, which is typical for Wurtzite-type bulk ZnO crystal (Gurylev & Perng, 2021).

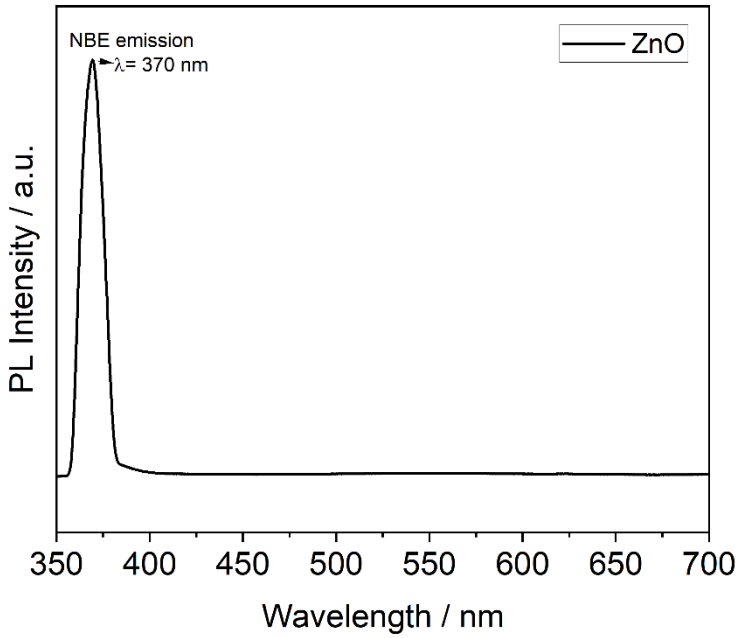

Figure 22 The PL spectra of the used ZnO precursor measured at an excitation wavelength of 320 nm at room temperature showing the NBE emission observed at 370 nm.

It is essential to understand the PL and EPR spectra of ZnO to use them as a fundamental basis for understanding the effects of Fe-doping. This will be highly crucial, as single-phase detection is observed on XRD (except for high concentration

dopings, such as 1% and 3%). The PL spectrum of ZnO features a sharp near-band-edge UV peak accompanied by a broad, defect-related visible emission spanning green, yellow, orange, and red wavelengths. The green component has been linked to a combination of intrinsic defects, including oxygen vacancies (V_O), zinc vacancies (V_{Zn}), and donor–acceptor pair recombination. Moreover, numerous investigations have shown that both the synthesis route and the resulting particle morphology can significantly affect the energy position and intensity of these visible emission bands (Erdem, 2014; Kaftelen et al., 2012; Repp & Erdem, 2016). TM ion doped ZnO produces violet light (380–450 nm), blue light (450–495 nm), and green light (495–570 nm) (X. Huang, Zhang, Tay, Venkatesan, & Chua, 2013). All curves in Figure 23 that belongs to ZnO: Fe1 at different temperatures contain a weak near-band-edge (NBE) peak of ZnO ~ 400 nm and a much broader green-yellow band peaking around 520–540 nm, which is ascribed. At the lowest calcination temperature (250 °C) the defect band is both the most intense and the broadest, signaling a high concentration of oxygen vacancies, interstitials or dangling bonds that funnel carriers into radiative deep-level recombination. As the treatment temperature rises to 320 °C and 400 °C the entire spectrum attenuates and slightly narrows, but the reduction is more pronounced for the defect band than for the NBE feature, indicating progressive healing or annihilation of non-stoichiometric sites while the intrinsic lattice remains largely intact. Calcining at 750 °C and especially 900 °C further quenches the deep-level emission to a small shoulder around 560 nm. A similar trend is observed for the EPR signal where $g \sim 2.52$, $g \sim 2.14$, and $g \sim 2.14$ due to Fe^{3+}. It should be noted that on the XRD only a single phase has been observed for ZnO. Here, it is observed that the sensitivity of EPR enables us to confirm the doping of Fe^{3+} ions and simultaneously create luminescent defect centers, as indicated by the PL spectra around 560 nm. Additionally, it is worth noting that as the calcination temperature increases, the intensity of the PL signal decreases. There is only one exception here for ZnO: Fe1-320 °C, which can be correlated with EPR (Kaftelen et al., 2012). In the literature, a red photoluminescence stems from singly ionized oxygen vacancies (V_o^+), were seen at around 650 nm is seen (Alvi, Ul Hasan, Nur, & Willander, 2011; Kaftelen et al., 2012). Conversely, no signal around 650 nm is detected, which is in line with the EPR results. Also, as discussed earlier, it is known that according to DFT calculations based on analysis of intrinsic defects in Fe-doped ZnO, the formation of the Fe_{Zn}-V_{Zn} complex is the most favored interaction compared to Fe_{Zn}-V_O and Fe_{Zn}-V_{Zn}-V_O (Debernardi & Fanciulli, 2007).

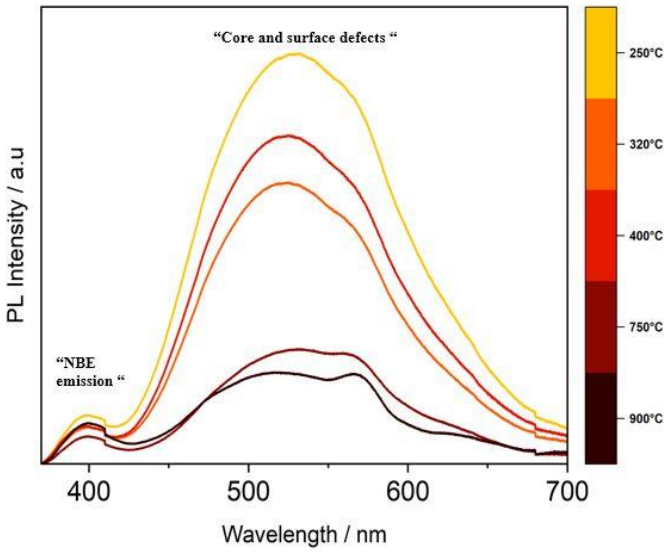

Figure 23 PL spectra of ZnO: Fe1 at different temperatures.

Here, we observe that as the doping concentration increases from 0.1% to 0.5%, the emission peaks (mainly ~ 467 nm, 536 nm, 565 nm, and 620 nm) become more prominent, as shown in Figure 24. This trend aligns with the XRD findings: as the doping concentration increases, crystallinity decreases, as determined by XRD results. PL results thus confirm the formation of defects due to the incorporation of Fe ions into the ZnO lattice (Sharma, Dutta, Pandey, Layek, & Verma, 2009).

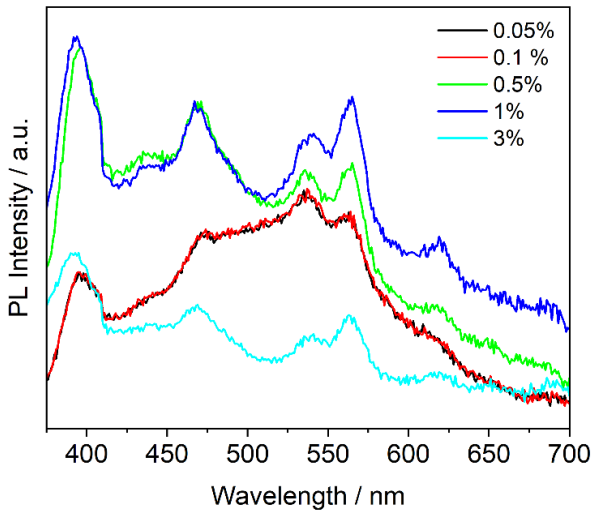

Figure 24 PL spectra of ZnO: Fe1 at varying dopant concentrations.

4.6.2 PL Analysis of $Ti_3C_2T_x$ MXene

An FS5 Edinburgh Instrument Spectrofluorometer was used at room temperature to measure the fluorescence spectrum of both samples, ranging from 270 to 700 nm. Figure 25 shows the PL spectra of the synthesized $Ti_3C_2T_x$ MXene samples in film form. The powder form was also analyzed; however, no signal was detected. Since $Ti_3C_2T_x$ MXenes do not exhibit intrinsic photoluminescence due to their metallic character (Sarycheva & Gogotsi, 2023). $Ti_3C_2T_x$ MXene was prepared following the method reported by Tang *et al.* (Tang, Zhou, & Shen, 2012) the initially formed oxide phase typically remains amorphous and cannot be detected via XRD. Nonetheless, it is well established from previous studies that TiO_2 containing significant defects can exhibit photoluminescence. The prominent PL peak near 630 nm indicates the presence of an oxide phase with photoluminescent properties. In this study, no photoluminescence has been analyzed in both PL and Raman analysis (Sarycheva & Gogotsi, 2023). Thus, the results also confirm that no oxide formation has been detected, which is in line with the SEM images.

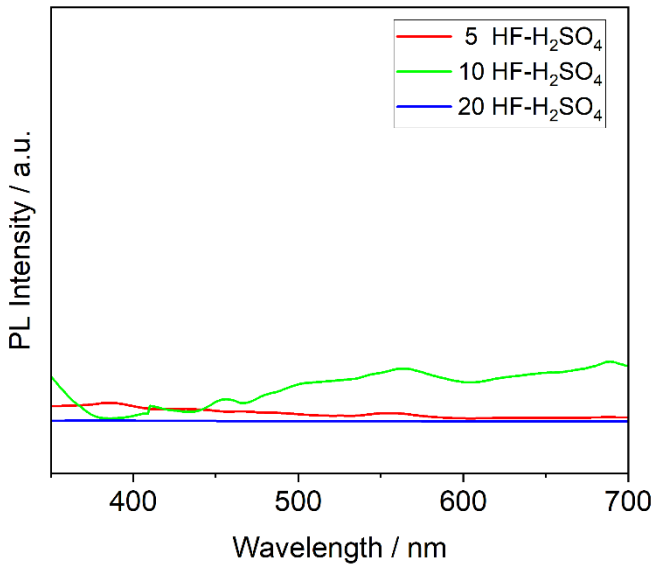

Figure 25 The recorded PL spectra of the delaminated $Ti_3C_2T_x$ MXene films etched using HF-H_2SO_4 etchant mixture.

4.7 EPR Analysis

4.7.1 EPR Analysis of Fe-doped ZnO

The Fe^{3+} ion has an electronic configuration that ends with d_5, which will give five allowed electronic transitions in EPR. A free Fe^{3+} ion has a $3d^5$ configuration with five unpaired electrons. Because its orbital angular momentum is quenched (L = 0), the ground term is $^6S_{5/2}$ (S = 5⁄2) (Aksel, Erdem, Jakes, Jones, & Eichel, 2010; Soares et al., 2022). In a crystal field, this spin sextet splits into three Kramers doublets under the internal electric field gradient. An applied magnetic field then separates these further into six Zeeman sublevels. Hyperfine effects from ^{57}Fe are ignored, since the only isotope with a non-zero nuclear spin (^{57}Fe, I = 1⁄2) makes up just 2.1 % of natural iron and produces no observable lines in the spectra (Aksel et al., 2010). This is due to Zeeman splitting and so-called fine structure (FS). The allowed transitions due to FS have four outer transitions m_s=|5/2,3/2>; |3/2,1/2>; |-1/2,-3/2>; |-3/2,-5/2> and one central transition (m_s =|1/2,-1/2>). The main difference between EPR and PL is that in EPR, we observe only the defect centers that are EPR active, namely, the paramagnetic ones. Fe^{3+} with its S=5/2 spin number is anyway paramagnetic. The intrinsic defects, such as vacancies and interstitials, should be singly or doubly ionized to become paramagnetic and observable in EPR. But in PL, all defect centers, whether para or diamagnetic, can be detected. Therefore, it is not easy to correlate the concentration of defects one-to-one by comparing the EPR and PL spectra. The challenge of pinpointing and assigning intrinsic defects both within the bulk and at the surface of ZnO nanocrystals produced by various methods is partially addressed by a semi-empirical core–shell framework. Using this model, Erdem *et al.* (Erdem, 2014) have shown that our ZnO electrode exhibits two separate EPR signatures (in both X- and Q-bands) arising from assemblies of paramagnetically active defects, namely singly ionized oxygen vacancies (V_{O^+}), zinc vacancies (V_{Zn}), zinc interstitials, and oxygen interstitials. Depending on whether the trapped charge resides in the more tightly bound core of the nanocrystal (where enhanced spin–orbit coupling shifts the g-value down to 1.962) or at the surface (where delocalized electrons behave nearly as free carriers, yielding a g-value of 2.006, close to the free-electron value of 2.0023), two distinct EPR centers

emerge. Moreover, these defect centers donate charge carriers, dramatically boosting the conductivity of the ZnO sample (Erdem, 2014; Kaftelen et al., 2012). Nevertheless, EPR gives us at least useful information on the localization of the defect centers, both for intrinsic and extrinsic (here Fe^{3+}) defects. Also, competing effects with Fe^{3+} and the intrinsic defects can be monitored, which enables us to exert extensive control of the concentration of metal ions (Baraki, Zierep, Erdem, Weber, & Granzow, 2014; Ruf, Repp, Urban, Thomann, & Erdem, 2016). Intrinsic defects (surface and core) and extrinsic defects (due to Fe^{3+} incorporation in the lattice) can interplay depending on many parameters. Here, the adjustment mechanism is the synthesis route based on the effect of calcination temperature was analyzed for ZnO: Fe1 samples as in Figure 26.

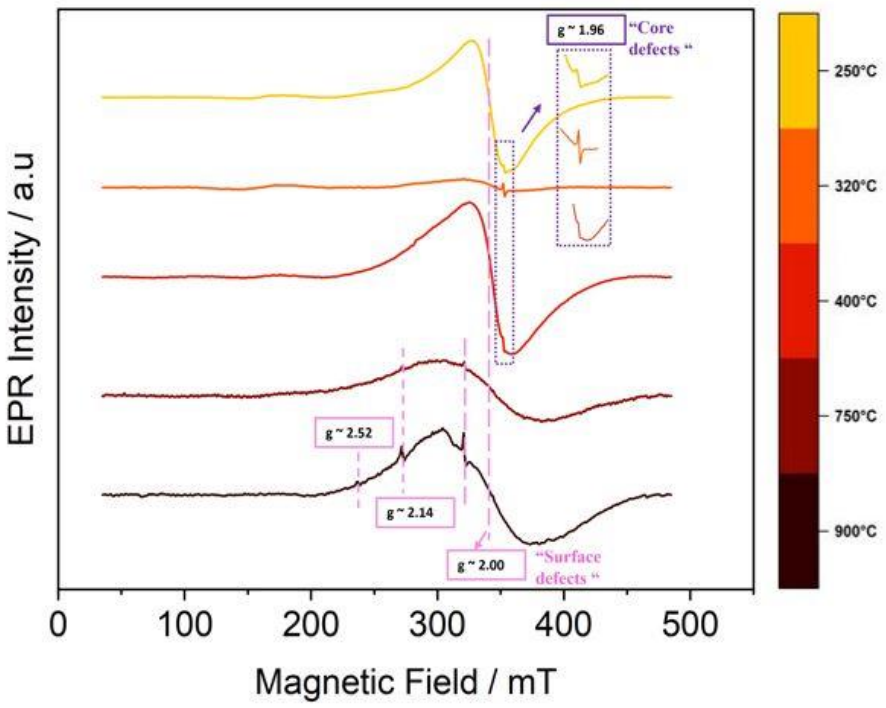

Figure 26 The EPR spectra of ZnO: Fe1 at varying temperatures.

Obviously, at lower calcination temperatures, the crystallinity of ZnO is almost started and therefore fewer Fe ions are accommodated in the ZnO lattice. In this case, we still observe intrinsic defect signal of core defects, which arises at g = 1.962. Once we increase the calcination temperature up to 750 °C, the intrinsic core defect signal vanishes, and distinct Fe-dominated EPR signals originate. For the sample ZnO: Fe1-750 °C we observe three magnetically inequivalent paramagnetic centers. The first one

has the effective g-factor (g = 4.25) and it gives the g-factor of Fe^{3+} associated with the oxygen vacancy. This indicates strong distortion from tetragonality, and more or less, it is the sign of the rhombic symmetric portion. The signal at g = 2.002 has a similar g-factor to that of free electrons (well-known gfree-electrons = 2.0023); thus, they are isolated Fe ions in a lattice where substitution occurs without any vacancy defects around. In this case, the orbital contribution to the spin-orbit coupling is almost zero, and we only have a contribution from the spins (S=5/2, L=0 from the Hund's rule). Finally, a broad Gaussian line represents the oxidation behavior, where high calcination temperatures may cause the formation of the iron oxide phase. Mostly metal oxides exhibit broad Gaussian lines when located on grain boundaries. Such phases cannot be determined via XRD, whereas the sensitivity of EPR is higher than that of XRD. EPR gives local configuration or environment information. Moreover, to analyze the effect of dopant concentrations, we have re-conducted EPR measurements as in Figure 27. It can be seen that EPR is a highly sensitive tool for the detection of paramagnetic defect centers even at low concentrations. Since EPR is a highly sensitive technique, as the concentration of paramagnetic ions increases, the detection possibilities decrease due to dipolar broadening of the signal caused by spin-spin interactions. Here, one can observe the effect of dipolar broadening starting from sample ZnO: Fe1-1000 °C. This is also the reason why we have limited the doping maximum to 3 %. However, below 0.1 %, the Fe^{3+} signals can be easily observed.

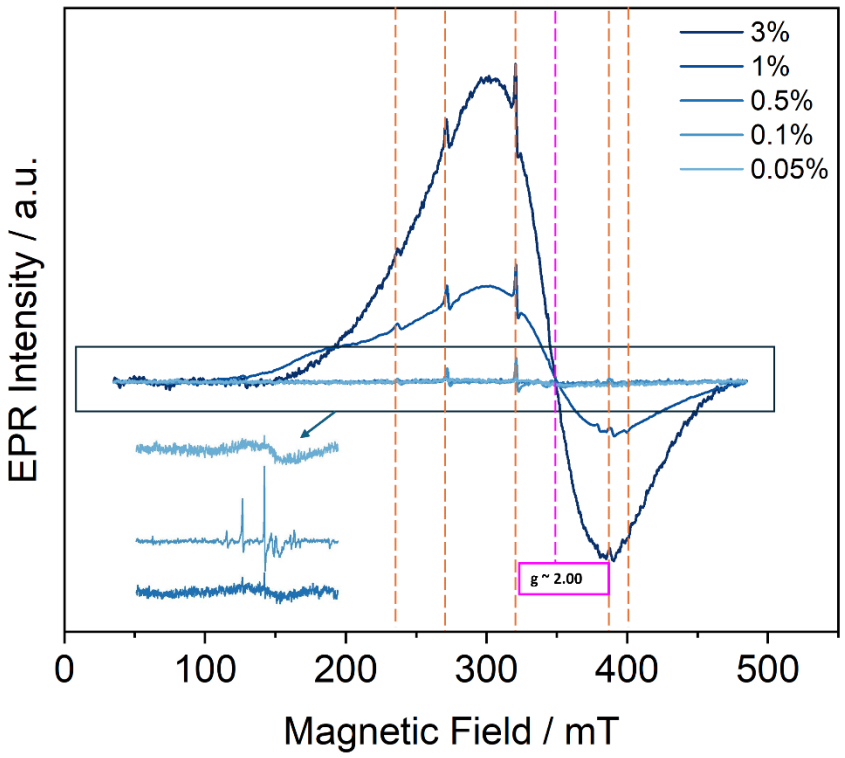

Figure 27 The EPR spectra of ZnO: Fe at varying dopant concentrations.

The synthesized powder of ZnO: Fe1000 °C was mechanically milled to investigate the effects of milling on the paramagnetic defects by introducing surface defects by the mechanical strain produced through high-energy ball milling process. A high-energy planetary ball milling (HEBM) equipment (Fritsch, Pulverisette 7 Premium Line Planetary Micro Mill) was employed at room temperature with zirconia vial and balls at following conditions: milling times of 2 hours, rotation speed of 500 rpm, Ø 2 mm zirconia balls, 45 ml zirconia vial, ball-to-powder weight ratio was 10:1. The ball-milled sample were names as ZnO: Fe1-1000 °C-BM and its EPR spectra was given in Figure 28. It is seen that the signal becomes a broad Gaussian peak, and no more Fe^{3+} signals were resolved due to the spin-spin interaction between the Fe^{3+} ions.

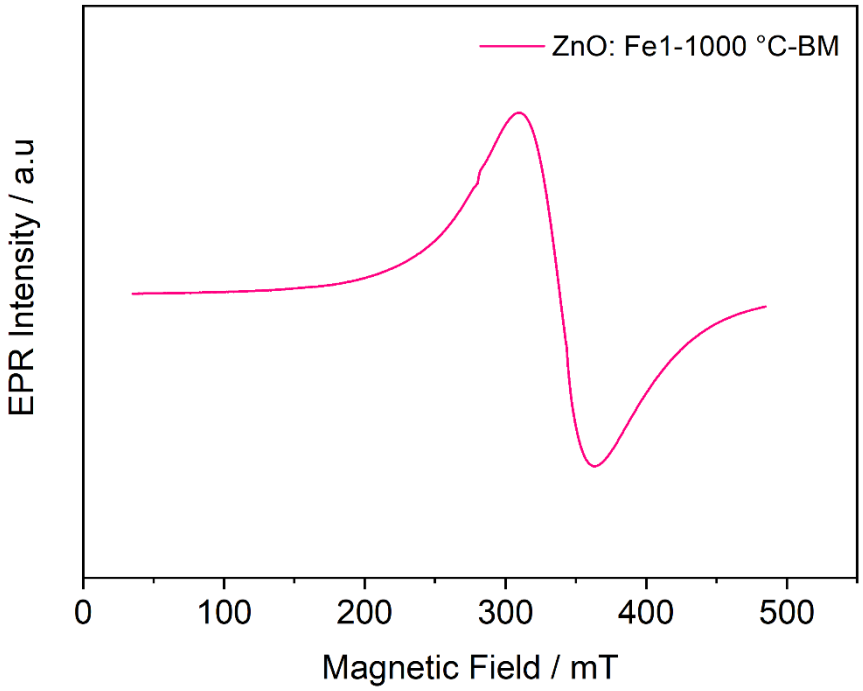

Figure 28 The EPR spectra of ZnO: Fe1-1000 °C-BM.

In Figure 29 (a) and (b), the X- and Q-band EPR spectra of ZnO:Fe for different doping concentrations (0.1 mol% % and 1 mol% %) at various calcination temperatures of 320, 360, 750, and 1000 ˚C are presented, respectively. The presence of Fe, even in low concentrations, significantly broadens the EPR spectra, as observed in both the X- and Q-band EPR spectra of samples calcined at lower temperatures. For ZnO: Fe1-750 °C, a new feature appears superimposed on the broad EPR signal, indicating Fe^{3+} ion incorporation in the ZnO lattice. By further increasing the calcination temperature to 1000 °C and decreasing the Fe concentration by a factor of 10, the interaction between the Fe centers is diminished, as denoted by the disappearance of the broad EPR signal. The fine-structured lines evidenced by the Q-band EPR measurements presented in Figure 29 (b) are well defined. The Fe^{3+}, similar to Mn, is expected to site substitute the Zn sites in the ZnO lattice with a C_{3v} symmetry. The X -and Q-band EPR investigation for ZnO:Fe has been previously reported by Açıkgöz *et al.*(Açıkgöz et al., 2014). The reason to go to higher frequencies, thus the higher magnetic field strengths, is to resolve any anisotropies or to see any hidden Fe or Mn centers. While in the doping process, Fe or Mn ions may integrate into the lattice at different configurations. Such various localizations of doping elements reflect magnetically inequivalent ions although they

are the same ion. Thus, one may expect two or three different Fe or Mn centers. For instance, in Fe doping, we see a broad Gaussian line which stems from the Fe-Fe (spin-spin) interactions. In the ZnO: Fe01-1000 °C sample (the very bottom one), tetragonally split fine structure lines are visible. This is one of the advantages of the Q band that we resolved all the EPR lines. The simulation given in Figure 30 revealed the g-factor of 2.002 and zero field splitting parameter (or, in other words, fine structure parameter) D of 610 MHz.

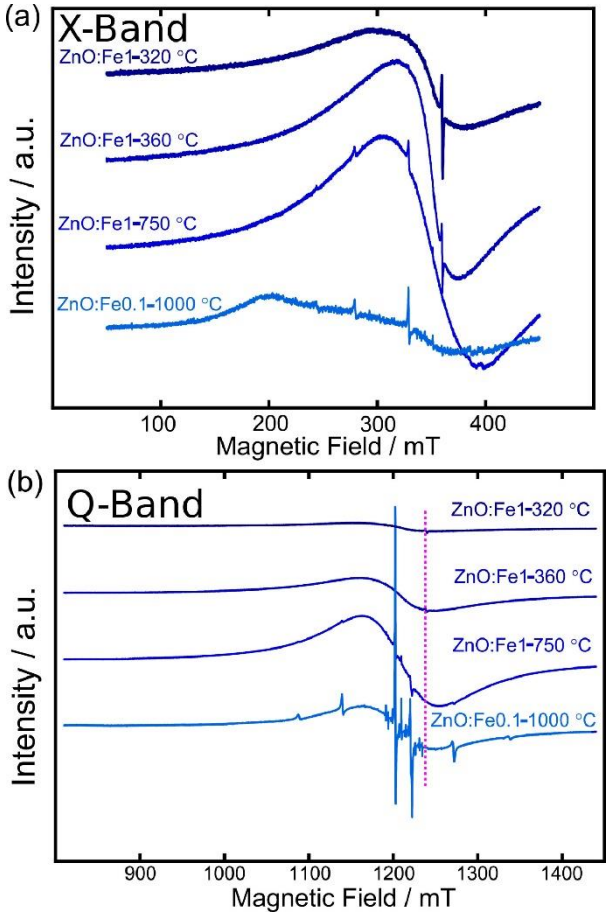

Figure 29 The EPR spectra of ZnO: Fe samples: (a) X-band, and (b) Q-band.

Figure 29 (b), obtained in Q-band, shows the incorporation of Fe^{3+} cations in ZnO. The observed EPR resonances in Figure 25, from the low to the high magnetic field region, indicate the $m_S \Leftrightarrow m_{S+1}$ transitions. The one in the middle (central transition) is the most intense. The simulation result, presented in Table 9, confirms once again the incorporation of Fe^{3+} cations, as they match extraordinarily with the literature (Chakraborty, Shirodkar, Gohil, Waghmare, & Ayyub, 2013). A second spin system was

applied for the simulation, with a g-value of 2.010 (1) and a substantial line width of 109 mT. This broad EPR signal was associated with ferromagnetic exchange interactions or very strong spin exchange interactions between the Fe^{3+} cations and a Fe_2O_3 secondary phase, which may form in the grain boundaries during the preparation stage of the material (D'Ambrosio et al., 2015; Raita et al., 2012; Tribollet, Behrends, & Lips, 2008; Y. Zhang et al., 2006).

Table 9 The simulation parameters of the ZnO: Fe01-1000 °C sample.

Spin	5/2	1/2
***g*-value**	2.0062	2.0101
[D E] / MHz	[1853 10.5]	-
A / MHz	-	-
LWPP [G L] / mT	[0.3 0.2]	[101 8]

As reported by Cabrera-Baez *et al.* (Cabrera-Baez et al., 2021), doping ZnO with magnetic ions leads to interesting changes in the electronic structures. The Fe^{3+} ions occupying the Zn sites have strong ferromagnetic interactions due to their high magnetic moment (S = 5/2) (Heitz et al., 1992; Malguth, Hoffmann, & Phillips, 2008). The Fe^{3+} centres and their presence at Zn core, interstitial, and surface sites, as well as corresponding g-factors, were analyzed with EPR spectroscopy, which shows similar results as presented in our study and therefore strongly supports the confirmation of the presence of Fe^{3+} in the ZnO structure (Cabrera-Baez et al., 2021). The XRD results also confirm the Fe^{3+} ions substitution in the Zn lattice. According to Karmakar *et al.*, hole doping is crucial for stabilizing ferromagnetism in Fe-doped ZnO and is facilitated through Zn vacancies. Moreover, there are cation vacancies in Fe-doped ZnO nanoparticles which can dope holes into the system and be confirmed by the EPR measurement via the presence of Fe^{3+} (Karmakar et al., 2007).

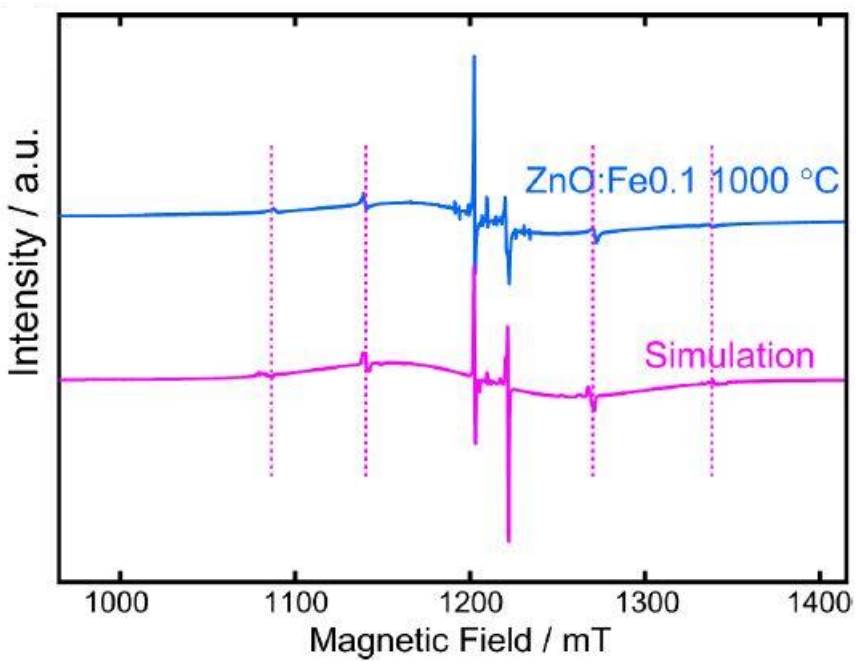

Figure 30 Simulated Q-band EPR spectra of ZnO: Fe01-1000 °C.

EPR spectroscopy exhibits exceptional sensitivity in identifying paramagnetic defects, enabling the distinction and characterization of stable or metastable energy states. Furthermore, it provides detailed information regarding the microscopic origin of these defects, elucidating their active role in material properties. However, challenges arise when assigning the S=1/2 defects, as different EPR spectra may be attributed to the same defect center or the same spectrum may be assigned to different paramagnetic species. Such problems mostly occurred in case of metal oxides which have intrinsic defect centers with electron spin of ½ due to the trapping of unpaired electrons in wide band gap. This creates difficulties in understanding the nature and origin of these defects, leading to potentially incorrect assignments. Moreover, conventional X-band (9.5 GHz) EPR spectroscopy may not be sufficient to resolve high-degree anisotropies or high-value field zero-field parameters, necessitating the application of ultra-high-field EPR spectroscopy to address these issues effectively. Thus, the ultra-high-field EPR measurements were performed at National High Magnetic Field Laboratory, Tallahassee, USA. The EPR measurements were performed at 112, 216, 324 and 406 GHz spectrometers as in Figure 31. It was observed that higher magnetic fields resulted in improved resolution. Additionally, the high-field EPR results provided accurate g-factor values, whereas X-band EPR alone, due to high zero-field splitting, failed to resolve all electronic transitions. The high-field EPR analysis performed for ZnO: Fe01-

1000 °C and ZnO: Fe1-1000 °C samples, it is seen that for ZnO: Fe1-1000 °C the Fe^{3+} ions are not resolved as ZnO: Fe01-1000 °C which shows the sensitivity of EPR. As frequency increased, the detection of EPR defect centers resolved clearly.

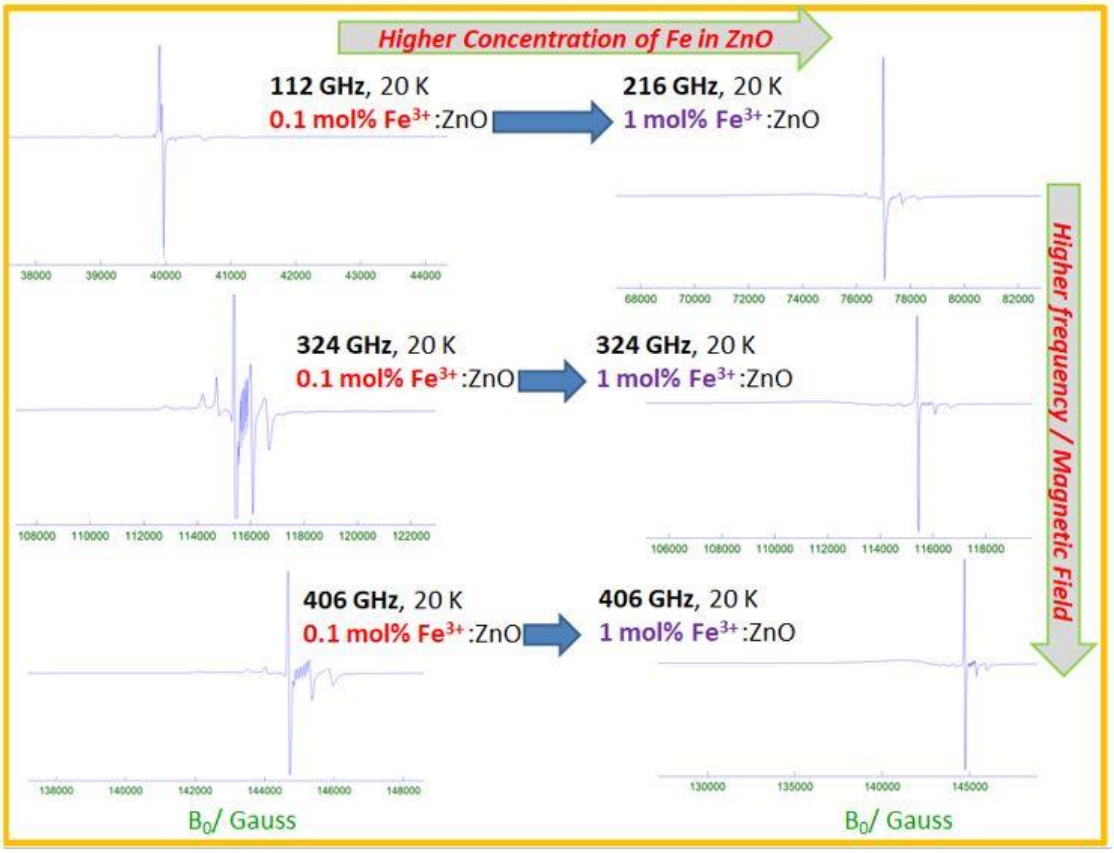

Figure 31 The EPR spectra of ZnO: Fe01-1000 °C and ZnO: Fe1-1000 °C were recorded at 112, 324, and 406 GHz.

4.7.2 EPR Analysis of $Ti_3C_2T_x$ MXene

The first EPR measurement started with the Ti_3AlC_2 MAX phase as in Figure 32. As is known, most MAX phases are Pauli paramagnets; hence, an EPR signal is expected to be observed (Barsoum, 2013).

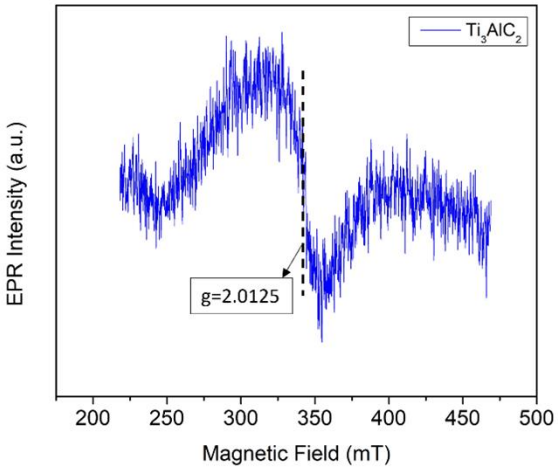

Figure 32 The EPR Spectra of Ti_3AlC_2 MAX phase.

The EPR spectra was measured at room temperature. The applied microwave frequency was 9.64 GHz (X-band), and a power of 1 mW. A total of 10 scans were collected within a sweep time of 467.99 seconds for each cycle. A broad signal is detected at a g-factor of 2.0125, as given in Figure 32. This signal is very close to the g-factor of free electron (g_{free} ~ 2.0023) and very similar to the g-factor of Ti_3AlC_2 that is reported in the literature before (g ~ 2.002) and attributed to the electrons that are trapped in the carbon vacancies, not to the Ti^{3+} defects (Ovodok et al., 2023; Yoon et al., 2018). Since MAX phases are synthesized using ball milling and further calcined at 1400 ºC, extrinsic defects are introduced during synthesis. Thus, by etching the MAX phases, defective Ti_3AlC_2 can be synthesized with respect to the etchant, etching time, and temperature. (Nam et al., 2023). Therefore, within this thesis, different etchant mixtures have been applied to analyze their effects on paramagnetic defect centers and analyze the mechanism of delamination on the paramagnetic defect sites.

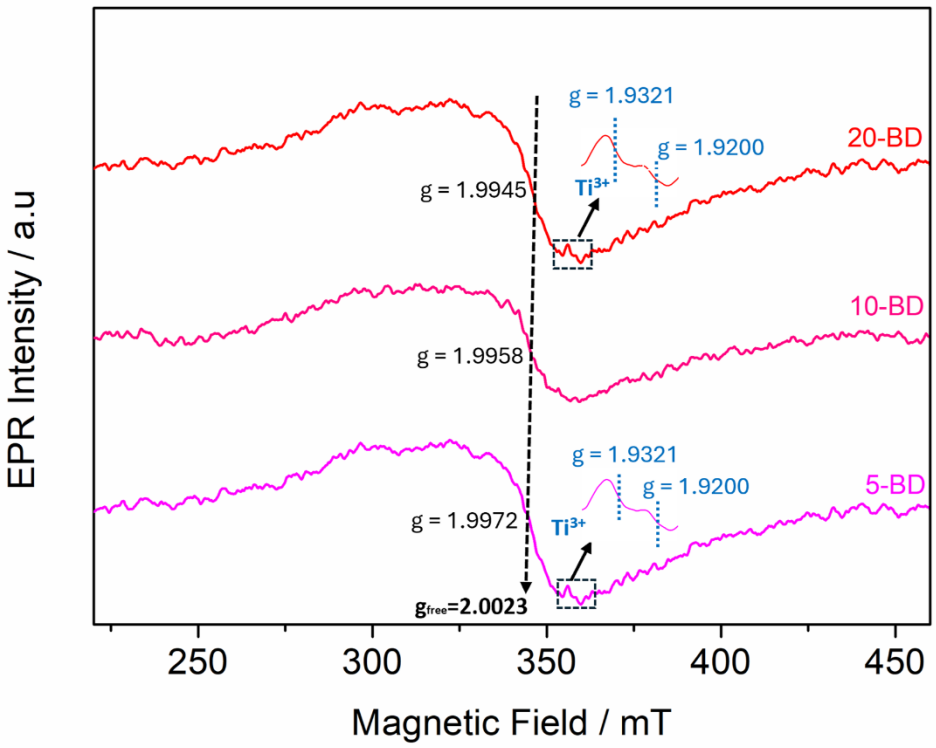

Figure 33 The EPR Spectra of the synthesized $Ti_3C_2T_x$ samples in powder form before delamination (BD) with LiCl.

To clearly understand the changes in the defect structure, we measured the synthesized MXene samples in powder form before delaminating with LiCl. The EPR spectra of the MXene samples before the delamination are given in Figure 33. Unlike the Ti_3AlC_2 MAX phase, here a broad Gaussian signal originating at $g \sim 1.9972$, 1.9958, and 1.9945 has been measured for 5 HF-H_2SO_4, 10 HF-H_2SO_4, and 20 HF-H_2SO_4 samples, respectively, before the delamination. Also, for samples showThis anisotropic signal shows an axial symmetry with two unresolved components ($g_x=g_y<g_z$) (Guskos et al., 2009). This anisotropic signal results from Ti^{3+} defects (Guskos et al., 2009; Sun et al., 2020). Titanium has an electronic configuration that ends with [Ar] $4s^23d^2$. Titanium has three main oxidation states: Ti^{2+}, Ti^{3+}, and Ti^{4+}. Their electronic configurations are $3d^2$, $3d^1$, and $3p^6$, respectively, resulting in spin (S) numbers of 1, ½, and 3, respectively. Ti^{2+} has a spin number of 1, which means that this doublet can split even at zero field; hence, detection using X-band EPR is not possible. In other words, the transitions are forbidden and very weak in EPR. Ti^{3+} has one unpaired electron; thus, it is paramagnetic and detectable using EPR spectroscopy. Ti^{4+} has no unpaired electrons and is therefore diamagnetic and does not exhibit a signal.

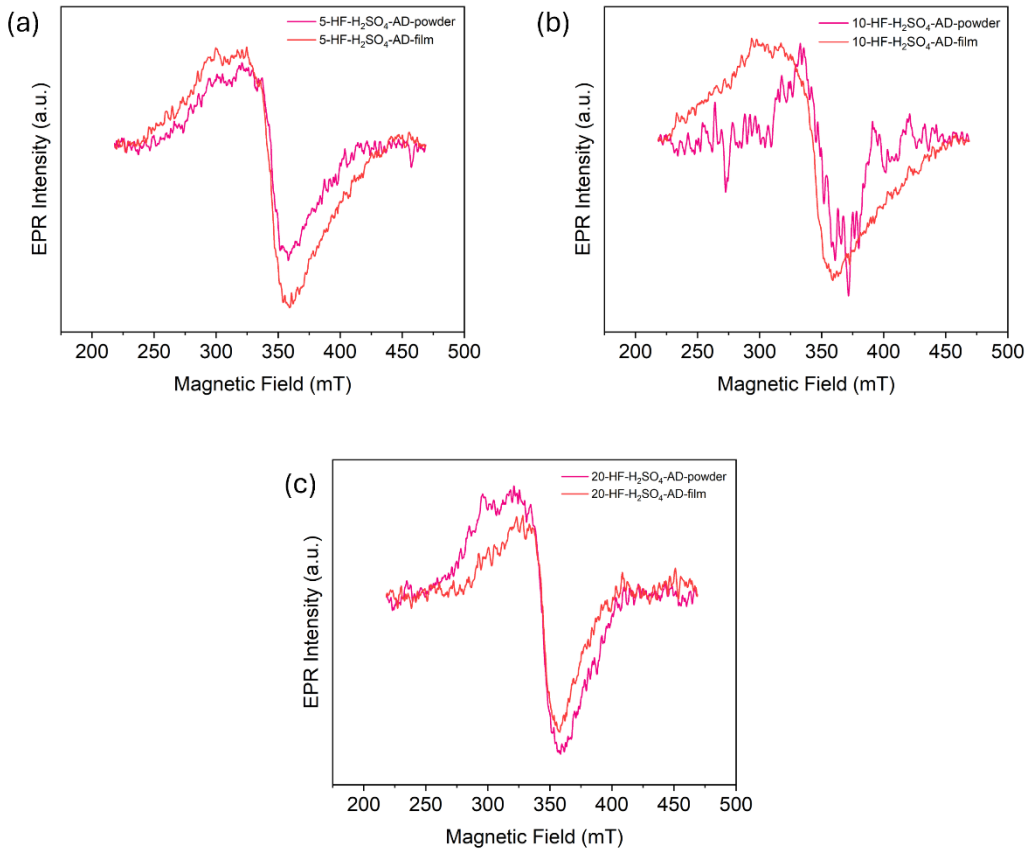

Figure 34 The EPR Spectra of the synthesized $Ti_3C_2T_x$ samples in powder and film form after delaminating with LiCl; (a) 5 HF-H_2SO_4, (b) 10 HF-H_2SO_4, (c) 20 HF-H_2SO_4.

Secondly, we measured the samples after the delamination with LiCl in both powder and film form as in Figure 34. After the delamination, the anisotropic signal present between 350 and 370 mT disappears. This is a significant finding that helps us understand the role of intercalation in the defect structure of MXenes. Moreover, the g-factor of the broad Gaussian signal shifts to the g-factor of the free electron except for sample 10 HF-H_2SO_4. This also illustrates the changes in defect symmetry and the defect environment. The EPR signal measured for the 10 HF-H_2SO_4 powder sample after delamination shows a lower signal-to-noise ratio, but the reason for this is not yet clear.

Table 10 The *g*-factors were measured after delamination with LiCl for samples in both powder and film forms.

Sample Form	**5 HF-H_2SO_4**	**10 HF-H_2SO_4**	**20 HF-H_2SO_4**
Powder	2.0026	1.9939	2.0032
Film	2.0054	2.0054	2.0026

The *g*-factors of the signals given in Figure 34 were reported in Table 10. The calculated g-factors of the samples were very close to $g_{free,}$ and there is no indication of Ti^{3+} defect centers for either form. This demonstrates that delamination effectively leads to changes in the defect structure and environment, regardless of the sample form. Moreover, there are slight shifts in the g-factor, which we attribute to the orientation of the MXene flakes. This implies that EPR spectroscopy can be further utilized to enhance the orientation of MXene flakes and improve the ion pathways in energy storage applications.

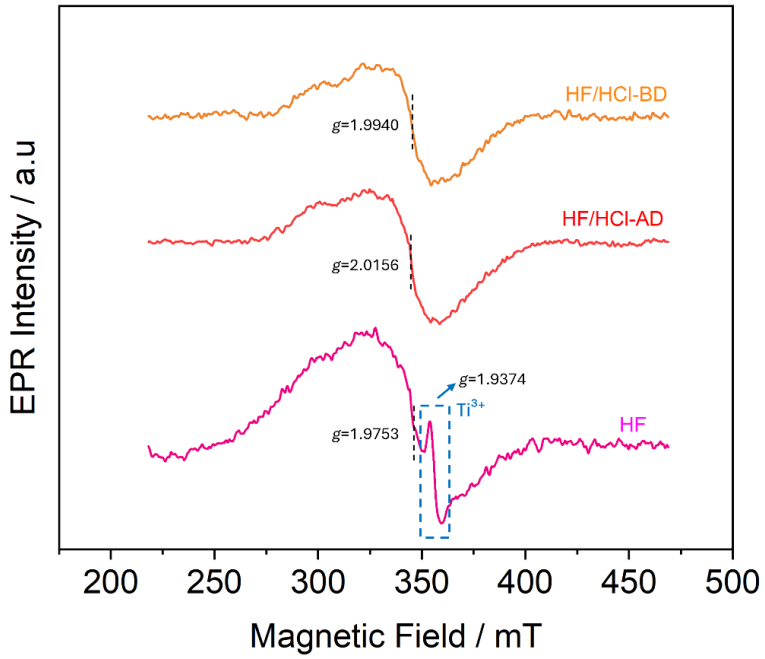

Figure 35 The EPR Spectra of the synthesized $Ti_3C_2T_x$ samples HF and HF/HCl mixture.

Etching in neat HF gives the familiar carbon-derived doublet at $g \approx 2.000$ / 2.006 but also introduces a distinct, sharper line at $g = 1.9374$, attributable to Ti^{3+} centres in a distorted octahedral field—evidence that strong fluoride attack partially reduces surface

Ti. When a 12 mL HF: 8 mL HCl mixture is used instead, only the carbon doublet at g = 2.0004 and 2.006 is observed; the Ti^{3+} resonance disappears, indicating that co-etching with chloride moderates the reaction and suppresses the formation of Ti-related paramagnetic defects as in Figure 35.

4.7.3 EPR Analysis of Activated Carbon

EPR spectroscopy is a powerful technique for probing structural defects in carbon-based materials because of its high sensitivity to paramagnetic imperfections. The X-band EPR spectra of cigarette-butt samples carbonized at 300, 400, 450 and 500 °C display a single symmetric Lorentzian signal at $g \approx 2.00$ which is characteristic of carbon-centred π-electron or dangling-bond radicals and indicating negligible transition-metal impurities. According to Figure 36, as the carbonization temperature rises the signal intensity increase simultaneously from 300 °C to a maximum at 450 °C, then falls at 500 °C, while the linewidth progressively narrows up to 450 °C and remains comparably sharp at 500 °C, implying that between 300 and 450 °C aromatic domains grow and delocalize the spin while creating new edge/defect sites, whereas further heating initiates graphitization that heals some dangling bonds, reducing the total spin population without markedly altering electronic structure.

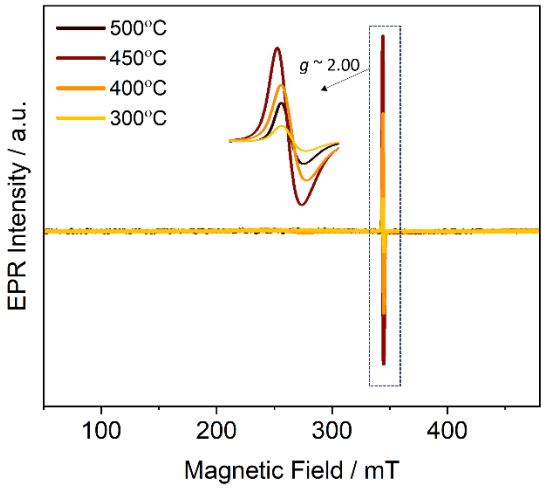

Figure 36 EPR spectra of the cigarette-butts carbonized at 300, 400, 450 and 500 ºC.

Both pristine activated carbon (AC) and KOH-activated AC samples were analyzed by EPR. The results show a pronounced decrease in EPR signal intensity for the KOH-activated sample compared with the untreated one. This suggests that OH groups passivate surface defects, eliminating paramagnetic carbon radicals and thus yielding a less defective structure. The classic "dangling bonds" are also likely reduced after activation. These findings align with Raman spectroscopy: the observed decrease in D-band intensity indicates fewer defects in the carbon framework, corroborating the EPR data. KOH activation also shifts the g-factor from about 2.00 toward 1.99, implying that surface defects are diminished and the remaining defects migrate into the lattice, where orbital effects dominate. Surface defects typically exhibit *g* values near 2.0023, so this shift confirms that surface imperfections are largely eliminated and lattice defects now predominate. Overall, EPR and Raman spectroscopy deliver consistent results, demonstrating that KOH activation plays a key role in defect engineering for activated-carbon materials as in Figure 37.

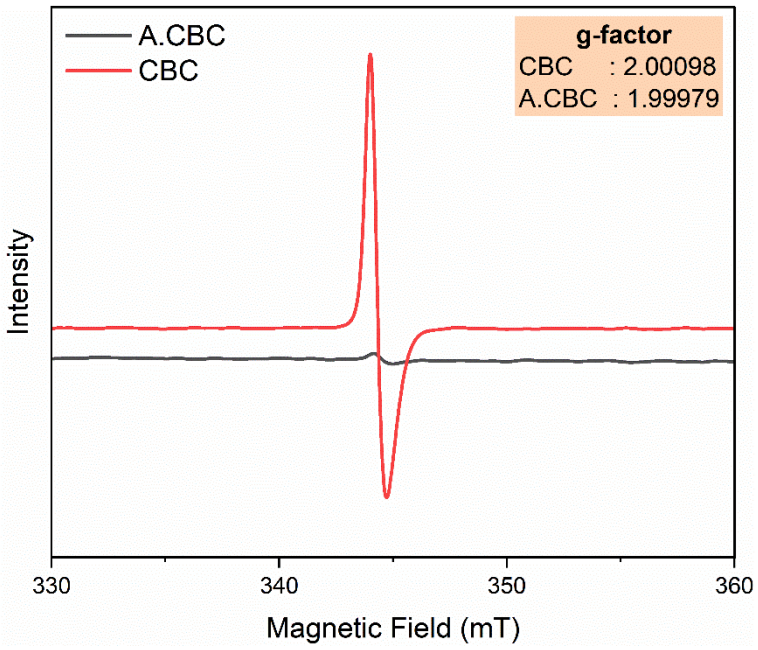

Figure 37 EPR spectra of CBC and A.CBC with their g-factors.

5. ELECTROCHEMICAL ANALYSIS OF ALL-IN-ONE SUPERCAPACITORS

To initiate the electrochemical testing, each assembled cell was first rested for 60 minutes, and the open-circuit potential (OCP) of the cells was checked; all were stable. To stabilize the cell and to remove any impurities in the system each cell has ben pre-cycled with 20 mV/s for 50 cycles. After the precycling finished, CV technique has been applied to the assembled supercapacitors to determine the voltage window.

The specific capacitance of the supercapacitor (Eq. (5.1)) has been calculated using the formula below;

$$C_g = (\int i\, dV) / (m\, v\, \Delta V) \quad (5.1)$$

where C_g is specific capacitance (F/g), ΔV is the potential window (V), m is the total mass of the active material (g), v is the scan rate (mV/s), i is the discharge current (mA).

To calculate the energy and power densities, galvanostatic cycling-potential limitation (GCPL) tests were performed using a constant current density and cycled the supercapacitor to 10,000 cycles. The power and energy density values have been calculated using GCPL results. The gravimetric energy and power density of the supercapacitor as (Eq. (5.2) and (5.3)) has been calculated using the formula below;

$$E_g = 1/2\ (C(\Delta V)^2 / 3.6) \quad (5.2)$$

$$P_g = (E/\Delta t)\ 3600 \quad (5.3)$$

Where E_g is the gravimetric energy density, and P_g is the gravimetric power density (Güngör, 2025).

For the electrode preparation, the same MXene films were used. Fe-doped ZnO samples were synthesized by myself before for my thesis with solid-state reaction. To prepare

the electrodes 80 wt.% Fe-doped ZnO has been mixed with 20 wt.% PTFE and free-standing films were prepared and dried in a vacuum oven at 80 °C for 2 days. The cells were then assembled according to the designs outlined in Table 9.

Table 11 The supercapacitor design showing each component.

Design	**Electrode 1 (E1)**	**Electrode 2 (E2)**	**Electrolyte (EL)**	**Separator**	**Type**
ZnO: Fe005	ZnO: Fe005-1000 °C	ZnO: Fe005-1000 °C	1 M H_2SO_4	Glass-fiber	Symmetric
ZnO: Fe05	ZnO: Fe05-1000 °C	ZnO: Fe05-1000 °C	1 M H_2SO_4	Glass-fiber	Symmetric
ZnO: Fe1	ZnO: Fe1-1000 °C	ZnO: Fe1-1000 °C	1 M H_2SO_4	Glass-fiber	Symmetric
ZnO: Fe1-BM	ZnO: Fe1-1000 °C-BM	ZnO: Fe1-1000 °C-BM	1 M H_2SO_4	Glass-fiber	Symmetric
ZnO: Fe3	ZnO: Fe3-1000 °C	ZnO: Fe3-1000 °C	1 M H_2SO_4	Glass-fiber	Symmetric
AC-KOH	A.CBC	A.CBC	6 M KOH	Glass-fiber	Symmetric
AC-H_2SO_4	A.CBC	A.CBC	1 M H_2SO_4	Glass-fiber	Symmetric
ZnO: Fe005-AC	ZnO: Fe005-1000 °C	A.CBC	1 M H_2SO_4	Glass-fiber	Asymmetric
ZnO: Fe05-AC	ZnO: Fe05-1000 °C	A.CBC	1 M H_2SO_4	Glass-fiber	Asymmetric
ZnO: Fe1-AC	ZnO: Fe1-1000 °C	A.CBC	1 M H_2SO_4	Glass-fiber	Asymmetric
ZnO: Fe1-BM-AC	ZnO: Fe1-1000 °C-BM	A.CBC	1 M H_2SO_4	Glass-fiber	Asymmetric
ZnO: Fe3-AC	ZnO: Fe3-1000 °C	A.CBC	1 M H_2SO_4	Glass-fiber	Asymmetric
ZnO: Fe1-10MXene	ZnO: Fe1-1000 °C	10 HF-H_2SO_4	1 M H_2SO_4	Glass-fiber	Asymmetric
ZnO: Fe1-20MXene	ZnO: Fe1-1000 °C	20 HF-H_2SO_4	1 M H_2SO_4	Glass-fiber	Asymmetric
AC-10 MXene	A.CBC	10 HF-H_2SO_4	1 M H_2SO_4	Glass-fiber	Asymmetric
AC-20 MXene	A.CBC	20 HF-H_2SO_4	1 M H_2SO_4	Glass-fiber	Asymmetric

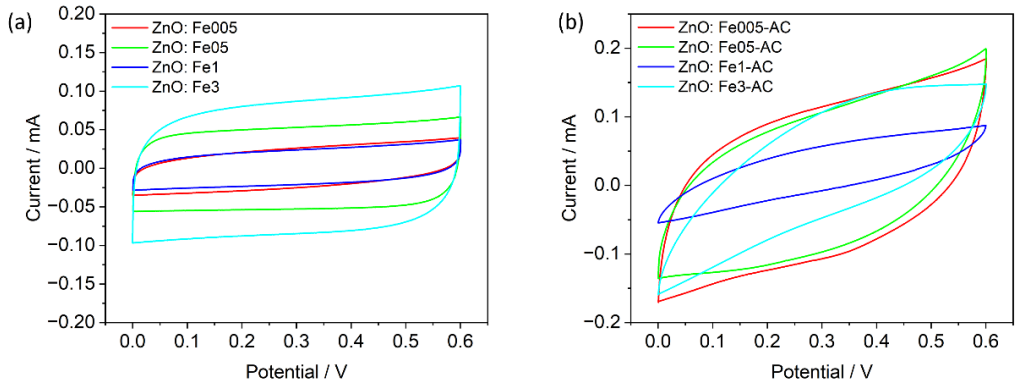

Figure 38 CV graphs of ZnO: Fe005, ZnO: Fe05, ZnO: Fe1, and ZnO: Fe3 recorded at 50 mV/s for 0 to + 0.6 V; (a) symmetric designs, and (b) asymmetric designs using A.CBC.

The electrochemical tests started with symmetric supercapacitors. In Figure 38 (a), the CV results of ZnO: Fe005, ZnO: Fe05, ZnO: Fe1, and ZnO: Fe3 are presented at a scan rate of 50 mV/s within a voltage window of 0.6 V. All four samples show a rectangular CV representing the EDLC behavior without any clear redox peaks (Simon et al., 2014). This allows ions to be quickly and reversibly taken up and released at the electrode surface (Güngör, 2025). In Figure 38 (b), the asymmetric supercapacitors assembled using ZnO: Fe, as opposed to synthesized A.CBC, are given. The shape of the CV changed from rectangular for symmetric designs to a conically tapered shape, or in other words, quasi-rectangular for the asymmetric supercapacitor. Here in Figure 38 (b), the charge-storage mechanism shows both EDLC and pseudocapacitive behavior without any redox peaks. Moreover, to analyze the performance of the supercapacitor at high scan rates, the CV is repeated by varying the scan rates at 2, 5, 10, 20, 50, 100, 200, 500, and 750 mV/s, as shown in Figure 39. In all graphs, as the scan rate increases, the shape of the CV curve remains the same, indicating that there is no impurity in the system and the supercapacitor exhibits stable CV shape at even high-scan rates.

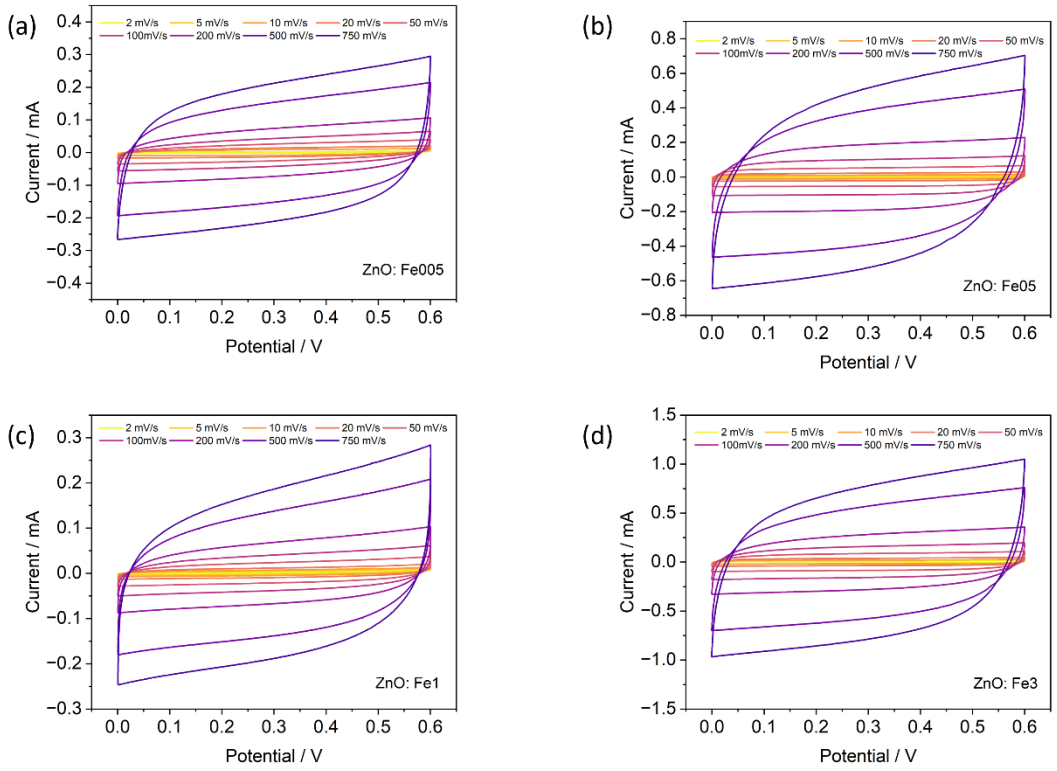

Figure 39 The cyclic voltammograms of the symmetric supercapacitors were recorded at various scan rates: (a) ZnO: Fe005, (b) ZnO: Fe05, (c) ZnO: Fe1, and (d) ZnO: Fe3.

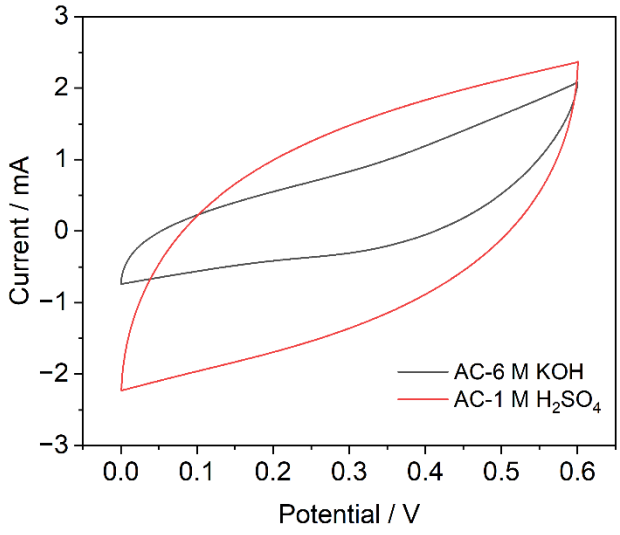

Figure 40 CV of symmetric supercapacitors assembled using 1 M H_2SO_4 and 6 M KOH electrolytes at 50 mV/s using A.CBC electrodes.

To analyze the effect of the electrolyte, two supercapacitors were assembled symmetrically. The only difference is that in one assembly, 6 M KOH is used as the

electrolyte, and in the other, 1 M H_2SO_4 is used. The CV graphs are recorded at 50 mV/s and given in Figure 40. Here, it is seen that with the use of 1 M H_2SO_4, higher current values and comparably higher area can be reached, and hence higher specific capacitances were reached. This can be explained by notably different hydrated ionic sizes: the hydrated proton (H^+) in H_2SO_4 is the smallest at roughly 2.80 Å, whereas the hydrated potassium ion (K^+) in KOH is the largest at about 3.31 Å (Nightingale Jr, 1959).This advantage arises from the proton's exceptionally small ionic and hydrated radii, combined with its high mobility and molar ionic conductivity, which together yield the lowest electrochemical impedance and the most pronounced capacitive response in the H_2SO_4 electrolyte system (Ibukun & Jeong, 2019). Thus, 1 M H_2SO_4 is used for assembling supercapacitors.

To further analyze the effect of reducing the particle size via high-energy ball milling and changing the extrinsic defect structure, a set of supercapacitors, both symmetric and asymmetric, was assembled. Their CV graph is given in Figure 41. Here, it is seen that when the ZnO: Fe1-BM sample is used as an electrode material, the area under the CV curve increases. This can be explained as bulk (larger particle sizes) ZnO shows EDLC behavior whereas at the nanoscale, its plentiful surface defects induce pseudocapacitive behavior, with Faradaic reactions becoming the dominant charge-storage mechanism (Toufani et al., 2020). The ZnO: Fe1-BM-AC supercapacitors' CV shape exhibits pseudocapacitive behavior with clear redox peaks, indicating that the device's specific capacitance and energy density are enhanced, resulting in battery-like performance. Hence, such systems are often dubbed "superbats" (battery-like supercapacitors) (Kasap, Kaya, Repp, & Erdem, 2019).

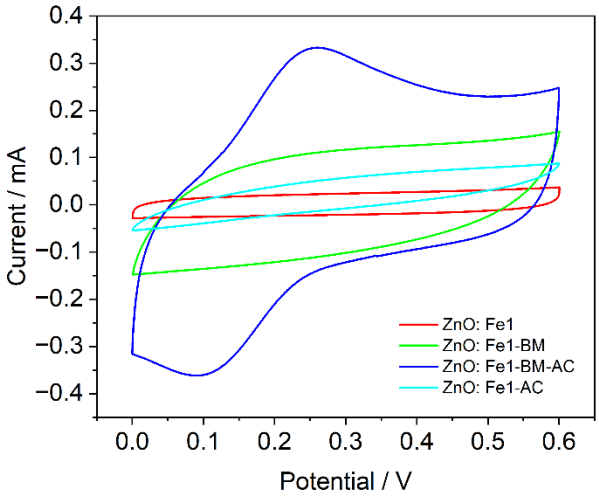

Figure 41 CV of ZnO: Fe1, ZnO: Fe1-BM symmetric, and ZnO: Fe1-BM-AC, and ZnO: Fe1-AC asymmetric supercapacitors assembled using 1 M H_2SO_4 at 50 mV/s.

The synergy between the MXene versus ZnO:Fe and A.CBC was investigated. The quasi-rectangular, conical shape of the ZnO: Fe1 curves reflects a combination of EDLC and surface-confined Faradaic processes, indicating good reversibility. For all designs given in Fig.42 no redox peaks were observed.

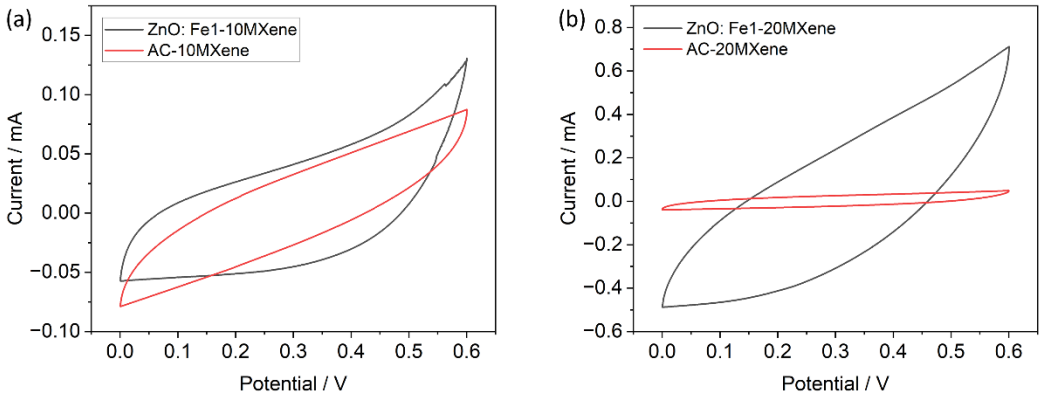

Figure 42 The cyclic voltammograms of the asymmetric supercapacitors were recorded at 50 mV/s ; (a) ZnO: Fe1-10MXene and AC-10MXene, and (b) ZnO: Fe1-20MXene and AC-20MXene.

To evaluate high-rate performance, CV measurements were carried out at scan rates of 2, 5, 10, 20, 50, 100, 200, 500, and 750 mV/s (Figure 43). The voltammograms

maintained their shape as the scan rate increased, indicating stable behavior even at very high scan rates.

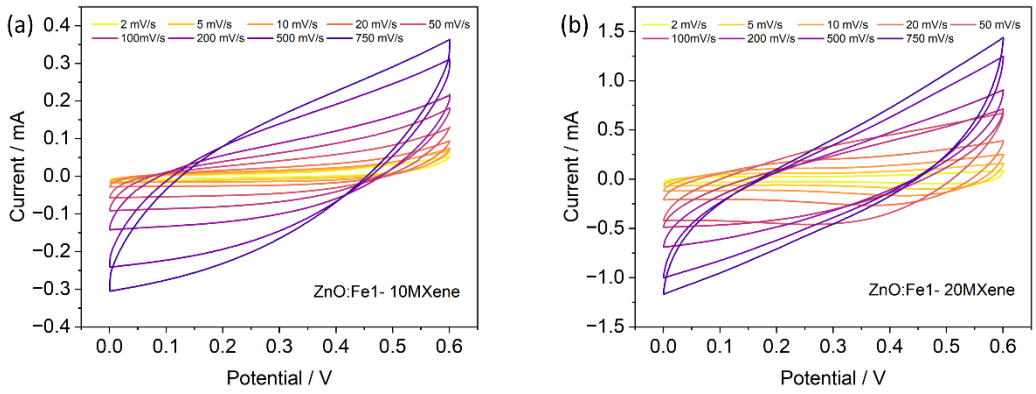

Figure 43 The cyclic voltammograms of the asymmetric supercapacitors were recorded at various scan rates; (a) ZnO: Fe1-10MXene, and (b) ZnO: Fe1-20MXene.

The Nyquist plots in Figure 44 (a)–(d) collectively show how electrode composition and processing influence both series resistance (R_s) and ion-diffusion behavior. No semicircles were observed in any of the plots. The lack of any semicircular arc at high frequencies across all plots suggests rapid ion diffusion and virtually no interfacial charge-transfer resistance at the electrodes.

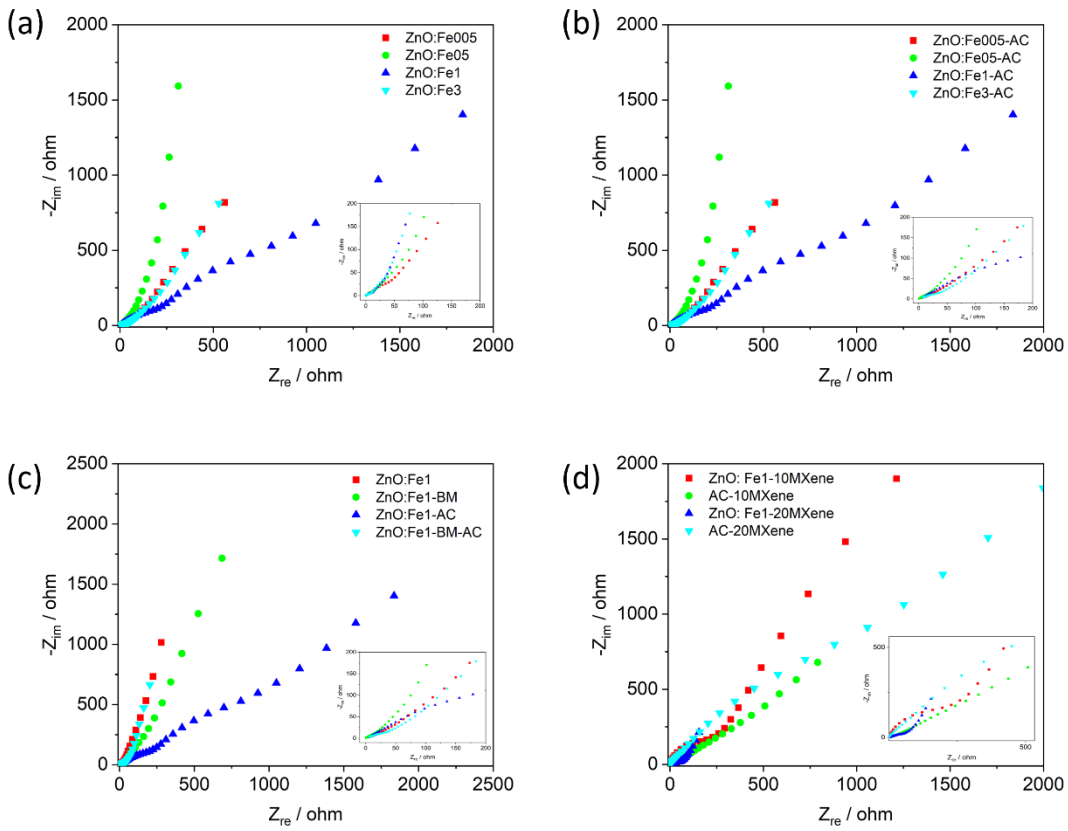

Figure 44 Nyquist plots of supercapacitor assemblies: (a) Symmetric supercapacitors composed of ZnO: Fe, (b) Asymmetric designs using ZnO: Fe opposed to A.CBC, (c) ZnO: Fe1 and ZnO: Fe1-BM sample opposed to A.CBC, (d) Asymmetric designs using ZnO: Fe, MXene and A.CBC.

GCPL measurements of all supercapacitors were held at 1 A/g current density within a voltage range of 0 to + 0.6 V for 10,000 Cycles. The specific capacity versus potential graphs of the supercapacitors designed by using ZnO: Fe and A.CBC were analyzed in Figure 45 below. In Figure 45 (a), the specific capacity vs potential graph of symmetric supercapacitors assembled using ZnO: Fe at different dopant concentrations is given. It is seen that the highest capacity was obtained from ZnO: Fe3, followed by ZnO: Fe05. This result is in agreement with the CV graphs, which show the highest current values and area, implying a higher specific capacitance. Upon further analysis of Figure 46 (a), it is evident that the ball-milled sample with 1 mol% achieves the highest specific capacity among all supercapacitors. As we discussed earlier, as the calcination temperature increases, the particles agglomerate and the particle size increases. As in line with the literature, the particle size influences the electrochemical performance (Ammar, Yildirim, Bakan, & Erdem, 2021; Erdem, 2014). Here, using ball milling, as

seen in the CV results, the charge-storage behavior changes, and dominant redox peaks are observed. Here, the GCPL results confirm the CV results as well, showing that reducing the particle size improves the electrochemical performance. As shown in Figure 46 (a), using the ball-milled sample yields better performance compared to ZnO: Fe1, with a specific capacity of 62 mAh/g at a current density of 1 A/g.

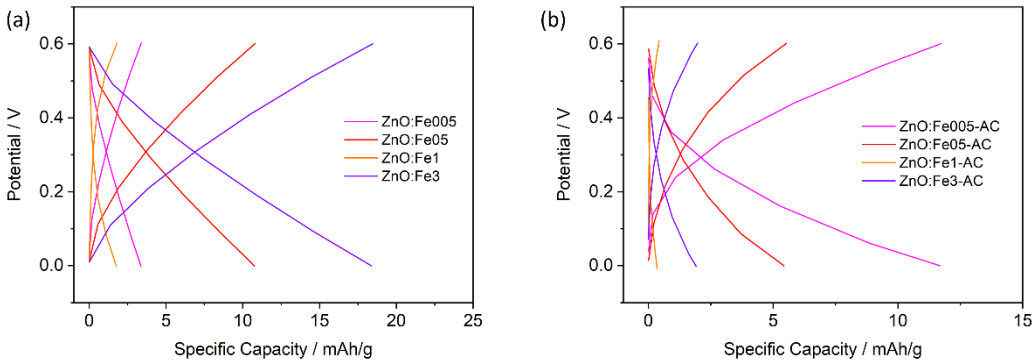

Figure 45 Specific capacitance versus potential graph of supercapacitor designs: (a) Symmetric designs using Fe-doped ZnO, (b) Asymmetric designs using Fe-doped ZnO opposed CB.

In Figure 46 (b), the highest capacitance is measured from ZnO:Fe1-20MXene (as 19 mAh/g at 1 A/g). Both CV and GCPL results confirm that 20-MXene shows better electrochemical performance compared to 10-MXene.

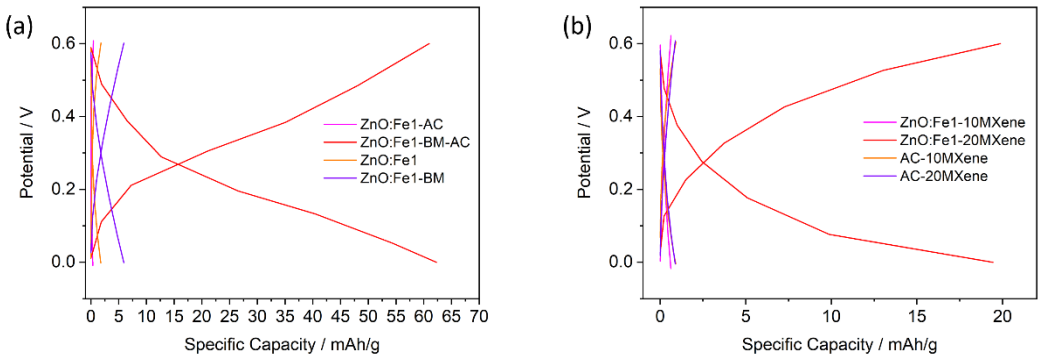

Figure 46 Specific capacitance versus potential graph of supercapacitor designs: (a) ZnO: Fe1 and ZnO: Fe1-BM samples opposed to A.CBC, and (b) Asymmetric designs using ZnO:Fe, MXene, and A.CBC.

The Coulombic efficiency (CE) has been calculated using the GCPL analysis and is given in Figure 47 below. Firstly, in Figure 47 (a), four symmetric supercapacitors, ZnO: Fe-005, ZnO: Fe-05, ZnO: Fe-1, and ZnO: Fe-3, were analyzed. The stability of the ZnO: Fe-1 saturated most and shows unstable performance. However, the CE values of all supercapacitors were higher than 98 % for 10,000 cycles. For the asymmetric supercapacitors assembled using ZnO: Fe versus A.CBC, shown in Figure 47 (b), lower CE values were obtained compared to the symmetric cells. This is in agreement with the CV results, that the electrochemical performance degrades when Fe-doped ZnO samples are used asymmetrically with A.CBC. Here, the ZnO: Fe1-CB also showed the lowest CE value, around 80 %. However, when the ball-milled sample is used as an electrode, the CE increases, as shown in Figure 47 (c), which results from the reduced particle size, as discussed earlier. Finally, in Figure 47 (d), the CE of asymmetric supercapacitors was given. Herein, the performance of the ZnO: Fe1-20MXene showed lower CE values, which are controversial compared to CV results; however, the CE values are still higher than 97 %.

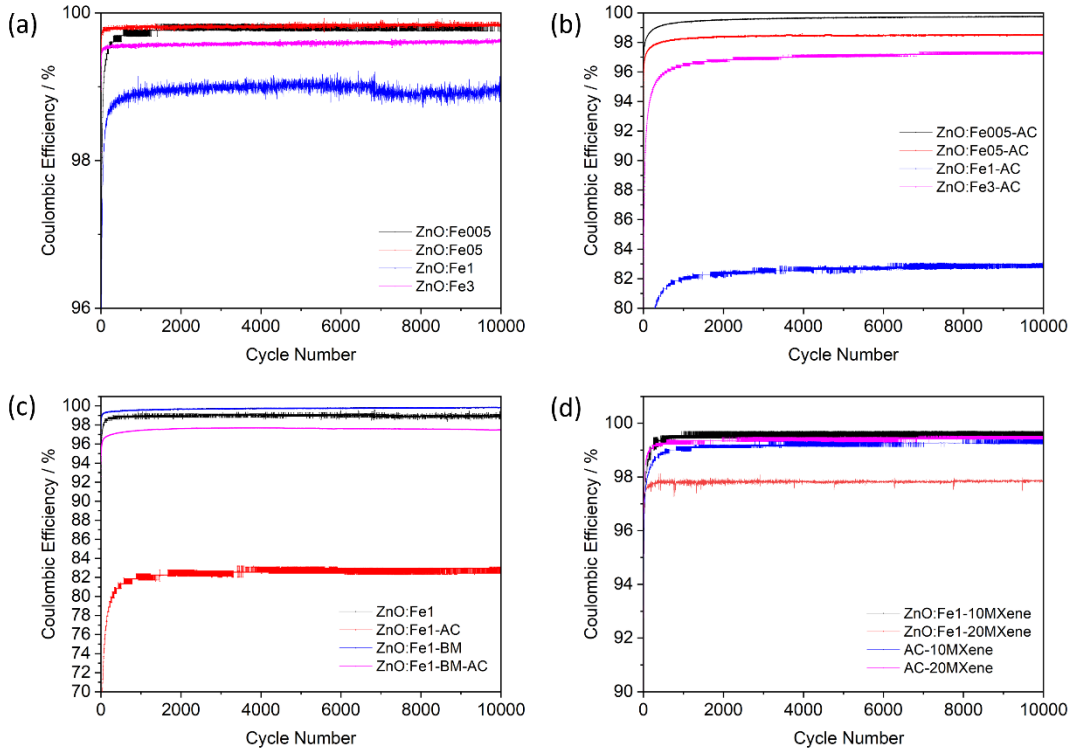

Figure 47 The Coulombic efficiency graphs of supercapacitor designs: (a) Symmetric designs using ZnO-Fe, (b) Asymmetric designs using ZnO:Fe opposed to A.CBC, (c) ZnO: Fe1 and ZnO: Fe1-BM sample opposed to A.CBC, (d) Asymmetric designs using ZnO:Fe, MXene, and A.CBC.

The specific capacitance, energy, and power densities were calculated using Eq. (5.1), (5.2), and (5.3) and GCPL data recorded at 1 A/g and tabulated in Table 12. The ZnO: Fe1-BM-AC achieves the maximum values across all metrics, delivering a specific capacitance of 416 F/g, an energy density of 74 Wh/kg, and a power density of 1,123 W/kg, higher than any other design tested at 1 A/g. This can be attributed to the effect of ball milling, as ZnO: Fe1 outperforms ZnO: Fe1-BM. Among the symmetric supercapacitors, IDY-3 showed the highest performance for C_s, E_g, and P_g (323 F/g, 58 Wh/kg, and 1,049 W/kg, respectively). This is quite expected due to the higher concentration of Fe^{3+} doping. Moreover, for asymmetric supercapacitors, ZnO: Fe1-20MXene showed the highest performance.

Table 12 The calculated specific capacitance, energy, and power density values using GCPL analysis were recorded at a current density of 1 A/g.

Design Name	Specific Capacitance (F/g)	Energy Density (Wh/kg)	Power Density (W/kg)
ZnO: Fe005	58	10	158
ZnO: Fe05	77	13	207
ZnO: Fe1	39	7.	32
ZnO: Fe1-BM	166	15	68
ZnO: Fe3	323	58	1049
ZnO: Fe005-AC	82	15	40
ZnO: Fe05-AC	77	13	37
ZnO: Fe1-AC	83	14	224
ZnO: Fe1-BM-AC	416	74	1123
ZnO: Fe3-AC	83	14	68
ZnO: Fe1-10MXene	39	7	18
ZnO: Fe1-20MXene	222	40	182
AC-10 MXene	77	14	36
AC-20 MXene	22	4	10

6. CONCLUSIONS AND FUTURE WORK

In this work, we have synthesized three distinct electrode materials—Fe-doped ZnO nanoparticles, $Ti_3C_2T_x$ MXene, and activated carbons, to produce materials that would provide high energy and power densities to improve the electrochemical performance of supercapacitors. Firstly, a solid-state reaction method is used to synthesize Fe-doped ZnO by focusing on the effect of calcination temperature, as well as dopant concentration to tailor the defects via EPR. Secondly, $Ti_3C_2T_x$ MXene were obtained by selectively etching Al from Ti_3AlC_2 using either concentrated HF, HF/HCl and HF/H_2SO_4 mixture, followed by with LiCl. Finally, waste cigarette butts were transformed into hierarchically porous carbons through inert-atmosphere carbonization, then chemically activated using different chemical agents. High surface area and pore volume is achieved using KOH as chemical agent.

For $Ti_3C_2T_x$ MXene, X-band EPR of films etched in neat HF exhibited a carbon-derived doublet ($g \approx 2.000/2.006$) alongside a sharp Ti^{3+} resonance at $g = 1.9374$. In contrast, a HF/HCl mixture suppressed Ti^{3+} centers entirely, confirming that co-etching controls surface-reduction pathways. In cigarette-butt carbons, spin population peaked for samples carbonized at 450 °C reflected by the maximum Lorentzian EPR intensity and declined at 500 °C as graphitization healed dangling bonds; KOH activation then halved the EPR signal and shifted the g-factor from ~2.0023 to ~1.99, demonstrating surface-defect passivation and migration of residual defects into the lattice. Our waste-to-wealth strategy—transforming discarded cigarette butts into high-performance carbons—underscores the sustainability potential of circular economy approaches in energy storage. The specific capacitance, energy density, and power density values were derived from GCPL measurements at 1 A/g. Among all samples, ZnO: Fe1-BM-AC exhibits the highest performance, reaching 416 F/g, 74 Wh/kg, and 1123 W/kg, surpassing every other design tested under the same conditions. This improvement is

attributable to the ball-milling process, as evidenced by the superior results of ZnO: Fe1-BM compared to the unmodified ZnO: Fe1. In the symmetric supercapacitors, ZnO: Fe3 delivered the best results (323 F/g, 58 Wh/kg, 1 049 W/kg), which aligns with its higher Fe^{3+} doping level. For the asymmetric configurations, the ZnO: Fe1-20MXene variant achieved the top performance metrics. However, the overall performance of MXenes, in contrast to ZnO:Fe and AC, was very low. However, there is still potential for the application of these materials as supercapacitor electrodes. This unified study not only advances fundamental understanding of defect-mediated charge storage but also shows the potential of sustainable, waste-to-wealth electrode materials for next-generation high-capacitance energy storage.

BIBLIOGRAPHY

Açıkgöz, M., Drahus, M. D., Ozarowski, A., Van Tol, J., Weber, S., & Erdem, E. (2014). Local coordination of Fe3+ in ZnO nanoparticles: multi-frequency electron paramagnetic resonance (EPR) and Newman superposition model analysis. *Journal of Physics: Condensed Matter, 26*(15), 155803.

Aksel, E., Erdem, E., Jakes, P., Jones, J. L., & Eichel, R.-A. (2010). Defect structure and materials “hardening” in Fe2O3-doped [Bi0. 5Na0. 5] TiO3 ferroelectrics. *Applied Physics Letters, 97*(1).

Al-Enizi, A. M. (2022). Waste cigarette butt-derived B, N doped bifunctional hierarchical mesoporous carbon for supercapacitor and oxygen reduction reaction. *Colloids and Surfaces A: Physicochemical and Engineering Aspects, 643*, 128775.

Aleinawi, M. H., Ammar, A. U., Şentürk, D., Barbu-Tudoran, L., Ajala, O. J., Eşkin, D., . . . Erdem, E. (2025). Microwave-tuned Mn-doped ZnO for all-in-one supercapacitors: Correlating defect chemistry with electrochemical behavior. *Journal of Colloid and Interface Science*, 138012.

Alhabeb, M., Maleski, K., Anasori, B., Lelyukh, P., Clark, L., Sin, S., & Gogotsi, Y. (2017). Guidelines for synthesis and processing of two-dimensional titanium carbide (Ti3C2T x MXene). *Chemistry of Materials, 29*(18), 7633-7644.

Altaf, C. T., Colak, T. O., Erdem, E., Unal, U., Misirlioglu, F. B., Condorelli, G. G., . . . Sankir, M. (2023). Disulfonated polyarylene ether sulfone membrane for graphitic carbon nitride/zinc oxide based photo-supercapacitors. *Electrochimica Acta, 456*, 142415.

Alvi, N., Ul Hasan, K., Nur, O., & Willander, M. (2011). The origin of the red emission in n-ZnO nanotubes/p-GaN white light emitting diodes. *Nanoscale research letters, 6*(1), 130.

Ammar, A. U., Yildirim, I. D., Bakan, F., & Erdem, E. (2021). ZnO and MXenes as electrode materials for supercapacitor devices. *Beilstein Journal of Nanotechnology, 12*(1), 49-57.

An, Y., Tian, Y., Feng, J., & Qian, Y. (2022). MXenes for advanced separator in rechargeable batteries. *Materials Today, 57*, 146-179.

Anasori, B., Lukatskaya, M. R., & Gogotsi, Y. (2017). 2D metal carbides and nitrides (MXenes) for energy storage. *Nature Reviews Materials, 2*(2), 1-17.

Anasori, B., Lukatskaya, M. R., & Gogotsi, Y. (2023). 2D metal carbides and nitrides (MXenes) for energy storage. In *MXenes* (pp. 677-722): Jenny Stanford Publishing.

Anayee, M., Kurra, N., Alhabeb, M., Seredych, M., Hedhili, M. N., Emwas, A.-H., . . . Gogotsi, Y. (2020). Role of acid mixtures etching on the surface chemistry and sodium ion storage in Ti 3 C 2 T x MXene. *Chemical Communications, 56*(45), 6090-6093.

Azamat, D., & Fanciulli, M. (2007). The structure of charge-compensated Fe3+ ions in ZnO. *Physica B: Condensed Matter, 401*, 382-385.

Bai, S., Guo, T., Zhao, Y., Sun, J., Li, D., Chen, A., & Liu, C. C. (2014). Sensing performance and mechanism of Fe-doped ZnO microflowers. *Sensors and Actuators B: Chemical, 195*, 657-666.

Baraki, R., Zierep, P., Erdem, E., Weber, S., & Granzow, T. (2014). Electron paramagnetic resonance study of ZnO varistor material. *Journal of Physics: Condensed Matter, 26*(11), 115801.

Barsoum, M. W. (2013). *MAX phases: properties of machinable ternary carbides and nitrides*: John Wiley & Sons.

Blankenship, L. S., & Mokaya, R. (2017). Cigarette butt-derived carbons have ultra-high surface area and unprecedented hydrogen storage capacity. *Energy & Environmental Science, 10*(12), 2552-2562.

Brunauer, S., Emmett, P. H., & Teller, E. (1938). Adsorption of gases in multimolecular layers. *Journal of the American chemical society, 60*(2), 309-319.

Cabrera-Baez, M., Padrón-Hernández, E., Soares, J. M., Santos, F., Guerra, Y., & Peña-Garcia, R. (2021). Effect of yttrium substitution in Fe-doped ZnO nanoparticles: An EPR study. *Journal of Magnetism and Magnetic Materials, 538*, 168317.

Caturla, F., Molina-Sabio, M., & Rodriguez-Reinoso, F. (1991). Preparation of activated carbon by chemical activation with ZnCl2. *Carbon, 29*(7), 999-1007.

Chakraborty, I., Shirodkar, S. N., Gohil, S., Waghmare, U. V., & Ayyub, P. (2013). A stable, quasi-2D modification of silver: optical, electronic, vibrational and mechanical properties, and first principles calculations. *Journal of Physics: Condensed Matter, 26*(2), 025402.

Cheng, Y., Zhang, Q., Fang, C., Huang, Z., Chen, J., Wu, L., & Wang, H. (2019). Synthesis of N-doped porous carbon materials derived from waste cellulose acetate fiber via urea activation and its potential application in supercapacitors. *Journal of the Electrochemical Society, 166*(6), A1231.

Colak, T. O., Altaf, C. T., Yesilbag, F. N. T., Yesilbag, Y. O., Yildirim, I. D., Erdem, E., . . . Sankir, M. (2024). Photo-supercapacitors based on zinc oxide/MXene paper dual acting electrodes. *Journal of Energy Storage, 86*, 111274.

D'Ambrosio, S., Chen, L., Nakayama, H., Matsukura, F., Dietl, T., & Ohno, H. (2015). Ferromagnetic resonance of Py deposited on ZnO grown by molecular beam epitaxy. *Japanese Journal of Applied Physics, 54*(9), 093001.

Debernardi, A., & Fanciulli, M. (2007). The magnetic interaction of Fe doped ZnO with intrinsic defects: a first principles study. *Physica B: Condensed Matter, 401*, 451-453.

Downes, M., Shuck, C. E., McBride, B., Busa, J., & Gogotsi, Y. (2024). Comprehensive synthesis of Ti3C2T x from MAX phase to MXene. *Nature protocols, 19*(6), 1807-1834.

Duan, X., Srinivasakannan, C., Wang, X., Wang, F., & Liu, X. (2017). Synthesis of activated carbon fibers from cotton by microwave induced H3PO4 activation. *Journal of the Taiwan Institute of Chemical Engineers, 70*, 374-381.

Emmett, P. H., & Brunauer, S. (1937). The use of low temperature van der Waals adsorption isotherms in determining the surface area of iron synthetic ammonia catalysts. *Journal of the American chemical society, 59*(8), 1553-1564.

Erdem, E. (2014). Microwave power, temperature, atmospheric and light dependence of intrinsic defects in ZnO nanoparticles: A study of electron paramagnetic resonance (EPR) spectroscopy. *Journal of alloys and compounds, 605*, 34-44.

Genc, R., Alas, M. O., Harputlu, E., Repp, S., Kremer, N., Castellano, M., . . . Erdem, E. (2017). High-capacitance hybrid supercapacitor based on multi-colored fluorescent carbon-dots. *Scientific reports, 7*(1), 11222.

Gurylev, V., & Perng, T. P. (2021). Defect engineering of ZnO: Review on oxygen and zinc vacancies. *Journal of the European Ceramic Society, 41*(10), 4977-4996.

Guskos, N., Typek, J., Bodziony, T., Zolnierkiewicz, G., Maryniak, M., & Biedunkiewicz, A. (2009). Ageing effect in nanocrystalline TiCx/C studied by EPR. *Journal of alloys and compounds, 470*(1-2), 51-54.

Güngör, A. (2025). Enhanced supercapacitor performance with cerium-doped polypyrrole nanofibers. *Journal of Materials Chemistry A, 13*(24), 18641-18655.

Haynes, S., Wilson, S., & Strickler, D. (1991). Study of the environmental degradation of cigarette filters: a simulation of the roadside or parking lot environment. Eastman Chemical custode service technical report. In.

Heidarinejad, Z., Dehghani, M. H., Heidari, M., Javedan, G., Ali, I., & Sillanpää, M. (2020). Methods for preparation and activation of activated carbon: a review. *Environmental Chemistry Letters, 18*(2), 393-415.

Heitz, R., Hoffmann, A., & Broser, I. (1992). Fe 3+ center in ZnO. *Physical Review B, 45*(16), 8977.

Hu, C., Hu, S., Fang, P., Tang, Z., Xiao, X., & Wu, H. (2022). Waste-Tire-Derived Activated Carbon as Efficient Adsorbent of P-Nitrophenol from Wastewater. *Journal of Chemistry, 2022*(1), 7313899.

Huang, X., Zhang, C., Tay, C., Venkatesan, T., & Chua, S. (2013). Green luminescence from Cu-doped ZnO nanorods: Role of Zn vacancies and negative thermal quenching. *Applied Physics Letters, 102*(11).

Huang, Y., Liu, Z., & Zhao, G. (2016). Reaction process for ZnCl 2 activation of phenol liquefied wood fibers. *RSC Advances, 6*(82), 78909-78917.

Ibukun, O., & Jeong, H. K. (2019). Effects of aqueous electrolytes in supercapacitors. *새물리, 69*(2), 154-158.

Igelmund, A., & Hausmann, A. (1975). Forbidden ESR transitions ΔS=±2 of Fe3+ and Mn2+ in zinc oxide. *Zeitschrift für Physik B Condensed Matter, 21*(1), 65-67.

Janotti, A., & Van de Walle, C. G. (2009). Fundamentals of zinc oxide as a semiconductor. *Reports on progress in physics, 72*(12), 126501.

Jibril, B., Houache, O., Al-Maamari, R., & Al-Rashidi, B. (2008). Effects of H3PO4 and KOH in carbonization of lignocellulosic material. *Journal of Analytical and applied pyrolysis, 83*(2), 151-156.

Kaftelen, H., Ocakoglu, K., Thomann, R., Tu, S., Weber, S., & Erdem, E. (2012). EPR and photoluminescence spectroscopy studies on the defect structure of ZnO nanocrystals. *Physical Review B—Condensed Matter and Materials Physics, 86*(1), 014113.

Karmakar, D., Mandal, S., Kadam, R., Paulose, P., Rajarajan, A., Nath, T. K., . . . Das, G. (2007). Ferromagnetism in Fe-doped ZnO nanocrystals: experiment and theory. *Physical Review B—Condensed Matter and Materials Physics, 75*(14), 144404.

Kasap, S., Kaya, I. I., Repp, S., & Erdem, E. (2019). Superbat: battery-like supercapacitor utilized by graphene foam and zinc oxide (ZnO) electrodes induced by structural defects. *Nanoscale Advances, 1*(7), 2586-2597.

Kumar, A., Dutta, S., Kim, S., Kwon, T., Patil, S. S., Kumari, N., . . . Lee, I. S. (2022). Solid-state reaction synthesis of nanoscale materials: strategies and applications. *Chemical Reviews, 122*(15), 12748-12863.

Kumar, S., Asokan, K., Singh, R. K., Chatterjee, S., Kanjilal, D., & Ghosh, A. K. (2014). Investigations on structural and optical properties of ZnO and ZnO: Co nanoparticles under dense electronic excitations. *RSC Advances, 4*(107), 62123-62131.

Langmuir, I. (1916). The constitution and fundamental properties of solids and liquids. Part I. Solids. *Journal of the American chemical society, 38*(11), 2221-2295.

Langmuir, I. (1918). The adsorption of gases on plane surfaces of glass, mica and platinum. *Journal of the American chemical society, 40*(9), 1361-1403.

László, K., Bóta, A., & Nagy, L. G. (2000). Comparative adsorption study on carbons from polymer precursors. *Carbon, 38*(14), 1965-1976.

Li, J., Liu, J., Li, C., Luo, J., Shen, C., & Yang, J. (2023). Preparation of discarded cigarette butt-derived activated carbon and its decolorization for waste edible oils. *Biomass Conversion and Biorefinery, 13*(11), 10299-10309.

Liang, J., Li, C., Zhang, S., Wang, S., & Hu, X. (2024). Sequential activation of willow wood with ZnCl2 and H3PO4 drastically impacts pore structure of activated carbon. *Industrial Crops and Products, 221*, 119387.

Lillo-Ródenas, M., Cazorla-Amorós, D., & Linares-Solano, A. (2003). Understanding chemical reactions between carbons and NaOH and KOH: an insight into the chemical activation mechanism. *Carbon, 41*(2), 267-275.

Liu, X., Huang, S., Li, G., Zhang, Q., Zhang, H., Yang, Y., . . . Huang, J. (2024). *Preparation and application of waste cigarette butts-derived mulch film with excellent mechanical properties and optical transparency.* Paper presented at the Journal of Physics: Conference Series.

Luke, J. (1991). *Degradability of Filter Materials and Plastics Packaging.* Paper presented at the BATCo meeting Impacts of Environmental Regulations on Packing and Product. British American Tobacco.

Maciá-Agulló, J., Moore, B., Cazorla-Amorós, D., & Linares-Solano, A. (2004). Activation of coal tar pitch carbon fibres: Physical activation vs. chemical activation. *Carbon, 42*(7), 1367-1370.

Mahto, A., Halakarni, M. A., Maraddi, A., D'Souza, G., Samage, A. A., Thummar, U. G., . . . Nataraj, S. (2022). Upcycling cellulose acetate from discarded cigarette butts: Conversion of contaminated microfibers into loose-nanofiltration membranes for selective separation. *Desalination, 535*, 115807.

Malguth, E., Hoffmann, A., & Phillips, M. R. (2008). Fe in III–V and II–VI semiconductors. *physica status solidi (b), 245*(3), 455-480.

Marinello, S., Lolli, F., Gamberini, R., & Rimini, B. (2020). A second life for cigarette butts? A review of recycling solutions. *Journal of hazardous materials, 384*, 121245.

Meng, Q., Chen, W., Wu, L., Lei, J., Liu, X., Zhu, W., & Duan, T. (2019). A strategy of making waste profitable: Nitrogen doped cigarette butt derived carbon for high performance supercapacitors. *Energy, 189*, 116241.

Merlen, A., Buijnsters, J. G., & Pardanaud, C. (2017). A guide to and review of the use of multiwavelength Raman spectroscopy for characterizing defective aromatic carbon solids: From graphene to amorphous carbons. *Coatings, 7*(10), 153.

Naguib, M., Kurtoglu, M., Presser, V., Lu, J., Niu, J., Heon, M., . . . Barsoum, M. W. (2011). Two-dimensional nanocrystals produced by exfoliation of Ti3AlC2. In *MXenes* (pp. 15-29): Jenny Stanford Publishing.

Naguib, M., Kurtoglu, M., Presser, V., Lu, J., Niu, J., Heon, M., . . . Barsoum, M. W. (2023). Two-dimensional nanocrystals produced by exfoliation of Ti3AlC2. In *MXenes* (pp. 15-29): Jenny Stanford Publishing.

Naguib, M., Mashtalir, O., Carle, J., Presser, V., Lu, J., Hultman, L., . . . Barsoum, M. W. (2012). Two-dimensional transition metal carbides. *ACS nano, 6*(2), 1322-1331.

Najib, S., & Erdem, E. (2019). Current progress achieved in novel materials for supercapacitor electrodes: mini review. *Nanoscale Advances, 1*(8), 2817-2827.

Nam, S., Mahato, M., Matthews, K., Lord, R. W., Lee, Y., Thangasamy, P., . . . Oh, I. K. (2023). Bimetal Organic framework–Ti3C2Tx MXene with metalloporphyrin electrocatalyst for lithium–oxygen batteries. *Advanced Functional Materials, 33*(1), 2210702.

Nightingale Jr, E. (1959). Phenomenological theory of ion solvation. Effective radii of hydrated ions. *The Journal of Physical Chemistry, 63*(9), 1381-1387.

Organization, W. H. (2017). Tobacco and its environmental impact: an overview.

Ovodok, E. A., Ivanovskaya, M., Poznyak, S., Maltanova, A., Azarko, I., Micusik, M., . . . Aniskevich, A. (2023). Synthesis of Ti3AlC2 max phase under vacuum, its structural characterization and using for Ti3C2Tx MXene preparation. *Thin Solid Films, 771*, 139759.

Özgür, Ü., Alivov, Y. I., Liu, C., Teke, A., Reshchikov, M. A., Doğan, S., . . . Morkoç. (2005). A comprehensive review of ZnO materials and devices. *Journal of Applied Physics, 98*(4).

Pandiyarajan, T., Udayabhaskar, R., & Karthikeyan, B. (2012). Role of Fe doping on structural and vibrational properties of ZnO nanostructures. *Applied Physics A, 107*(2), 411-419.

Panneerselvam, C., Suresh, U., Alatawi, F. A., Angayarkanni, J., & Murugan, K. (2022). Cigarette butt waste derived activated carbon incorporated silver nanoparticle (AC-Ag): effective nanocomposite for anti-bacterial and anti-larval activity in wastewater remediation. *Materials Letters, 313*, 131809.

Raita, O., Popa, A., Stan, M., Suciu, R., Biris, A., & Giurgiu, L. (2012). Effect of Fe concentration in ZnO powders on ferromagnetic resonance spectra. *Applied Magnetic Resonance, 42*, 499-509.

Ranjkesh, Z., & Nasouri, K. (2023). Production of novel activated carbon fibers from smoked cigarette wastes using NaOH. *Macromolecular Research, 31*(7), 663-676.

Repp, S., & Erdem, E. (2016). Controlling the exciton energy of zinc oxide (ZnO) quantum dots by changing the confinement conditions. *Spectrochimica Acta Part A: Molecular and Biomolecular Spectroscopy, 152*, 637-644.

Ruf, T., Repp, S., Urban, J., Thomann, R., & Erdem, E. (2016). Competing effects between intrinsic and extrinsic defects in pure and Mn-doped ZnO nanocrystals. *Journal of Nanoparticle Research, 18*, 1-11.

Sahai, A., Kumar, Y., Agarwal, V., Olive-Méndez, S., & Goswami, N. (2014). Doping concentration driven morphological evolution of Fe doped ZnO nanostructures. *Journal of Applied Physics, 116*(16).

Saldarriaga, J. F., Aguado, R., Pablos, A., Amutio, M., Olazar, M., & Bilbao, J. (2015). Fast characterization of biomass fuels by thermogravimetric analysis (TGA). *Fuel, 140*, 744-751.

Salman Masoudi Soltani, S. M. S., & Sara Kazemi Yazdi, S. K. Y. (2012). The effect of pyrolysis time and heating rate on the surface area and pore size properties of porous carbon obtained from the pyrolysis of a cellulosic waste.

Sarycheva, A., & Gogotsi, Y. (2023). Raman spectroscopy analysis of the structure and surface chemistry of Ti3C2Tx MXene. In *MXenes* (pp. 333-355): Jenny Stanford Publishing.

Shahrokhi-Shahraki, R., Benally, C., El-Din, M. G., & Park, J. (2021). High efficiency removal of heavy metals using tire-derived activated carbon vs commercial activated carbon: Insights into the adsorption mechanisms. *Chemosphere, 264*, 128455.

Sharma, P. K., Dutta, R. K., Pandey, A. C., Layek, S., & Verma, H. (2009). Effect of iron doping concentration on magnetic properties of ZnO nanoparticles. *Journal of Magnetism and Magnetic Materials, 321*(17), 2587-2591.

Shekhirev, M., Shuck, C. E., Sarycheva, A., & Gogotsi, Y. (2021). Characterization of MXenes at every step, from their precursors to single flakes and assembled films. *Progress in Materials Science, 120*, 100757.

Shimodaira, N., & Masui, A. (2002). Raman spectroscopic investigations of activated carbon materials. *Journal of Applied Physics, 92*(2), 902-909.

Simon, P., & Gogotsi, Y. (2008). Materials for electrochemical capacitors. *Nature materials, 7*(11), 845-854.

Simon, P., Gogotsi, Y., & Dunn, B. (2014). Where do batteries end and supercapacitors begin? *Science, 343*(6176), 1210-1211.

Slaughter, E., Gersberg, R. M., Watanabe, K., Rudolph, J., Stransky, C., & Novotny, T. E. (2011). Toxicity of cigarette butts, and their chemical components, to marine and freshwater fish. *Tobacco control, 20*(Suppl 1), i25-i29.

Soares, A., Castro-Lopes, S., Cabrera-Baez, M., Milani, R., Padrón-Hernández, E., Farias, B., . . . Guerra, Y. (2022). The role of pH on the vibrational, optical and electronic properties of the Zn1-xFexO compound synthesized via sol gel method. *Solid State Sciences, 128*, 106880.

Sun, W., Wang, H. W., Vlcek, L., Peng, J., Brady, A. B., Osti, N. C., . . . Greenbaum, S. G. (2020). Multiscale and multimodal characterization of 2D titanium carbonitride MXene. *Advanced Materials Interfaces, 7*(11), 1902207.

Takai, K., Oga, M., Sato, H., Enoki, T., Ohki, Y., Taomoto, A., . . . Iijima, S. (2003). Structure and electronic properties of a nongraphitic disordered carbon system and its heat-treatment effects. *Physical Review B, 67*(21), 214202.

Tang, Q., Zhou, Z., & Shen, P. (2012). Are MXenes promising anode materials for Li ion batteries? Computational studies on electronic properties and Li storage capability of Ti3C2 and Ti3C2X2 (X= F, OH) monolayer. *Journal of the American chemical society, 134*(40), 16909-16916.

Toufani, M., Kasap, S., Tufani, A., Bakan, F., Weber, S., & Erdem, E. (2020). Synergy of nano-ZnO and 3D-graphene foam electrodes for asymmetric supercapacitor devices. *Nanoscale, 12*(24), 12790-12800.

Tribollet, J., Behrends, J., & Lips, K. (2008). Ultra long spin coherence time for Fe3+ in ZnO: A new spin qubit. *Europhysics Letters, 84*(2), 20009.

Vali, I. P., Anusha, B., Pruthvija, M., Savitha, S., Ravindra, S., Nagaveni, M., . . . Swathi, N. (2024). Bamboo and coconut shell based activated carbon: a Raman spectroscopic study. *Materials Chemistry and Physics, 318*, 129240.

Wang, J., & Kaskel, S. (2012). KOH activation of carbon-based materials for energy storage. *Journal of materials chemistry, 22*(45), 23710-23725.

Wang, Y., Alsmeyer, D. C., & McCreery, R. L. (1990). Raman spectroscopy of carbon materials: structural basis of observed spectra. *Chemistry of Materials, 2*(5), 557-563.

Ward, E. J., Lacey, J., Crua, C., Dymond, M. K., Maleski, K., Hantanasirisakul, K., . . . Sandeman, S. (2020). 2D titanium carbide (Ti3C2Tx) in accommodating intraocular lens design. *Advanced Functional Materials, 30*(47), 2000841.

Wu, Y.-F., Hsiao, Y.-C., Ou, Y.-J., Kubendhiran, S., Huang, C.-Y., Yougbaré, S., & Lin, L.-Y. (2022). Synthesis of cigarette filter-derived activated carbon using various activating agents for flexible capacitive supercapacitors. *Journal of Energy Storage, 54*, 105379.

Wu, Y., & Cao, C. (2018). The way to improve the energy density of supercapacitors: Progress and perspective. *Science China Materials, 61*(12), 1517-1526.

Xu, B., & Gogotsi, Y. (2020). MXenes: From Discovery to Applications. *Advanced Functional Materials, 30*(47).

Yang, H., Chen, P., Chen, W., Li, K., Xia, M., Xiao, H., . . . Chen, H. (2022). Insight into the formation mechanism of N, P co-doped mesoporous biochar from H3PO4 activation and NH3 modification of biomass. *Fuel Processing Technology, 230*, 107215.

Yang, J., & Qiu, K. (2011). Experimental design to optimize the preparation of activated carbons from herb residues by vacuum and traditional ZnCl2 chemical activation. *Industrial & engineering chemistry research, 50*(7), 4057-4064.

Yoon, Y., Le, T. A., Tiwari, A. P., Kim, I., Barsoum, M. W., & Lee, H. (2018). Low temperature solution synthesis of reduced two dimensional Ti 3 C 2 MXenes with paramagnetic behaviour. *Nanoscale, 10*(47), 22429-22438.

Yousef, S., Eimontas, J., Striūgas, N., Praspaliauskas, M., & Abdelnaby, M. A. (2024). Pyrolysis kinetic behaviour, TG-FTIR, and GC/MS analysis of cigarette butts and their components. *Biomass Conversion and Biorefinery, 14*(5), 6903-6923.

Zafeiridou, M., Hopkinson, N. S., & Voulvoulis, N. (2018). Cigarette smoking: an assessment of tobacco's global environmental footprint across its entire supply chain. *Environmental science & technology, 52*(15), 8087-8094.

Zhang, P., Phan, T. L., & Yu, S. C. (2012). Electron-spin-resonance study of polycrystalline Fe-doped ZnO ceramics. *Journal of the Korean Physical Society, 61*(10), 1563-1567.

Zhang, S., Liu, Q., Zhang, H., Ma, R., Li, K., Wu, Y., & Teppen, B. J. (2020). Structural order evaluation and structural evolution of coal derived natural graphite during graphitization. *Carbon, 157*, 714-723.

Zhang, Y., Yan, S.-s., Liu, Y.-h., Tian, Y., Liu, G., Chen, Y., . . . Liu, J. (2006). Ferromagnetic resonance study on Fe–ZnO inhomogeneous magnetic semiconductors. *Solid state communications, 140*(9-10), 405-409.